

# Atomistic Simulation of Defect Structure Evolution and Mechanical Properties at Long Time Scales

by

Yue Fan

B.S., Physics, Peking University, Beijing, China (2008)

Submitted to the Department of Nuclear Science and Engineering  
in partial fulfillment of the requirement for the degree of

Doctor of Philosophy in Nuclear Science and Engineering

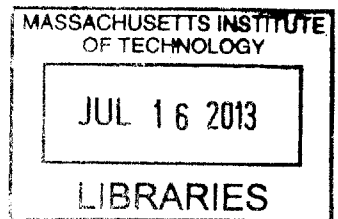
at the

MASSACHUSETTS INSTITUTE OF TECHNOLOGY

June 2013

© Massachusetts Institute of Technology 2013. All rights reserved.

ARCHIVES



Author .....  
Department of Nuclear Science and Engineering  
May 10, 2013

Certified by .....  
*[Signature]*  
Bilge Yildiz  
Associate Professor of Nuclear Science and Engineering  
Thesis Supervisor

Certified by .....  
*[Signature]*  
Sidney Yip  
Professor of Nuclear Science and Engineering and Materials Science  
Thesis Co-advisor

Certified by .....  
*[Signature]*  
Michael J. Demkowicz  
Assistant Professor of Materials Science and Engineering  
Thesis Reader

Accepted by .....  
*[Signature]*  
Mujid S. Kazimi  
TEPCO Professor of Nuclear Engineering  
Chair, Department Committee on Graduate Theses



**[THIS PAGE INTENTIONALLY LEFT BLANK]**

# **Atomistic Simulation of Defect Structure Evolution and Mechanical Properties at Long Time Scales**

by

Yue Fan

Submitted to the Department of Nuclear Science and Engineering  
on May 2, 2013, in partial fulfillment of the  
requirements for the degree of  
Doctor of Philosophy

## **Abstract**

This thesis is a computational and theoretical investigation of the response of materials' mechanical properties to a wide range of environmental conditions, with a particular focus on the coupled effects of strain rate and temperature. The thesis provides original contributions to the fundamental understanding of how the materials mechanical properties change, as manifested by defect structure evolution, with temperature and strain rate conditions, as well as to the development of methodology used for enabling the investigation of dislocation-defect interactions over a much wider range of time scales than of reach to traditional techniques.

This thesis advanced the capabilities of a recently developed activation-relaxation based atomistic method to enhance the accuracy of kinetic predictions, and to enable the investigation of dislocation-defect interactions dynamically at long time scales. We took the Autonomous Basin Climbing (ABC) method as a starting point, and incorporated the ability to sample multiple transition pathways associated with a given state. This new feature addresses the problem of overestimating the system evolution time due to the one-dimensional nature of the original ABC algorithm. The ABC method was further implemented in a dynamic framework, which makes it possible for the first time to directly simulate the dislocation-obstacle interactions at very low strain rates. This approach allows for a new way to connect the atomistic results to models at the meso-scale for simulating the plasticity of metals.

We analytically derived how the applied strain rate couples with the thermal activation process, based on the framework of transition state theory informed by the atomistic approach described above. We demonstrated the coupling effect is a common mechanism behind many important phenomena, and provide three

examples from the atomic level on the dislocation mobility and dislocation interactions with radiation induced defects. (i) A well-known universal flow stress upturn behavior in metals has been examined. We provide a simple physically based model to predict the flow stress at various strain rates, without invoking any assumed mechanisms or fitting parameters as in the traditional constitutive models. (ii) We implemented this new model in (i) to investigate the dislocation-obstacle interactions. The approach enabled us to map the interaction between an edge dislocation and a self interstitial atom (SIA) cluster in Zr in a two-parameter space consisting of temperature and strain rate. This approach allows the direct atomistic simulation of dislocation-obstacle interactions at experimental time scale, namely at low strain rates, which cannot be reached by traditional atomistic techniques. The dislocation is found to absorb the SIA cluster and climb at low strain rates and high temperatures, while it passes through the SIA cluster at high strain rates and low temperatures. The predicted mechanism map is able to reconcile the seeming controversy between previous experimental and computational findings. (iii) A dislocation-void interaction in bcc Fe at prescribed strain rate is also investigated. We demonstrated that different applied strain rates can affect the interaction mechanism and the defect microstructure, and eventually lead to a negative strain rate sensitivity (nSRS) of yield strength below a critical strain rate. This finding at the unit process level supplements the previous explanations of the nSRS with higher level constitutive relations.

Beyond the specific cases analyzed in metals in this thesis, the insights gained on the coupling between strain rate and thermal activation can be used to explain the dependence on strain rate and temperature in other important classes of materials (e.g. colloids, cement) and phenomena (e.g. corrosion, creep).

Thesis Supervisor: Bilge Yildiz

Title: Associate Professor of Nuclear Science and Engineering

## **Acknowledgments**

Thanks go first and foremost to my thesis advisor, Prof. Bilge Yildiz. Throughout the five-year period at MIT, I have been fortunate to work with her and have her guidance and support. Her kindness, patience and understanding make it possible to overcome all the hardships while finishing this thesis, as well as conducting my researches. Professor Yildiz puts her effort in helping me on every small step that I need to make, from working with me through my first publication, to giving me detailed advices on how to deliver an insightful presentation. Any of my accomplishments would have been impossible without her support, and I hope her exacting standards and professionalism will stay with me during my career.

I would like to thank my thesis co-advisor, Prof. Sidney Yip, for his valuable suggestions and comments during my thesis research. Through my conversations and interactions with Prof. Yip not only have I broadened my scientific view from the very fundamental level, but I have also learned great wisdom necessary to succeed in any professional or personal endeavor.

I would also like to acknowledge my thesis reader, Prof. Michael J. Demkowicz, for the many discussions he held with me at all stages of the work presented here. I have been inspired by our joyful conversations and learned a lot from his insightful comments. I also want to thank Prof. Ju Li, for serving on my thesis committee. I have been motivated by his pioneering work in dislocation nucleation and further developed the theory for describing dislocation flow.

I owe special thanks to Dr. Yuri N. Osetsky (ORNL), for his productive collaboration. I hope such collaboration will continue in my future career. I also need to acknowledge Oak Ridge National Lab for offering me the prestigious Wigner Fellowship, which provides a great opportunity for pursuing my research together with the top scientists in the world. I am happy to thank Dr. Marius Stan (ANL), for his support during my postdoc application. Although I decided to join Oak Ridge National Lab in the end, I still need to acknowledge Argonne National Lab, for offering me the prestigious Aneesur Rahman Fellowship.

I am also grateful for the support of all the members of the Yildiz group, from past to now, during my PhD period. They all have contributed to my scientific success and were always happy to provide helpful comments. I own special thanks to Dr. Akihiro Kushima, the developer of Autonomous Basin Climbing (ABC) method, without which most of my research would not have been possible to be done. I would also like to thank Mostafa Youssef, Dr. Dario Marrocchelli, for their discussion and suggestions on many problems encountered in my research. I also acknowledge our new group member, Lixin Sun, for her help in implementing ABC algorithm to a well-known simulation software LAMMPS, which broadened the potential applicability of ABC method to many other systems.

I'm happy to thank Yan Chen, Wen Ma, Dr. Zhuhua Cai, Fei Yan, Wei-Shan Chiang, Liang Zhang, Prof. Yang Zhang (UTUC), Dr. Wei-Ren Chen (ORNL), Dr. Xianming Bai (INL) for their friendship and support.

I greatly acknowledge all the financial supports during my PhD, including the fellowship from Department of Nuclear Science and Engineering at MIT, Nuclear Regulatory Commission Young Faculty Grant, and the Consortium for Advanced Simulation of Light Water Reactors (Contract No. DE-AC05-00OR22725).

I want to thank my undergraduate university, Peking University, the School of Physics, where I built up a solid background in physics, which will benefit my entire career. I would also like to thank China, the motherland where I was born and grew, for her drastic development that makes me proud of. Specifically, my research was coincidentally highlighted on the MIT homepage on last October 1<sup>st</sup>, also the national day of China, and that was one of the most joyful moments in my life.

Although it should go without saying, I still want to stress that none of my achievement is possible where there is no group of family to offer support and understanding. I want to dedicate this thesis to my dear wife, Lu Xing, for her love, patience, and the happiness that we shared every day. I cannot write enough words to thank my father, mother and sister, for their everlasting understanding and encouragements that helped build my character to be a simple, humble, and honest person.

# Contents

<b>Abstract</b> .....	iii
<b>Acknowledgments</b> .....	v
<b>List of Tables</b> .....	ix
<b>List of Figures</b> .....	x
<b>1 Introduction</b> .....	1
1.1 Background and Motivation .....	1
1.2 the Aim and the Contributions of the Thesis .....	5
1.3 Scope of Thesis .....	7
<b>2 Methodology: Atomistic Simulations at Long Time Scale</b> .....	11
2.1 Potential Energy Landscape .....	11
2.2 Overview of Existing Atomistic Methods for Exploring PES .....	12
2.2.1 Activation Relaxation Technique (ART) .....	12
2.2.2 Dimer Method .....	13
2.2.3 Hyperdynamics and Temperature-Accelerated Dynamics (TAD) Methods .....	14
2.2.4 Autonomous Basin Climbing (ABC) Method .....	15
2.2.5 Discussion on Different Techniques .....	18
2.3 Extension of ABC (ABC-E) Method .....	19
2.3.1 Analytical TST and KMC .....	20
2.3.2 1D Nature of ABC Method .....	22
2.3.3 Extension of ABC (ABC-E) Method .....	24
2.4 ABC Method in a Dynamic Scenario .....	26
<b>3 Point Defects: Structure Evolution, Accumulation, and Migration</b> .....	29
3.1 SIA Cluster Unfaulting in BCC Fe .....	29
3.1.1 Background and Motivation .....	29
3.1.2 Problem Statement and System Set Up .....	31
3.1.3 Results .....	32
3.1.4 Discussion .....	36
3.2 Vacancy Accumulation in BCC Fe .....	38
3.2.1 Background and Motivation .....	38
3.2.2 Problem Statement and System Set Up .....	39
3.2.3 Results .....	40
3.2.4 Discussion .....	47
3.3 Anisotropic Diffusion of Vacancies and Self Interstitial Atoms in HCP Zr .....	48
3.3.1 Vacancy Diffusion .....	48



3.3.1.1	Background and Motivation.....	48
3.3.1.2	Problem Statement and System Set Up.....	49
3.3.1.3	Results and Discussion.....	49
3.3.2	Self-interstitial Atom (SIA) Diffusion.....	52
3.3.2.1	Problem Statement and System Set Up.....	52
3.3.2.2	Results and Discussion.....	55
<b>4</b>	<b>Line Defects: Dislocation Mobility, and Interaction with Point Defects</b> .....	<b>64</b>
4.1	Dislocation Mobility at Prescribed Strain Rate and Temperatures.....	64
4.1.1	Background and Motivation.....	64
4.1.2	Problem Statement.....	65
4.1.3	Results and Discussion.....	65
4.2	Dislocation-SIA Cluster Interaction Mechanisms Mapped by Atomistic Simulations as a function of Strain Rate in Zr.....	77
4.2.1	Background and Motivation.....	77
4.2.2	Problem Statement and System Set Up.....	80
4.2.3	Results and Discussion.....	81
4.3	Inverse Relation between Critical Resolved Shear Stress and Strain Rate — Dislocation-Vacancy Cluster Interaction in BCC Fe.....	91
4.3.1	Background and Motivation.....	91
4.3.2	Problem Statement and System Set Up.....	92
4.3.3	Results and Discussion.....	92
<b>5</b>	<b>The Interface Connecting Atomistic Simulation to Engineering Scale Model</b> .....	<b>101</b>
5.1	Atomistic Interface to Engineering Scale Model.....	102
5.1.1	Background and Visco-Plastic Self-Consistent (VPSC) Model.....	102
5.1.2	Atomistic Interface to VPSC Model.....	103
5.1.3	Connecting Atomistic Model to VPSC — Example on Dislocation-Void Interaction.....	105
5.1.4	Provide Physical Based Description to Mesoscale Constitutional Model: Example on Strain Rate Sensitivity.....	109
<b>6</b>	<b>Summary and Broad Implication</b> .....	<b>114</b>
6.1	Summary of the Thesis.....	114
6.2	Analogy between Glass Rheology and Crystal Plasticity.....	118
6.2.1	Background.....	118
6.2.2	Yield Strength of Amorphous System.....	119
6.2.3	Analogy between Amorphous and Crystal System.....	122
6.2.4	Discussion and Broader Implications.....	125
	<b>Bibliography</b> .....	<b>127</b>

# List of Tables

Table 3.1: The mean and the standard deviation of the life-time in the unfauling of the NPC 4-SIA cluster found from the MD simulations using the AMS potential ..... 36

Table 3.2: The energetic of SIA states and the comparison against previous calculations ..... 54

Table 3.3: The summary on SIA migration mechanism in Zr from ABC-E results ... 59

# List of Figures

Figure 2.1:(a) Schematic illustration of the ABC method (Figure adapted from Ref.[40]). The system climbs out of a potential energy basin (1-3) by adding Gaussian penalty functions to the system’s potential energy. Finally, the system reaches the neighboring minimum (4). (b) Trajectory of energy values (1-4) involved in the ABC method, corresponding to the case in (a). (c) Potential energy landscape derived from (b), and the KMC simulation parameters based on it. ....	16
Figure 2.2: Illustration of a connected nodes network, with the initial state “ <i>i</i> ” and final state “ <i>f</i> ”.....	20
Figure 2.3: An evolution chain is provided by ABC algorithm. The red path on the left corresponds to the PES of a one dimensional chain of transitions illustrated on the right.....	22
Figure 2.4: (a) A pre-constructed 2D PES with rough landscape, for representing the multiple processes scenario. (b) Variation of the evolution time with temperature sampled by full catalogue KMC, ABC (average of 6 runs), and ABC-E .....	26
Figure 2.5: Illustration for the dynamic model in capturing the dislocation-obstacle interaction as a function of strain rate, $\dot{\epsilon}$ , and temperature, T .....	27
Figure 2.6: Strategy of accepting a transition event or not in the dynamic model of ABC method.....	28
Figure 3.1: (a) The evolution of energy and atomic trajectories (C1-C6) starting with the initial NPC 4-SIA cluster, found by using the ABC method with the AMS potential (visualized by Atomeye Ref.[97]). Blue balls represent the interstitial atoms, green balls represent the vacant lattice sites, small orange balls represent the atoms on lattices. The grey rods are placed only to accentuate the defect structure, but do not represent a physical meaning for a special set of bonds. (b) The potential energy landscape associated with the atomic configurations described in (a) .....	33

Figure 3.2: Arrhenius relation between the mean life-time,  $\bar{t}$ , of NPC 4-SIA cluster and temperature, T (the life time at 1050K was set as  $t_0$ ), with an effective energy barrier of  $E_b$  derived from KMC simulations, and MD results, respectively ..... 35

Figure 3.3: A schematic plot of different stages during the resistivity recovery experiments in Fe. Among these stages, stage IV is longstanding controversial. Under electron irradiation conditions, the vacancy cluster motion stage is missing, while it exists under neutron irradiation conditions. (The plot is adapted from Ref .[91]) ..... 38

Figure 3.4: (a) Sequence of atomic configurations of vacancies in bcc Fe generated by ABC sampling (lattice atoms not shown) with initial configuration C1 consisting of 50 single vacancies. (b) Sequence of vacancy configurations depicting the reaction between two vacancy clusters,  $V1+V2 \rightarrow V3$ . Blue balls represent the inserted vacancies, and red balls and green balls represent the interstitial atoms and vacant lattice sites, respectively, that arise during the vacancy cluster structure evolution ..... 40

Figure 3.5: The migration barrier for a single vacancy near a small cluster. The barrier 0.44 eV is considerably smaller than 0.63 eV, the vacancy migration barrier in bulk Ref.[107] ..... 41

Figure 3.6: (a) The PES associated with a subset of the structural evolution shown in Figure 1(a), with initial and final average clusters of 6 and 9 vacancies, respectively. Inset: A region on the PES where the system is trapped in the early stages of evolution. (b) The average vacancy cluster size associated with the PES in (a). (c) Fraction of mono-vacancies among all the defects during structural evolution. (d) Evolution of vacancy clusters corresponding to the size increase seen in Regime III in (b) ..... 43

Figure 3.7: Temperature dependence of the average cluster size (red points) simulated by KMC based on the PES in Fig. 2(a), and the PAS data (blue points) Ref.[100] showing the relative intensity of vacancy clusters with size larger than ten. 46

Figure 3.8: Two vacancy migration paths in Zr, represented by M1 and M2. These paths are captured by the ABC-E algorithm.....	49
Figure 3.9: (a) The total MSD and its projection on $\langle a \rangle$ and $\langle c \rangle$ directions, at 1000 K. The slopes represent the diffusivities along different directions. (b) The ratio between the $\langle c \rangle$ and $\langle a \rangle$ diffusivities at various temperatures. All the results in (a) and (b) are based on the assumption that the pre-factors of two migrations are the same.....	50
Figure 3.10: Blue triangles: the results with MA07 potential, and the same pre-factors. Red squares: the results with MA07 potential, and different pre-factors. Purple open squares: the results with AWB95 potential, and different pre-factors ....	51
Figure 3.11: Diffusivity under different temperatures, by AB MD method, and with the MA07 potential.....	52
Figure 3.12: Possible interstitial sites in hcp metals (shown by green spheres).....	53
Figure 3.13: Only three stable among all six possible interstitial sites are stable, within MA07 interatomic potential. ....	54
Figure 3.14: Direct O-O hopping mechanism. O state can migrate to either 1st NN O state or 2nd NN O state, as shown in (a) and (b), respectively. ....	55
Figure 3.15: O-M1-BC migration pathway and associated barriers. Notice that O-M1 transition has actually two degeneracies, while the figure above only shows one of them. ....	56
Figure 3.16: O-M2-O migration pathway and associated barriers. O-M2 transition has actually two degeneracies, while the figure above only shows one of them. ....	57
Figure 3.17: BC-BO-BC migration pathway and associated barriers. BO-BC transition has three degeneracies, while the figure above only shows one of them....	58

Figure 3.18: The summary on SIA migration mechanisms in Zr from Gopinath et al's TAD results Ref.[114].....	58
Figure 3.19: (a) SIA diffusion trajectories up to 100 ps, at 300 K and 500 K, respectively. (b) The projections of trajectories in basal plane.....	60
Figure 3.20: (a-c) The MSD on <a> and <c> directions, at 150 K, 600 K, and 900 K, respectively. (d) The ratio between the <c> and <a> diffusivities at various temperatures .....	62
Figure 4.1: (a) Strain-stress curve of the $\frac{1}{2}\langle 111 \rangle$ screw dislocation in bcc Fe under static conditions. The corresponding Peierls stress is about 1400 MPa. (b) Activation barrier for the glide motion of $\frac{1}{2}\langle 111 \rangle$ screw dislocation as a function of stress. Blue squares represent the calculated data points by ABC method. The red line is a fit to $E(\sigma) = E_0 \left[ 1 - (\sigma / \sigma_c)^p \right]^q$ with $p=0.63$ and $q=1.41$ . The dashed line represents a constant activation volume scenario with $p=1$ and $q=1$ . .....	69
Figure 4.2: (a) The flow stress of the $\frac{1}{2}\langle 111 \rangle$ screw dislocation under different strain rate and temperature conditions. The solid lines show the results calculated according to Eq.(4.8) with the attempt frequency of $1.2 \cdot 10^{12} \text{ s}^{-1}$ . The open squares and triangles represent direct MD simulation results at strain rates of $10^7 \text{ s}^{-1}$ and $10^6 \text{ s}^{-1}$ , respectively. (b) The relation between strain rate (in logarithmic scale) and $1/T$ at constant flow stress of 800 MPa and 500 MPa. The dashed lines are linear extrapolation from the low strain rate regime. ....	71
Figure 4.3: (a) The predicted relation between flow stress and strain rate at 50 K and 100 K. The solid symbols and lines are the calculated results for the $\frac{1}{2}\langle 111 \rangle$ screw dislocation in bcc Fe with $p=0.63$ and $q=1.41$ in $E(\sigma) = E_0 \left[ 1 - (\sigma / \sigma_c)^p \right]^q$ . The dashed lines are the results for a hypothetical scenario of $p=1$ and $q=1$ that corresponds to constant activation volume for the dislocation. (b) Variation of reduced flow stress with strain rate at 300 K. The experimental data on copper (blue triangles) and on iron (red squares) are adapted from Ref.[38] and references therein.	

The black line represents the results calculated by Eq.(4.8), with the activation energy profile input from Gordon et al.'s work in Ref.[127] for a long screw dislocation in bcc Fe. .... 74

Figure 4.4: (a) The strain-stress curve for the interaction between the  $1/3 \langle 11\bar{2}0 \rangle \{1\bar{1}00\}$  prismatic edge dislocation and a basal 5-SIA cluster in hcp Zr .The numbers 1-5 represent the critical points during the interactions. (b) The corresponding critical configurations during the interaction..... 82

Figure 4.5: (a) (left) The stress-strain curves under different strain rate conditions, and (right) associated critical configurations (1-4 shown in (a)). (b) The unit process governing the kinks in the strain-stress curve in (a) for the lower strain rate cases.... 84

Figure 4.6: (a) The energy barrier for the trigger reaction that leads to dislocation jog via the absorption of the SIA cluster, shown here as a function of strain, associated with the strain-stress curves in Figure 4.5 (a). (b) The strain rate-temperature diagram that provides the boundary for the transitions between the two mechanisms that govern the dislocation-SIA cluster interaction. The red line is the calculated boundary with the attempt frequency of  $10^{13} \text{s}^{-1}$ . The upper boundary of the light blue stripe represents the results with the attempt frequency of  $10^{14} \text{s}^{-1}$ , while the lower boundary represents the results with the attempt frequency of  $10^{12} \text{s}^{-1}$ . The blue data points are the MD results. In particular, the open squares represent the result of mechanism I, that dislocation simply passes through the SIA cluster; while the filled squares represent the mechanism II, that the SIA cluster is absorbed by the dislocation..... 87

Figure 4.7: (a) The strain-stress curve, and associated potential energy of the system, during the static interaction. (b) The corresponding critical atomistic configurations during the static interaction as shown in (a). The structures are visualized by Atomeye Ref.[97], and colored according to different coordination numbers..... 93

Figure 4.8: (a-b) The stress-strain curves for the dislocation void interaction under different strain rate conditions, provided by ABC and MD simulations, respectively. (c) The associated critical atomic configurations after the interaction..... 95

Figure 4.9: The CRSS under different strain rates conditions. Red open squares are the results of ABC framework simulations, while the black squares represent the MD simulations results. .... 96

Figure 4.10: (a) The energy differences under different strain rate conditions, with respect to the static energy landscape. (b) The atomistic configurations during the interactions, at various strain rates. (c) The atom density distributions along x-axis, i.e. the  $\langle 111 \rangle$  direction, for structures S1-S5. The vacancy cluster's fractional coordinate along x-axis is about 0.8. It clearly shows that for high strain rates  $10^6\text{s}^{-1}$  and  $10^8\text{s}^{-1}$ , the vacancy clusters are ripped into parts, while such behavior is not observed for lower strain rate conditions. .... 97

Figure 5.1: The interaction mechanism between  $\langle a \rangle$  type edge dislocation and vacancy cluster under (a) 0 MPa, and (b) yield stress  $\sim 300$  MPa, respectively..... 105

Figure 5.2: (a) The energy landscape of the dislocation-void interaction at different stress conditions. (b) The corresponding effective barriers and interaction mechanisms at different stress conditions. .... 107

Figure 5.3: The reduced climb rate, following the definition in Eq.(5.7), as a function of temperature at different stress conditions. .... 109

Figure 5.4: The measured strain rate sensitivity for Zircaloy-4, defined as  $m = \partial \ln \sigma / \partial \ln \dot{\epsilon}$ , at different temperatures. The plot is adapted from Ref.[155]. .... 110

Figure 5.5: (a) The relation between yield strength and applied strain rate in a log-log scale, at different temperature, in a Fe model system. (b) The strain rate sensitivity calculated from (a), as a function of temperature. .... 112





# Chapter 1

## Introduction

### 1.1 Background and Motivation

The design of materials with unique functionalities has become increasingly important to meet the urgent demand for sustainable energy technologies. Advanced nuclear reactors are being designed for longer life times while operating in extreme conditions of temperature, chemical activity, and irradiation [1-5]. Developing materials more tolerant to extreme conditions thus requires understanding and assessing the irradiation induced microstructural evolution. This thesis focuses on the dislocation-obstacle interactions under a wide range of temperature and strain rate conditions [6-10]. Understanding the dislocation-obstacle interaction mechanisms is important because these interactions affect the mechanical properties of structural materials ranging from creep and growth to plasticity and hardening [11-16]. However, traditional atomistic simulations to date have only addressed the behavior of these defect systems at high-strain rates because of the limitations related to the time scales of reach to them. This situation left open the question of whether the accurate mechanisms are indeed captured, which this thesis aims to address.

Computational modeling and simulation, accompanied by the continuous enhancement of computing power during past few decades, has become an effective quantitative approach for progress in many disciplines, ranging from predicting the protein's molecular structure to global climate change, from drug design to galaxy formation and evolution. In a nutshell, computational methods drastically extend the reach of research methods because virtual experiments and predictions can easily be

performed under simulated conditions beyond the practicality of real experiments [17]. Due to such extensive capability, a wide range of computational methods constructively complement the theoretical and experimental methods [18].

While simulations have particular advantages over “real” experiments in terms of lower cost, faster progress, better control of isolated parameters in affecting the modeled system, there are still formidable challenges. This thesis focuses on atomistic simulations and their connection to meso-scale and continuum approaches. The major limitations of atomistic simulations involve the small length and short time scales of the system that can be reached. The length scale issue is less challenging because even hundreds of atoms, with the assistance of periodic boundary condition, can well represent many materials’ bulk properties. In addition, the length scale limitation can, at least partially, be addressed by parallelizing the problem and computing in large supercomputer systems. However, the time step in the integration over time cannot be parallelized in the computations. This makes it a formidable challenge to reach long time scales with atomistic simulations. Particularly in nuclear structural materials, defects are produced within displacement cascades induced by high-energy neutrons, ions and electrons, at very short time scales ( $\sim 10^{-13}$ - $10^{-11}$  s). The defect migration, interaction, and accumulation govern the microstructural evolution, which in turn determines the macroscopic degradation of the materials at the time scale of years ( $\sim 10^7$  s $^{-1}$ ) [11]. The process from defect formation till the observation of the radiation effects on macroscopic properties spans more than 20 orders of magnitude in time. On the other hand in atomistic simulations, the most accurate techniques, ab initio based methods, can only reach the pico-seconds time scale due to the extremely expensive computational load. While molecular dynamics (MD) simulation, another widely used atomistic technique, is able to reach much longer time scale than ab initio method, it can hardly go beyond nano-second, which is still more than ten orders of magnitude away from the “real” experiments.

Due to such a large gap between the time scales that MD can reach and the experiments, results obtained by MD might not reflect the accurate mechanisms

taking place at long times. Particularly in this thesis, we focus on the interactions between dislocations and obstacles, which are known to significantly affect the mechanical properties of structural materials over a wide range of conditions including low strain rates over long time scales. Most MD studies to date aimed to reveal the interaction mechanisms between dislocations and obstacles by performing the simulations only at one particular or very limited range of conditions. Typical MD calculations of these interactions are performed either at very high strain rates greater than  $10^6\text{s}^{-1}$  [7, 9, 10, 19-22], or at static conditions where the temperature is set to be 0 K [23-26]. The static calculations do not involve integration over time, and only relax the system based on the minimization of the potential energy. Thus, they intrinsically prohibit the thermal activation process while straining the system. Therefore the molecular static simulations give rise to effectively equivalent outcomes as the MD simulations at the very high strain rate limit which also does not permit thermal activation [27-29]. This equivalence is first analytically demonstrated by Zhu et al. [28], then by Weinberger et al. [27], and finally by the author of this thesis [29]. For the sake of simplicity, we will therefore refer to both scenarios as high strain rate studies below. These high strain rate results are either directly compared with experiments [21] or incorporated into continuum approaches [22]. An emergent problem is therefore raised - can the high strain rate studies well represent the real experiments driven at much lower strain rates?

An example that supports this question is a seeming controversy between the simulated prediction and the experimental observation over the interaction mechanism between an edge dislocation and a defect cluster in Zr. In molecular static calculations [25], the simulation was performed at 0 K, and the system was driven by the applied shear strain only without any thermal activation. These conditions are akin to the high strain rate and low temperature limit [27-29] because they don't give rise to thermal activation over sufficiently long time, as discussed above. In those atomistic simulations, the dislocation and obstacle was found not to interact with each other. In other words, the dislocation simply passes through the obstacle upon induced shear deformation, leaving both the defects structure

recovered in the end [25]. While in tensile experiments, under very low strain rate ( $10^{-4}\text{s}^{-1}$ ) and high temperature (600 K), dislocation channel formation is clearly observed [30], indicating the absorption of obstacle on the slip plane by the dislocation. The experimental results starkly differ from the simulation results described above.

Such discrepancy between experiments and atomistic simulations raises a key challenge - by straining the system too fast in traditional atomistic simulations (since the static simulations indeed represent the high strain rate limit [27-29]), are we missing thermally activated processes which end up not having enough time to occur? Furthermore, previous high strain rate simulations suggest that the temperature can also affect the interaction mechanisms between dislocations and obstacles [9, 20]. For example, in a unit process of interaction between dislocation and SIA loop in bcc Fe, under the same level of applied strain rates around  $10^6\text{s}^{-1}$ , the SIA loop is absorbed by the dislocation at high temperature; while both the dislocation and SIA loop recover fully at low temperature. These findings demonstrate that both the temperature and the applied strain rate together determine the interaction mechanism because of the presence of thermally activated processes. However, the following questions have been open: are the strain rate effect and temperature effect independent from each other or do they act in concert with each other? If they do couple, what is the relation between these two driving factors? And consequently, how can this interrelation determine the interaction mechanisms between dislocations and obstacles under a wide range of conditions?

## 1.2. the Aim and the Contributions of the Thesis

The aim of this thesis is to address systematically the challenges summarized above – namely:

- 1) gain a quantitative and physically based understanding of the coupled temperature and strain rate effects on the interaction mechanisms between dislocations and obstacles using atomistic simulations, and
- 2) develop and adapt new atomistic methods that enable the investigation of dislocation-defect interactions over a much wider range of time scales than traditional techniques.

The key contributions of this thesis are two-fold. The first is a new and fundamental understanding of how the materials mechanical properties change, as manifested by defect structure evolution under a wide range of conditions, with a particular focus on the temperature and strain rate effects [29, 31]. Specifically, we analytically elucidated how the applied strain rate affects the thermal activation process, based on a theoretical derivation that we developed. By using this analytical derivation that represents the coupling between the strain rate and thermal activation, we successfully explained a longstanding challenge of flow stress upturn behavior [32-38], without invoking any assumed mechanisms or fitting parameters. We then combined the theoretical derivation with the newly developed atomistic technique, and investigated the strain-rate and temperature dependence of dislocation-obstacle interactions in plasticity of metals, specifically Zr and bcc Fe in this thesis. This approach enabled us to uncover the interaction mechanisms over a very wide range of strain rates ( $10^{-7}\text{s}^{-1}$  to  $10^8\text{s}^{-1}$ ), which is far beyond the reach of the MD method. We demonstrated that the interaction is impacted by both thermal activation and strain rate effects, and provided an interaction mechanism map within a two-parameter space consisting of temperature and strain rate for the case in Zr. The interaction mechanism is actually an outcome of the competition between thermal activation and strain rate. In particular, at high temperatures and low strain rates, the

thermal activation has enough time to take place and leads to the obstacle absorption by dislocation; while at low temperatures and high strain rates, the process does not have enough time to be thermally activated and the dislocation simply passes through the obstacle, leaving both defects recovered in the end. This finding very well reconciles the seeming controversy between experiments [30] and previous simulations [25] mentioned above. In other words, they are not really contrary to each other, the different results arise rather because of the different conditions in the simulations and in the experiments reported above. The same framework has also been extended to a similar problem involving a dislocation-void interaction in bcc Fe, and supplements the previous understanding of the origin of negative strain rate sensitivity behavior [39]. In sum, this fundamental understanding can be used to aid in explaining and predicting a broader range of problems where time scales are important in determining the materials behavior.

This scientific contribution was enabled by the new method that I introduced and further developed for addressing this problem – that makes the second contribution of this thesis. Evolution of defect microstructure at long time scales could not be directly simulated by traditional atomistic methods, and an alternate approach is necessary. For this purpose, we introduced a novel computational technique recently developed by Kushima et al. [40, 41]. The technique is based on an activation-relaxation algorithm, called Autonomous Basin Climbing (ABC), and enables the simulation of the problem at arbitrarily long time scales while retaining the atomic details and predictive power. This thesis further developed the ABC technique for better accuracy and for implementation in dynamic scenarios. We incorporated the capability to sample multiple transition pathways associated with a given state, and this added feature improves the accuracy of the kinetic predictions. We implemented this technique in a dynamic framework, which made it possible to directly simulate the dislocation-obstacle interactions at very low strain rates. This is regarded as the tool preparation step for bridging the different time scales between experiments and traditional computations.

## 1.3 Scope of Thesis

This thesis is organized as described below:

In Chap 2 we discuss the basic principles of long time scale computational techniques, and the atomistic simulation methodologies that will be employed throughout the thesis. The notion of potential energy surface (PES) and its importance in materials evolution are introduced in Section 2.1. Section 2.2 gives a brief overview of several existing long time scale atomistic methods based on the concept of escaping from deep energy minima on PES, with a particular focus on the Autonomous Basin Climbing (ABC) algorithm [40] that is employed throughout the thesis. In the end of Section 2.2, we have a discussion on these methods in terms of advantages and drawbacks, and specify the reason for picking ABC method in this thesis. The advancement of the ABC technique (ABC-E with the capability of detecting multiple transition pathways is described in Section 2.3. Such modification makes it possible for considering multiple competitive mechanisms, e.g. the anisotropic diffusion of defects in hcp Zr (Sec 3.3-3.4), and improves the accuracy of the predictions of kinetics. This chapter closes in Section 2.4 with an introduction of how dynamic simulations at a given strain rate can be performed by using ABC and transition state theory. The purpose of dynamic simulations in this thesis is investigating the dislocation-point defect interactions that will be discussed in Chap 4. The dynamic implementation using ABC makes it possible for the first time to perform atomistic and predictive simulations of the dislocation-obstacle interactions at very low strain rate conditions, which can be directly compared with experiments.

Chap 3 presents the simulation results on the formation, migration and accumulation of point defects in nuclear structural materials. This is important because the point defects are formed under irradiation and are usually the obstacle to dislocations, and their interactions with dislocations determine the mechanical properties of the structural materials. Section 3.1 introduces the structure of the newly observed sessile self-interstitial atom (SIA) cluster in bcc Fe under irradiation, and its unfauling mechanism to the traditional mobile structure. The unfauling time



of such sessile SIA cluster is calculated under different temperatures, and found consistent with the direct MD simulations. Another type of defect, the vacancies, is studied in Section 3.2. Particularly, we introduce a supersaturated vacancy environment and discuss how the vacancies interact and accumulate with each other. The growth curve of the average size of vacancy cluster is calculated as a function of temperature, and compared with the positron annihilation spectroscopy (PAS) experiments. Section 3.3 and 3.4 discuss the anisotropic diffusion of vacancy and SIA in Zr, with the implementation of ABC-E method. And correspondingly, the results are benchmarked against different other available techniques, including MD, adaptive-boost (AB) MD [42], and temperature-accelerated dynamics (TAD) [43].

Chap 4 focuses on the dislocation mobility and its interaction with irradiation induced point defects, cause they affect the mechanical properties that are critical for the safety of structural materials in the nuclear reactor [24, 25, 44–47]. The examples in this chapter reflect a common mechanism behind all these simulated processes, specifically, the competition between strain rate and thermal activation, which is a key contribution of this thesis. In Section 4.1 we consider the dominant plastic unit in bcc Fe, the glide motion of  $\frac{1}{2}\langle 111 \rangle$  screw dislocation. An analytical theory is developed for describing the dislocation mobility under different applied strain rate and temperature conditions. It is demonstrated that there is a significant coupling effect between the two variables of applied strain rate and temperature. This derived theory, combined with atomistically calculated input, describe naturally a flow stress upturn behavior at high strain rate regime, an experimentally established phenomena for which the underlying mechanism has not been clarified before. A unit process of dislocation-SIA cluster interaction in Zr is studied in Section 4.2. The interaction mechanisms are predicted and the corresponding mechanism map is cast in a two-parameter space consisting of temperature and strain rate. This study spans a wide range of strain rate conditions, from  $10^{-7}\text{s}^{-1}$  to  $10^8\text{s}^{-1}$ , which makes it possible to directly compare with experiments. The SIA cluster is found to be entirely absorbed by the dislocation at low strain rates and high temperatures; while at high strain rates and low temperatures the dislocation passes through the SIA cluster, leaving behind

both the SIA cluster and the dislocation structures fully recovered. The constructed mechanism map displays the material's response under various conditions, and also explains the seeming inconsistencies between the previous experimental and computational results. Section 4.3 examines a unit process of dislocation-vacancy cluster interaction in bcc Fe over a broad range of strain rate conditions. We study the relation between the critical resolved shear stress (CRSS) and the strain rates, and observe an inverse behavior when strained slower than  $10^5\text{s}^{-1}$ . It is demonstrated that the dislocation obstacle interactions are determined by two competitive driving forces: strain rate and thermal activation. Different strain rates can affect the microstructures of the defects during the interaction, and eventually lead to the "V" shape like relation between the CRSS and loaded strain rates [39]. We show that even a unit process can induce an inverse behavior as well, which supplements the previous explanations of the inverse relation from the global point of view. The inverse behavior results in the decreased ductility and strength of the materials, and correspondingly generates the instabilities of materials during deformation [48, 49]. Therefore this study helps understand the origin of materials' instabilities on a microstructural level.

Chap 5 demonstrates how ABC based simulations can be connected to larger length-scale methods, to enable of multiscale modeling of microstructure evolution. There are many important phenomena, whose overall degradation is an aggregate of multiple modes of deformations, rather than determined by a dominant unit process [50]. Under such circumstances, it is not possible to directly deduce the macroscopic degradations from the atomistic simulations on a unit process. In contrast, it is necessary to find a higher level framework that can accommodate all the involved unit processes and treat these processes in a self-consistent manner. Correspondingly, one needs mesoscale models to connect atomistic to the engineering scale. The latter can be used to explain or predict the materials' macroscopic degradation by incorporating the microscopic degradation mechanisms and their kinetic descriptors. In this chapter, we discuss a suggested interface connecting our atomistic simulation to engineering scale method, in particular the

visco-plastic self consistent (VPSC) model developed at Los Alamos National Laboratory [51, 52]. A formalism to interface the atomistic results of this thesis to the VPSC is derived. An illustrative example of stress effect on the climb rate is provided. With this interface, a wider range of microscopic parameters from the atomic level can be provided into the higher level simulation models, which can predict and optimize the performance of the nuclear structural materials.

A summary is given in Chap 6, which discusses the importance of the simulation framework and results throughout the thesis. We particularly focus on the significance of combination between atomistic modeling and theoretical derivation in extending atomistic simulations to realistic time scales, and its broader impact on other scientific areas. We propose an analogy between the glass rheology and metal plasticity, and believe our method and framework developed in this thesis might shed light also on glassy systems.

## Chapter 2

# Methodology: Atomistic Simulations at Long Time Scales

This chapter presents the development of the simulation tools used in the later sections of the thesis. A specific goal here is to enable accurate methods simulating the system behavior over long time scales while retaining the atomistic details. In this chapter, we briefly introduce several well-known methods in slow dynamics and compare their advantages and drawbacks. We select the Autonomous Basin Climbing (ABC) method as the basis of our simulation technique throughout this thesis. We further advance ABC method by introducing new capabilities to it: i) identifying multiple transition pathways, which makes the prediction of kinetics more accurate, and ii) a dynamic implementation of ABC method, in order to directly simulate the dislocation-obstacle interactions at very low strain rate conditions.

### 2.1 Potential Energy Landscape

Properties of condensed matter rely on the interaction between the atoms in the system, governed by the landscape of the potential energy surface (PES) [53]. The relevant problems in the scope of this thesis, i.e. the degradation of structural materials, are non-equilibrium and evolve by the rare events transitions on the energy landscape. The activation barriers between the rare events are very high, and according to the transition state theory (TST), the system spends the bulk of the time (proportional to  $\exp[\Delta E/k_B T]$ , where  $\Delta E$  is the activation barrier) trapped in deep

energy minima. This time scale can be very long and molecular dynamics (MD) cannot be used to capture such rare events because of having to directly track the atoms' trajectories in time determined by Newton's equations.

The new school of thought in simulating the microstructural evolution at long time scale is based on identifying all the key unit processes of transitions between minimum energy states on the PES and coupling that information to TST calculations. Such a concept requires the capability of exploring the structure of PES and constructing the associated energy landscape in the evolution of the system.

## **2.2 Overview of Existing Atomistic Methods for Exploring PES**

### **2.2.1 Activation Relaxation Technique (ART)**

Activation relaxation technique (ART) [54, 55] is a method of searching the saddle points associated with a selected basin on the PES. The algorithm is the following: first relax the system to a local energy minimum using an appropriate interaction potential; then initiate the activation process, where the system is slightly perturbed along a random direction to create a nonzero term in the force. The configuration is then moved to a nearby saddle point by iterative application of a redefined force with the direction far from the initial local minimum. In sum, the system is forced to follow an up-hill trajectory in the energy landscape until the saddle point is found.

Once a saddle point is reached, the system is set back to the original state again and displaced along another random direction to find other saddle points associated with the given minimum state. All the observed saddle points and pathways are stored in the reaction catalogue, which serves as the input parameters for the following kinetic Monte Carlo (KMC) simulation.

The ART method has been applied to a series of studies, including the diffusion of point defects in bcc Fe and Si [56], heat transfer in amorphous Si [57], and the plastic flow in glassy materials [58].

### **2.2.2 Dimer Method**

Dimer method [59] is another atomistic technique of finding saddle points without knowledge of the final state in the transition. The algorithm first creates a replica of the system which is displaced slightly from the original configuration by a fixed distance. Then the dimer system is rotated in order to find the lowest curvature mode of the PES at the position where the dimer is located. By doing so the dimer system is forced to move uphill on the PES, from the vicinity of the initial state towards a saddle point. Along the way, the dimer is rotated in order to find the lowest curvature mode of the potential energy at the point where the dimer is located.

Similarly to the ART method, once a saddle point is reached in the dimer algorithm, the system is set back to the original state again and displaced along another random direction to find other saddle points. All the detected saddle points and pathways are served as the input parameters for the following KMC simulation.

The dimer method has been initially used to study the Al adatom motion on Al(100) surface [59] and chemical reactions [60]. Recently, the dimer algorithm has been further developed by Xu et al., named self-evolving atomistic kinetic Monte Carlo (SEAKMC) method, by incorporating the KMC processes and characterizing the environment on the fly [61-63].

### 2.2.3 Hyperdynamics and Temperature-Accelerated Dynamics (TAD) Methods

Besides the two methods introduced above for searching the saddle points on the PES, there are a family of techniques based on biased dynamics, e.g. hyperdynamics [64] and temperature-accelerated dynamics (TAD) [43] methods, to boost the rare event transition. According to TST, the expected transition time for a system trapped in a deep energy minima is proportional to  $\exp[\Delta E/k_b T]$ , where  $\Delta E$  is the activation barrier,  $T$  is the temperature. Correspondingly, there are mainly two biased approaches to boost the transition, which are reducing the activation barrier  $\Delta E$ , and increasing the temperature  $T$ , respectively.

The hyperdynamics method focuses on reducing the activation barrier  $\Delta E$ , by adding a biased potential  $\Delta V$  to the system's PES. Then the transition will be boosted by a factor of  $\exp[\Delta V/k_b T]$ . The hyperdynamics method has been applied to study the adatom diffusion on the fcc (100) surface in a Lennard-Jones system [65]. Although very appealing, there are important requirements on the form of the bias potential. Specifically, the biased potential must be zero at the dividing surfaces between the minima, which is a challenging task and requires very high associated computational load.

TAD method is based on the idea of speeding up the transitions by increasing the temperature, and then extrapolating to low temperature regime following Arrhenius behavior, while filtering out the transitions that should not have occurred at the required temperature. The TAD method has been applied to a series of studies, including the vapor-deposited crystal growth [66] and the Frenkel pair recombination in the vicinity of grain boundaries pre-loaded with interstitials [67].

## 2.2.4 Autonomous Basin Climbing (ABC) Method

The ABC method is an algorithm based on the activation-relaxation procedures, and explores and reconstructs the system's potential energy surface. It was developed by Kushima et al. in computing the viscosity of supercooled liquids [40], and is based on the Laio and Parrinello's idea of escaping from free energy minima[68]. Laio and Parrinello's method adds penalty functions to the free energy of a set of collective coordinates in an N-particle system in order to force the system evolve towards rare-event configurations, and in doing so, it requires a knowledge of possible reaction coordinates based on input from coarse grained molecular dynamics. On the other hand, ABC adds penalty functions to the potential energy of the entire 3N-dimensional space with no prior assumption of the reaction coordinates and with no need to acquire a set of forces from local MD simulations. Therefore, ABC method can serve extremely useful in finding the reaction paths and low-probability configurations without knowing the reaction paths or final configurations in advance. In ABC algorithm, a local minimum energy state,  $i$ , with energy  $E_i$  and configuration  $\{r_i\}$  is selected at the beginning (Figure 2.1 a:(1)). A series of penalty function additions and total relaxations are then operated in order to make the system climb out of the local basin and reach the next basin (Figure 2.1 a:(2)-(4)). While climbing up a potential hill (steps 1-3 in Figure 2.1 b), the total energy (indicated by black squares) is always larger than the original potential energy (indicated by red circles). When the total energy reaches above a saddle point, upon relaxation a sudden drop in the total energy takes place. This drop corresponds to a new minimum energy configuration that the system relaxes down to. Therefore, the total energy and the original potential energy at this point are equal (step 4 in Figure 2.1 b). The blue crosses represent the highest potential energy that the system reached during that last step. Then, the saddle point, shown by the green triangles in Figure 2.1.b, and the barrier between the neighboring minima, shown as  $E_{ij}$  and  $E_{ji}$  in Figure 2.1.b, are derived by tracing back the trajectories that the system underwent.



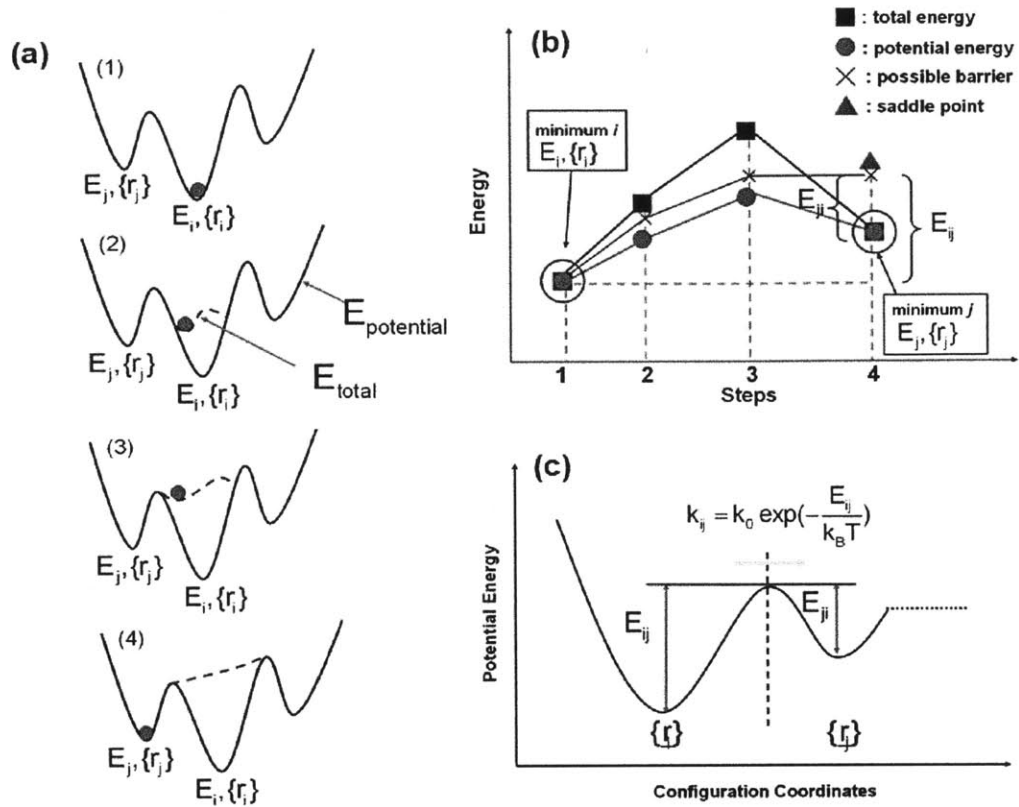


Figure 2.1: (a) Schematic illustration of the ABC method (Figure adapted from [40]). The system climbs out of a potential energy basin (1-3) by adding Gaussian penalty functions to the system's potential energy. Finally, the system reaches the neighboring minimum (4). (b) Trajectory of energy values (1-4) involved in the ABC method, corresponding to the case in (a). (c) Potential energy landscape derived from (b), and the KMC simulation parameters based on it.

While presented in detail by Kushima et al. in Ref.[40], here we summarize the key steps in the ABC algorithm:

(a) Select an initial local minimum-energy configuration  $r_i^0$  with energy  $E_i$ . The superscript "zero" represents that the configuration corresponds to a minimum.

(b) Activation step: add a penalty energy on the PES in a Gaussian function form,

$$\phi_1(\underline{r}) = W \exp\left[-\frac{(\underline{r} - r_i^0)^2}{2\Omega^2}\right],$$

to activate the system out of the minimum energy configuration.  $W$  and  $\Omega$  are prescribed constants which determine the strength and

spatial extent of the penalty function, respectively. The total system energy now becomes  $\Phi_p^1 = \Phi + \phi_1$ , where  $\Phi_p^1$  and  $\Phi$  represent the total energy and potential energy of the system, respectively.

(c) Relaxation step: relax the configuration and energy starting from that at  $\Phi_p^1$  to obtain the new energy and configuration  $\mathcal{L}_1$ .

(d) Repeat steps (b) and (c) with  $\Phi_p^2 = \Phi_p^1 + \phi_2$ ,  $\Phi_p^3 = \Phi_p^2 + \phi_3$ , ..., until a relaxation step,  $n$ , takes the system to a significantly lower energy state  $E_2$  with configuration  $\mathcal{L}_2^0$ .

(e) Confirm the sampling of the new local minimum energy configuration  $\mathcal{L}_2^0$  with energy  $E_2$ , by the criterion  $\Phi_p^n(\mathcal{L}_2^0) = \Phi(\mathcal{L}_2^0)$ . This means that the total energy equals to the potential energy at  $\mathcal{L}_2^0$  as the new local minimum.

(f) Repeat the operations (a)-(e) above to get a series of minimum energy configurations in the structural evolution of the system.

By collecting the energy barriers between the different minima, the inherent potential energy landscape of the structure evolution is constructed, as schematically illustrated in Figure 2.1.c.

Unless the penalty function strength represented by  $W$  is too large compared to the energy barrier between the two minima, varying the values of  $W$  and  $\Omega$  should give the same path of evolution between the energy minima. The uniqueness of the reaction path found by the ABC method using an appropriate set of values for  $W$  and  $\Omega$  was illustrated for atomic diffusion on a metal surface by Kushima et al in Ref.[40]. The smaller the penalty function strength, the more accurate the barriers derived in this algorithm are. However, the computational expense also grows with smaller magnitude of the penalty function. To balance the accuracy and computational efficiency, a penalty function that is not too small is first applied to get the correct reaction pathway, and then the initial state and derived final state are input to nudged elastic band (NEB) [69] to refine the value of the barriers.

## 2.2.5 Discussion on Different Techniques

We introduced five different long time scale atomistic techniques above. Among these methods, ART, Dimer and ABC are based on static (0 K) calculations, while the other two, hyperdynamics and TAD, are based on dynamic simulations at finite temperatures. Each method has its own advantages and drawbacks, and therefore is suitable for different applications. Below is a brief comparison of these methods.

ART and Dimer methods can both detect multiple transition pathways associated with a give minimum state, and therefore are particularly useful and accurate in the scenarios where there are many competitive transitions, e.g. in glass system [58, 70, 71], and the heavily damaged system [56, 61, 72]. However, the main drawback of this type of methods is the unaffordable computation load during the study of long term non-equilibrium evolution. The reason is that for a complicated non-equilibrium process, each minimum is connected with many other states, and each new observed state is connected with more states as well. Therefore the calculation can easily become of explosive magnitudes. For example, in a recent study on the annihilation of dislocation-dipole [73], Wang et al. showed that the ART could not drive the system to the final state due to the “very high associated computational load”, and had to employ the ABC method to observe the dipole dissociation processes.

For the two dynamic methods, hyperdynamics and TAD, an advantage is that the attempt frequency, which needs to be computed separately as input to ART, Dimer and ABC methods, is no longer necessary. It can be simultaneously identified as a result of the simulation. This advantage can provide more accurate results compared to having to fit the attempt frequency. In addition, no assumption of harmonic is being made in hyperdynamics [74]. This is another advantage since it can remove the approximation of harmonic transition state theory (HTST), which is employed in all other four methods, ART, Dimer, ABC and TAD. However, the boost factors of both the hyperdynamics and TAD are limited by the lowest barrier during evolution [74]. Therefore the system can be easily trapped in an oscillation between two neighboring states connected by small barrier, and will not be able to extend to long

time scale. On the other hand in hyperdynamics, the bias potential requires a diagonalization of  $3N$ -dimensional Hessian matrix, which makes the calculation extremely expensive. Recently there are further developments as variations to hyperdynamics [42, 75] to make the calculation of the bias potential more practical and accurate by introducing an adaptive boost (AB) method. In AB-MD, a smooth histogram of collective variables is first estimated by canonical ensemble molecular dynamics calculations. The histogram can thus be employed to estimate the bias potential in an adaptive manner. This procedure is not only more feasible than previous calculation of Hessian matrix in hyperdynamics, but quantitatively more accurate. This development has been successfully applied to study the diffusion of carbon atom in both bulk bcc Fe and near dislocation core [42]. Comparing with other techniques, ABC algorithm does not need to calculate the Hessian matrix of the PES, which is required in ART and hyperdynamics. Therefore the implementation of the ABC algorithm is technically more feasible. ABC method has been demonstrated in accurately capturing the mechanism and kinetics of a series of unit processes, including the unfauling of a self-interstitial atom (SIA) cluster in bcc Fe[76], the structure of vacancy cluster in fcc Al[77], the dislocation motion and structure [29, 73] and interaction of dislocation with obstacles in both hcpZr and bcc Fe[31, 39]. Most of these studies are accomplished as part of this thesis, as presented in the following chapters. In addition, a recent study demonstrated that the ABC method is computationally more effective than ART in studying the dislocation system [73]. Since the main scope of this thesis, as discussed in Chap 1, is to uncover the interactions between dislocations and obstacles, and due to the reasons mentioned above, all the studies throughout this thesis employed the ABC method.

## **2.3 Extension of ABC (ABC-E) Method**

Although the original ABC method has been demonstrated robust in a series of studies on different unit processes [29, 40, 41, 76-79], it can overestimate the system evolution time scale if there are multiple competitive processes because it evolves

the system as a one-dimensionally connected chain of transition events. In this section we introduce the underlying reason of the time overestimation by comparing ABC method with analytical TST and KMC results. Then we further modify ABC method into an extended version that is able to capture the multiple transition pathways from an individual basin on the PES.

### 2.3.1 Analytical TST and KMC

For a given transition network, according to TST, the evolution time from initial state (“*i*” in Fig.2.2) to final state (“*f*” in Fig.2.2) can be calculated as following:

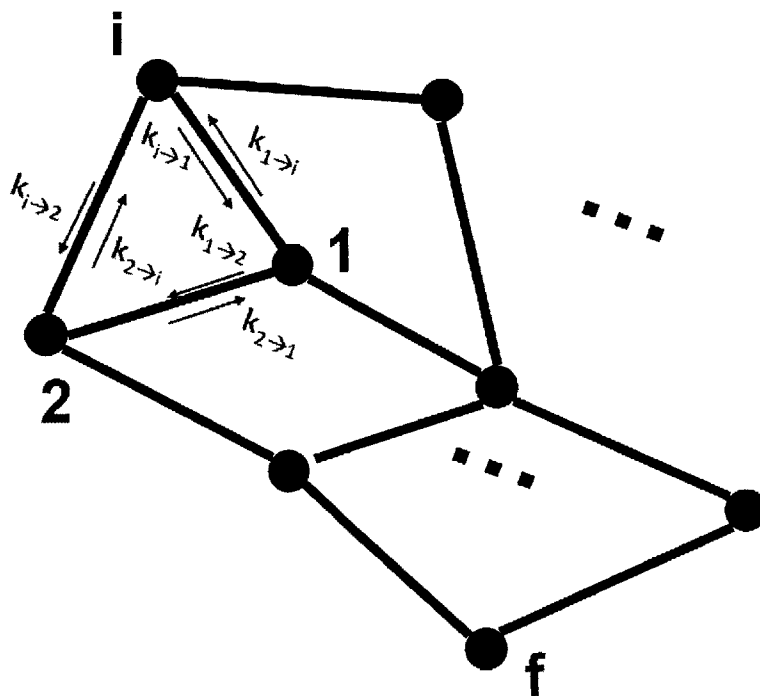


Figure 2.2. Illustration of a connected nodes network, with the initial state “*i*” and final state “*f*”.

If state *p* and *q* are connected with each other, following TST, the jump frequency from *p* to *q* can be derived by:

$$k_{p,q} = k_0 \exp\left[-\frac{E_{p,q}}{k_B T}\right]$$

where the prefactor  $k_0$  is the attempt frequency. The escaping time for state  $p$  is given by:

$$\tau_p = \frac{1}{k_{p,1} + k_{p,2} + \dots + k_{p,n(p)}}$$

where  $n(p)$  is the number of neighboring nodes connected with  $p$ .

The evolution time from  $i$  to  $f$  can therefore be calculated as:

$$t_{i \rightarrow f} = \tau_i + \frac{k_{i,1}}{k_{i,1} + \dots + k_{i,n(i)}} t_{1 \rightarrow f} + \dots + \frac{k_{i,n(i)}}{k_{i,1} + \dots + k_{i,n(i)}} t_{n(i) \rightarrow f}$$

and similarly, for other unknown variables such as  $t_{1 \rightarrow f}$ , there are also:

$$t_{1 \rightarrow f} = \tau_1 + \frac{k_{1,j}}{k_{1,j} + \dots + k_{1,n(1)}} t_{i \rightarrow f} + \dots + \frac{k_{1,n(1)}}{k_{1,j} + \dots + k_{1,n(1)}} t_{n(1) \rightarrow f}$$

⋮

We can rewrite above equations into the matrix expression as below:

$$\begin{pmatrix} 1 & -\frac{k_{i,1}}{k_{i,1} + \dots + k_{i,n(i)}} & \dots & -\frac{k_{i,n(i)}}{k_{i,1} + \dots + k_{i,n(i)}} & \dots & 0 \\ \frac{k_{1,j}}{k_{1,j} + \dots + k_{1,n(1)}} & -1 & \dots & \frac{k_{1,n(1)}}{k_{1,j} + \dots + k_{1,n(1)}} & \dots & 0 \\ \vdots & & & \ddots & & \vdots \\ & & \dots & & & \vdots \end{pmatrix} \begin{pmatrix} t_{i \rightarrow f} \\ t_{1 \rightarrow f} \\ \vdots \\ \vdots \end{pmatrix} = \begin{pmatrix} \tau_i \\ -\tau_1 \\ \vdots \\ \vdots \end{pmatrix}$$

The evolution time  $t_{i \rightarrow f}$  can be analytically derived by diagonalizing the  $n \times n$  matrix above, where  $n$  is the number of nodes in the system. In reality, the dimension  $n$  can be very large which makes the analytical solution very difficult to obtain. Therefore, KMC is widely employed to get the numerical solution and can usually reach very high accuracy for enough samplings.

## 2.3.2 1D Nature of ABC Method

Now let's revisit the transition network discussed in Sec 2.3.1 with ABC method. ABC algorithm evolves the system mainly towards the pathway with the lowest barrier, while neglecting other higher barrier pathways. Therefore, for the same system, ABC will provide an evolution chain that connects the transition paths in one dimension (1D) instead of a network (seen in Fig.2.3).

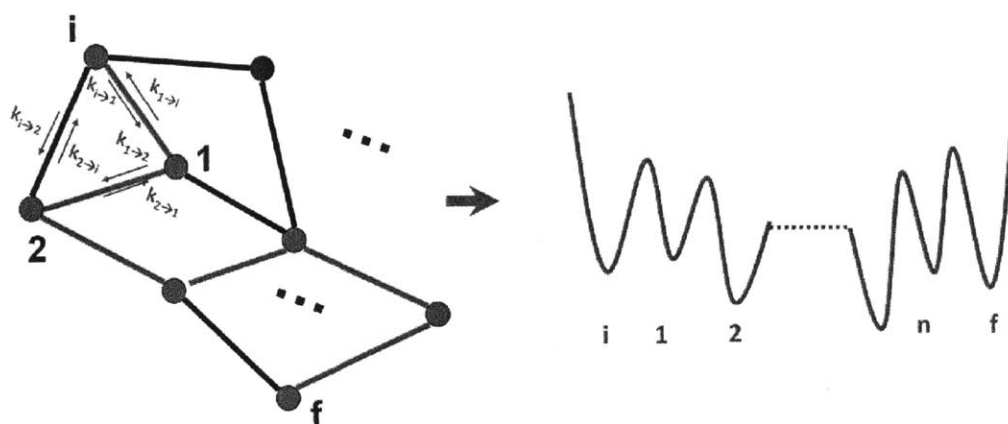


Figure 2.3 Illustration of ABC results on the same system as in Fig.1. An evolution chain is provided by ABC algorithm. The red path on the left corresponds to the PES of a one dimensional chain of transitions illustrated on the right.

Since for this 1D chain, each state is only connected with its left and right state, therefore the escaping time for state  $p$  is given by:

$$\tau_p = \frac{1}{k_{p,p-1} + k_{p,p+1}}$$

And similarly, the evolution time from  $i$  to  $f$  can be calculated by solving the following linear equations:

$$\begin{pmatrix} 1 & -1 & 0 & 0 & \dots & 0 \\ \frac{k_{1,j}}{k_{1,j} + k_{1,2}} & -1 & \frac{k_{1,2}}{k_{1,j} + k_{1,2}} & 0 & \dots & 0 \\ 0 & \frac{k_{2,1}}{k_{2,1} + k_{2,3}} & -1 & \frac{k_{2,3}}{k_{2,1} + k_{2,3}} & \dots & 0 \\ \vdots & & & \ddots & & \vdots \\ 0 & 0 & \dots & 0 & \frac{k_{n,n-1}}{k_{n,n-1} + k_{n,f}} & -1 \end{pmatrix} \begin{pmatrix} t_{i \rightarrow f} \\ t_{1 \rightarrow f} \\ \vdots \\ t_{n \rightarrow f} \end{pmatrix} = \begin{pmatrix} \tau_i \\ -\tau_1 \\ \vdots \\ -\tau_n \end{pmatrix}$$

The dimension for the above matrix is the length of the 1D chain, much less than the total number of nodes in the system. In addition, the matrix has the banded tridiagonal structure, which is much simpler than the matrix in the last section. KMC can be further employed based on this reduced matrix to calculate the evolution time  $t_{i \rightarrow f}$ . Because of the reduced dimension and simpler underlying mathematical structure, the ABC based KMC can save substantial computational load from the full catalogue KMC calculation.

Although has been demonstrated robust in a series of studies on different unit processes [29, 40, 41, 76-79], we observe the 1D nature of ABC method can lead to an overestimation of the system evolution time [80-82] if there are multiple competitive processes at the same time. To give an illustration we consider a synthetic comparison between ABC and full catalogue KMC using a pre-constructed hypothetical two-dimensional PES (Fig.2.4.a). The ABC trajectory was generated for the same prescribed initial state, and used to estimate the temperature-dependent system evolution time and the effective activation energy. Six different sets of activation penalty function parameters were employed, and all the runs gave the same governing transition pathway. To simulate a scenario with multiple processes, we randomly introduced 100 intermediate minima with varying depths and widths (seen in Fig.2.4.a) to form a rough energy landscape connecting the initial and final states. As shown in Fig.2.4.b, ABC gives the same effective barrier as full catalogue KMC, which demonstrates ABC is providing the dominant transition pathway. On



the other hand, the evolution time is overestimated by about 1~2 orders of magnitude in ABC method. This is a result of the 1D nature of the original ABC algorithm, because the residence time at each state is governed by  $1/(k_{forward} + k_{backward})$ , whereas in KMC simulations using a full catalogue of transition pathways,  $i$ , it is governed by  $1/\sum k_i$ . Therefore the evolution time calculated by ABC for a scenario with multiple competing processes can be overestimated.

### 2.3.3 Extension of ABC (ABC-E) Method

To address the challenge of time overestimation concern mentioned above, the ABC method is further modified by following algorithm: 1) After the first transition pathway is observed by ABC, put the system back to the original given basin while retaining the previously added penalty functions. 2) Add a repulsive potential function (also in Gaussian form) on the identified saddle point to block the observed lowest transition pathway. 3) While keeping the blocking functions, continue employing the routine ABC steps described above, then the transition with the next lowest saddle point should be observed. By performing these steps of iterations, a series of transition pathways associated with the given basin can thus be identified. Specifically, the procedure can be summarized as following:

1. Select initial state, apply regular ABC steps, until first neighboring state observed.
2. Record the new state, put the system back to original state, and add a blocking penalty function on the previously observed saddle point.
3. Implement regular ABC steps, until the next new minimum observed, then judge whether it's a new state or a previously visited state: (i) if it's previously visited, then put the system back to the original state, add another blocking function on the new saddle point, restart step 3: (ii) if it's a new step, goto step 2.

By doing so, a series of neighboring states to the original state are found. The order of finding these new states is with increasing activation barriers. The more states observed, the more accurate the results are.

The criteria for stopping the search for more states can be defined in two ways. An easy criterion is to set a maximum number of total penalty functions added in the entire simulation,  $N_{steps}^{MAX}$ , and consider all the identified transition pathways within these upper bound of search steps. Specifically, let us denote  $n_j$  as the number of penalty functions added before detecting the first connected state to the original minimum. Once the first connected state is found, the system is set back to the original state, following the procedures mentioned above. Let us assume it takes then another  $n_2$  steps to find the second connected state to the original minimum-energy state. The search is terminated after observing the  $i_{th}$  state, where

$$\sum_{j=1}^{j=i} n_j \leq N_{steps}^{MAX} < \sum_{j=1}^{j=i+1} n_j .$$

Although this selection of  $N_{steps}^{MAX}$  is somewhat arbitrary, the

calculation converges very well at large  $N_{steps}^{MAX}$ . For simplicity, we applied this criterion in this thesis, and our experiences on a hypothetical 2D PES and on the anisotropic diffusion of point defects in Zr suggest that a number of few hundred for  $N_{steps}^{MAX}$  is enough to get converged results. We can define a second, more accurate criterion as the following: Assume the number of already observed states is  $N_{states}^{obs}$ , with the associated barriers, from low to high, as  $E_1^{obs}, E_2^{obs}, \dots, E_{N_{states}^{obs}}^{obs}$ . Once a new state is found with the barrier  $E^{new}$ , we can compare the relative probability of this transition with respect to the previously observed states at a given temperature, by calculating

$$\alpha(T) \equiv \frac{\exp(-E^{new}/k_B T)}{\sum_{N_{states}^{obs}} \exp(-E_i^{obs}/k_B T)}$$

If the calculated  $\alpha(T)$  is very small, which means the new state has only negligible probability to be visited, then the searching process can be terminated. The rule of thumb for the specific value of  $\alpha(T)$ , following other similar truncation criterion used in TAD [43] and kinetic-ART methods [56], is around 0.1%.

In sum, the extension of ABC, now called ABC-E, is further implemented into the on-the-fly KMC framework, to obtain more accurate estimates of the kinetics of system evolution.

We revisit the same benchmarking problem at the end of section 2.3.2, now by ABC-E, and the results are shown in Fig.2.4.b. It can be seen that the results of ABC-E show a much better numerical accuracy, as expected.

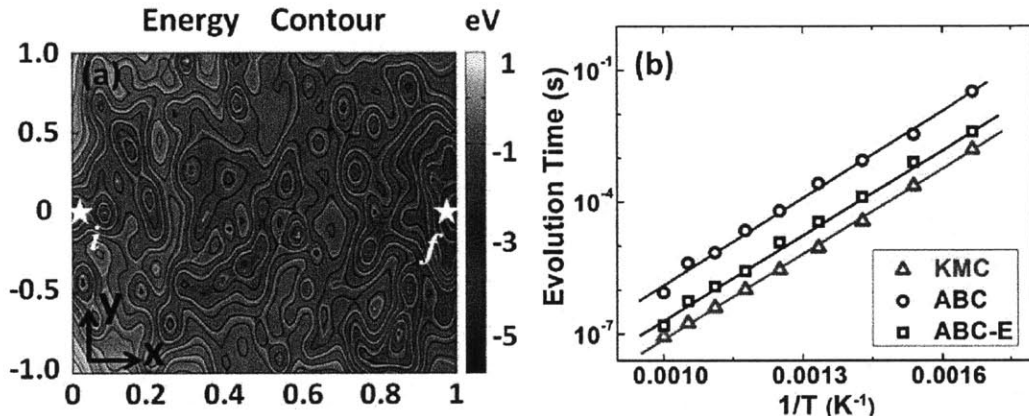


Figure 2.4 (a) A pre-constructed 2D PES with rough landscape, for representing the multiple processes scenario. (b) Variation of the evolution time with temperature sampled by full catalogue KMC, ABC (average of 6 runs), and ABC-E.

## 2.4 ABC Method in a Dynamic Scenario

ABC is essentially a method that explores the static energy landscape, while lacking an explicit time dependence. In reality, however, many processes are also driven by time-dependant dynamical parameters, e.g. with certain applied strain rates in the tensile experiments. Such dynamical factors drive the system's potential energy landscape with time, and therefore make it impossible to study within a single set of ABC samplings with a single initial configuration. To address this challenge,

we built a model which consists of consecutive ABC iterations to incorporate the strain rate effect on the dislocation-obstacle interaction (will be discussed in Chap 4). The approach is described in the following:

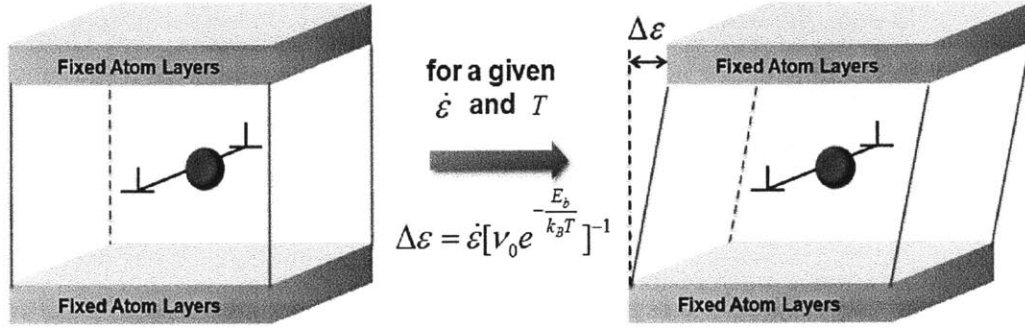


Figure 2.5 Illustration for the dynamic model in capturing the dislocation-obstacle interaction as a function of strain rate,  $\dot{\epsilon}$ , and temperature,  $T$ .

(i) Under a given strain condition, employ ABC to obtain the interaction mechanism and the reaction pathway.

(ii) Apply NEB method to calculate the energy barrier  $E_b$  between the initial and final states that are captured by ABC in step (i).

(iii) According to the TST, the expected thermal activation time is then given by  $\Delta t = [\nu_0 e^{-E_b/k_B T}]^{-1}$ , where  $\nu_0$  represents the attempt frequency and is set to be  $10^{13} \text{ s}^{-1}$  throughout this thesis (if not specified otherwise) as a first order approximation [83]. Consequently, for a certain applied strain rate condition  $\dot{\epsilon}$ , the required strain increment,  $\Delta\epsilon = \dot{\epsilon}\Delta t = \dot{\epsilon}[\nu_0 e^{-E_b/k_B T}]^{-1}$ , is applied to the system. Then restart step (i) under the new strain condition.

By iterating steps (i)-(iii), this algorithm permits us to study the dislocation-obstacle interaction under different strain rates and temperature conditions, and extend to lower strain rate regimes than traditional MD. In the iterations above, the strain is discretely induced into the system. In real experiments and MD simulations, however, the strain is continuously loaded. Therefore if the calculated increment  $\Delta\epsilon$  in step (iii) is too large, significant errors can be induced as an artifact. To address

this limitation, any strain increment larger than a critical value  $\epsilon_s$  during each step is forbidden, where the criterion  $\epsilon_s$  should be selected appropriately according to the system. Following the strategy of previous atomistic simulations on a dislocation system [84], we tested different incremental strain steps (from  $10^{-6}$  to  $10^{-4}$ ) in these static simulations, and compared the associated critical stresses and atomic configurations. We identified that the choice of  $10^{-6}$  and  $5 \times 10^{-4}$  provide identical atomic configurations, and have only small differences on the critical stress value (smaller than 5% of the critical stress). In order to optimize computational efficiency and accuracy, the value of  $\epsilon_s$  is set to be  $5 \times 10^{-4}$  in this thesis.

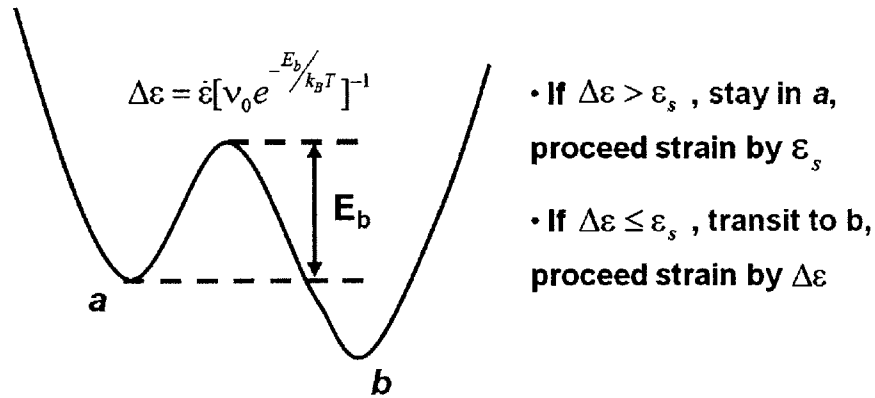


Figure 2.6 Strategy of accepting a transition event or not in the dynamic model of ABC method.

In sum, if the calculated  $\Delta\epsilon$  is smaller than  $\epsilon_s$ , then accept the transition and proceed the strain  $\Delta\epsilon$ . On the other hand, if the calculated strain increment is larger than  $\epsilon_s$ , directly applying  $\Delta\epsilon$  into the system can introduce non-negligible artifacts to the structural evolution of the defect due to a large strain applied in one step. Therefore under such a circumstance, only an incremental strain of  $\epsilon_s$  is induced into the system, while the transition event is not accepted and the system is put back into the prior configuration.

## Chapter 3

# Point Defects: Structure Evolution, Accumulation, and Migration

Irradiation creates point defects in the material. The structural evolution of point defects and their interactions with dislocations are critical to understand and predict the effects of radiation on mechanical properties of the nuclear materials. In this chapter we consider the two types of point defects, the self-interstitial atom (SIA) and vacancy, in both bcc Fe and hcp Zr. Several important processes, including the sessile defect unfauling mechanism, vacancy accumulation and point defect diffusion, have been studied by ABC or ABC-E methods. The reported results are compared with available experiments and other simulation studies. The work in this chapter helps elucidate the evolution of point defect cluster structures and diffusion at long time scales. The understanding on point defects also serves to prepare for Chapter 4, where their interactions with dislocations will be discussed.

### 3.1 SIA Cluster Unfauling in BCC Fe

#### 3.1.1 Background and Motivation

SIA cluster is a common type of irradiation induced defect. In bcc Fe, previous MD studies showed that SIA clusters are likely composed of parallel  $\langle 111 \rangle$  crowdions and do one-dimensional gliding migration with a very low activation barrier [85-89]. The observations of  $\frac{1}{2}\langle 111 \rangle$  SIA loops' 1-D movement in bcc Fe

by transmission electron microscopy (TEM) experiments support the MD predictions of this process qualitatively [90]. However, the resistivity recovery experiments in irradiated bcc-Fe upon small-dose irradiation suggested that the activation barriers for small SIA clusters are much higher than the MD prediction [91, 92]. This discrepancy indicates that, even for the small SIA clusters, some stable and non-parallel structures might be formed, which could impact the materials' microstructural evolution. The behavior of the small non-parallel SIA clusters could serve as the unit initiation process for the migration and evolution of larger size defects, especially those associated with slow dynamics. However, these stable structures have not been thoroughly probed until only recently. In this context, Terentyev et al. proposed the non-parallel configurations (NPC) of small SIA clusters (2-, 3-, and 4-SIA clusters) [93] as candidates of stable SIA structures. The authors studied these NPC SIA clusters by density functional theory (DFT) calculations and MD simulations with a recent embedded atom method (EAM) potential developed by Ackland, Mendeleev and Srolovitz (AMS) [94]. Their results proved that the NPC structures are much more stable than the parallel  $\langle 111 \rangle$  crowdions. Furthermore, by fitting the Arrhenius relation between temperature and the life time of the NPC SIA clusters as found from MD simulations, they calculated the effective activation barrier for the evolution from NPC SIA cluster state to the glide  $\langle 111 \rangle$  for the 2-, 3-, and 4-SIA clusters. The result for the 2-SIA cluster was  $0.43 \pm 0.08$  eV, which was consistent with the value  $0.42 \pm 0.03$  eV given by resistivity recovery experiment [91, 92] and by ab initio calculations [95, 96]. The effective barrier for the unfauling of the 4-SIA cluster was reported to be much higher,  $1.68 \pm 0.29$  eV. However, the details of the unfauling mechanism and the corresponding evolution in energy for NPC SIA clusters were not provided. That is because an MD simulation cannot provide easily the complete picture of the energy landscape associated with each possible atomic configuration in the long-time scale evolution of an SIA structure. On the other hand, a comprehensive understanding of the potential energy landscape can help elucidate the system's atomic structure evolution and the corresponding kinetics [53]. Therefore in this section, we would

like to explore the detailed energy landscape associated with SIA structure evolution by ABC method, and particularly focus on the effective energy barriers and time scales governing the structural evolution.

### 3.1.2 Problem Statement and System Set Up

Based on the energy landscape for the evolution of the SIA clusters by ABC method, the barriers between the different minimum energy configurations are served as input parameters to an on-the-lattice KMC simulation, without any other assumptions or parameterization. The effective migration barrier and the evolution time between the initial state and final state were then calculated by the KMC simulations.

It is worth reminding here that the static potential energy landscape calculations involved in the current form of the ABC algorithm bare no information on the entropy contribution to the energy. The structure of the algorithm does not prohibit to include the entropy contributions in future development, provided the degeneracy of inherent structures and configurations of saddle points and minima. On the other hand, the entropy is not a significant contributor to the energy barriers in such cases as when the temperature is low or when the potential energy difference is very large. Those cases are of particular importance to slow dynamics in the evolution of trapped structures, as in radiation damage at relatively lower temperatures. In such cases, the KMC simulations based only on the potential energy surface could enable sufficiently good estimate of the energy barriers.

The effective migration barrier calculated by the ABC and KMC methods is then benchmarked against MD simulations of the same type of NPC SIA clusters. The supercell in the simulation is cubic with  $10a_0 \times 10a_0 \times 10a_0$  dimensions, and containing 2004 Fe atoms in total. Interstitial atoms are inserted into the supercell according to the NPC structure proposed by Terentyev et al.[93]. For comparison purposes, we employ the same type of EAM potentials developed by Ackland et al. [94]. To enable statistically sufficient number of MD tests under each temperature, we consider the following criterion, resulting in Eq.(3.3) below. The microstructural



evolution of SIA clusters is a state transition process. According to the TST, the probability distribution function,  $p(t)$ , for the time,  $t$ , of first escape from one energy basin is:

$$p(t) = k \exp(-kt), \quad (\text{Eq.3.1})$$

where  $k$  is the total jump frequency to neighboring minima.

The average time that the system stays in the given energy basin is the mean life-time,  $\bar{t}$ , of the configuration in the basin, and is given by,

$$\bar{t} = \int_0^{\infty} k \exp(-kt) t dt = \frac{1}{k}. \quad (\text{Eq.3.2})$$

The standard deviation,  $\sigma$ , of the life-time is then derived as,

$$\sigma = \sqrt{\sigma^2} = \left( \int_0^{\infty} k \exp(-kt) (t - \bar{t})^2 dt \right)^{1/2} = \sqrt{\frac{1}{k^2}} = \frac{1}{k}. \quad (\text{Eq.3.3})$$

Theoretically, this result implies that the mean value of the life-time,  $\bar{t}$ , should be exactly the same as its standard deviation,  $\sigma$ . Therefore, the number of MD tests should be sufficiently numerous when the calculated average life-time converges to a value close to its standard deviation.

### 3.1.3 Results

#### (i) Unfaulting Mechanism of SIA Cluster

The 4-SIA NPC structure described by Terentyev et al. [93] is selected as the starting point in the simulations. After relaxation the initial configuration, C1 in Figure 3.1, consists of 12 interstitial atoms and 8 empty lattice sites, which gives a net number of 4 interstitials. Among these, 3 interstitial atoms and 2 lattice sites form the  $\langle 111 \rangle$  crowdion, while the remaining 9 interstitial atoms and 6 lattice sites form a ring structure of three trimers on (111) planes. The evolution trajectory and the corresponding energy landscape as derived by the ABC method with the AMS potential is also shown in the figure.

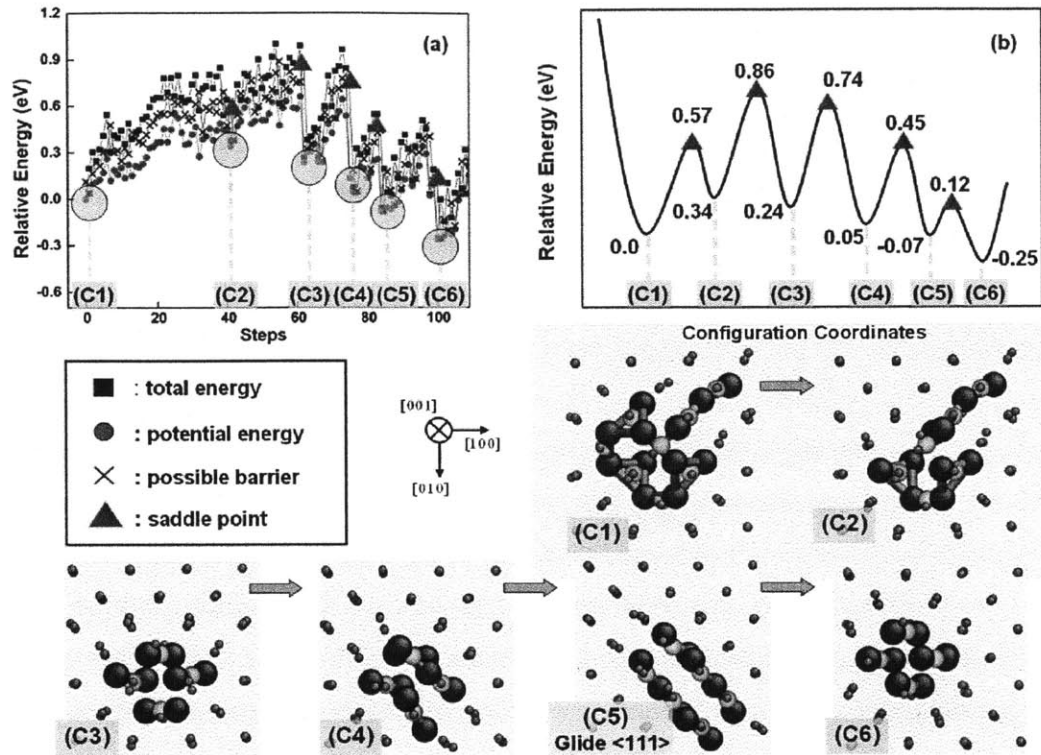


Figure 3.1 (a) The evolution of energy and atomic trajectories (C1-C6) starting with the initial NPC 4-SIA cluster, found by using the ABC method with the AMS potential (visualized by Atomeye[97]). Blue balls represent the interstitial atoms, green balls represent the vacant lattice sites, small orange balls represent the atoms on lattices. The grey rods are placed only to accentuate the defect structure, but do not represent a physical meaning for a special set of bonds. (b) The potential energy landscape associated with the atomic configurations described in (a).

After being activated by the energy penalty function, the next minimum energy configuration is C2. In C2, the  $\langle 111 \rangle$  crowdion remained unchanged, while the ring structure of three trimers was broken up due to the returning of the interstitials in one of the trimers back to the nearest vacant lattice sites. Upon further activation, C3 was found as the  $\langle 111 \rangle$  crowdion rotated to a  $\langle 110 \rangle$  dumbbell, and consists of three parallel  $\langle 110 \rangle$  dumbbells and another  $\langle 110 \rangle$  dumbbell perpendicular to the other three. Then, two  $\langle 110 \rangle$  dumbbells in C3 rotated to  $\langle 111 \rangle$  direction. Therefore, C4 consists of two parallel  $\langle 110 \rangle$  dumbbells and two parallel  $\langle 111 \rangle$  dumbbells. Evolution of C4 to C5 involved the two  $\langle 110 \rangle$  dumbbells rotating to the

$\langle 111 \rangle$  direction, ending up together as the glide  $\langle 111 \rangle$  configuration. Finally, C6, which consists of 4 parallel  $\langle 110 \rangle$  dumbbells, is the lowest energy structure of the 4-SIA cluster. These two last states, C5 and C6, found in this transition are qualitatively consistent with Terentyev et al.'s results. Furthermore, a detailed set of transition state configurations in the unfauling process from the trapped to the mobile glide  $\langle 111 \rangle$  configuration were thus identified at the atomic level and associated with the energy landscape (Figure 3.1) for the first time with the ABC method in our investigation. In this process, the transitions  $C1 \rightarrow C2$ ,  $C2 \rightarrow C3$ ,  $C3 \rightarrow C4$  have similar activation barriers, 0.57, 0.52, and 0.50 eV, respectively, that are higher than the other two remaining transitions in the unfauling. Therefore, based on the activation barriers, the breaking of the initial ring structure of three trimers in (111) planes followed by the rotation of the  $\langle 111 \rangle$  crowdion are the rate limiting processes of the unfauling mechanism.

## **(ii) Life Time and Effective Activation Barrier**

The effective activation barrier in the transition from 4-SIA NPC to glide  $\langle 111 \rangle$  configuration, is obtained by the KMC simulations based on the energy landscape produced above by ABC method. In the KMC simulations, the system was initially set at configuration C1 made of the non-parallel SIA cluster shown in Figure 2, and the simulation was terminated when the system reached C5, the glide  $\langle 111 \rangle$  configuration. 10000 KMC simulations were performed under each temperature. Figure 3.2 shows a clear Arrhenius relation between the unfauling time and temperature with a slope of  $0.82 \pm 0.01$  eV, which gives the effective activation barrier. The advantage here is that the configurations and the corresponding energy barriers in KMC are not presumed, but rather precisely described by the results from the ABC method.

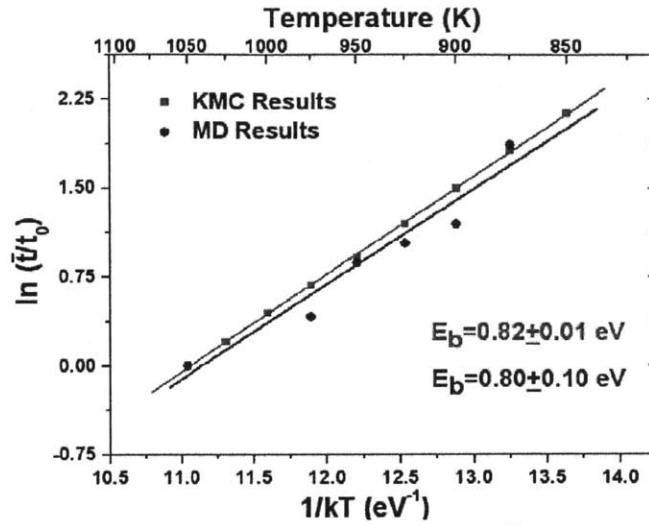


Figure 3.2 Arrhenius relation between the mean life-time,  $\bar{t}$ , of NPC 4-SIA cluster and temperature, T (the life time at 1050K was set as  $t_0$ ), with an effective energy barrier of  $E_b$  derived from KMC simulations, and MD results, respectively.

Compared with the migration barrier for the glide  $\langle 111 \rangle$  movement (tens of meV [85-87]), this value of 0.82 eV corresponds to a very high activation energy for the unfauling of the NPC 4-SIA cluster. This means that the configuration C1 is a rather stable structure, consistent qualitatively with Terentyev et al's conclusion. In our investigation, the effective activation barrier calculated from the ABC and KMC simulations is benchmarked against MD tests using the same EAM potential. Configurations C2 and C3 were also found in the MD simulations, which is consistent with the evolution trajectory given by the ABC method. C4 was seldom found in the MD simulations at these rather high temperatures because the barrier between C4 and C5 is relatively low. The quantitative results for the unfauling time taken from the MD results are shown in Table 3.1.

As seen in Table 3.1, the calculated mean life-time and its standard deviation are sufficiently close to each other. This implies statistical reliability of the MD-driven results, based on the criterion described by Eq.(3.2) and Eq.(3.3). Using the mean life-time versus temperature data, which obeys the Arrhenius behavior as shown in Figure 3.2, the effective activation energy in transition from NPC cluster to glide  $\langle 111 \rangle$  cluster with the MD benchmark tests is  $0.80 \pm 0.10$  eV.

Table 3.1: The mean and the standard deviation of the life-time in the unfauling of the NPC 4-SIA cluster found from the MD simulations using the AMS potential.

Temperature (K)	Mean lifetime (ps)	Standard deviation (ps)
1050	18.65	30.08
975	28.20	34.09
950	44.44	39.78
925	52.50	54.25
900	61.72	49.16
875	120.47	99.07

The MD results of 0.80 eV are clearly consistent with the 0.82 eV effective barriers calculated by the ABC and KMC simulations. As noted in the Sec 3.1.2, the KMC results based on the ABC-driven energy barriers here do not include entropy contributions. The reason that they are well consistent with the MD-driven energy barriers could be that the entropy difference between the initial point, C1, and the main saddle point located between C2 and C3 determining the barrier for the unfauling process is very small compared to the potential energy difference between them. The consistent benchmarking of the results with the MD tests proves that the ABC method is quantitatively capable of capturing the transitions in the atomic structure of the SIA clusters and the corresponding energy landscape.

### 3.1.4 Discussion

It is noted that, the derived values are significantly different from the 1.68 eV given by Terentyev et al's MD results using the same AMS potential. According to the criteria we described in Eq.(3.3), the MD results for estimating the life-time in this transition states context can be statistically acceptable only when the standard

deviation is close to the calculated mean life-time. However, only one MD result data point was provided for the life-time at the relatively low temperature around 800 K by Terentyev et al. in [93]. Therefore, the mean and the standard deviation of the life-time calculated in Ref. [93] for the 4-NPC SIA cluster around 800K is not clear quantitatively. Such a low number of MD runs at the given temperature could be the cause for the loss in accuracy of the unfaulting energy barrier result reported by Terentyev et al. for the NPC 4-SIA cluster.

Another point worth mentioning here is the time-savings with the ABC simulations when compared with MD, and we give an example for this comparison. In this paper, the mean life-time of the NPC cluster is about 100 ps in the temperature range of 800K-1000K. It takes  $10^5$  steps for a single MD test with a time step of  $10^{-15}$ s to capture the transition with this life-time. Furthermore, considering several temperatures and approximately 10 to 20 MD tests at each temperature for achieving statistically reliable results, the total time-steps consumed in the MD simulations amount to about  $10^7$ . On the other hand, with the ABC method, a number of several hundred simulation steps is sufficient for a typical transition trajectory (Figure 3.1.a). Although a step in ABC method is longer than in MD (about  $10^3$  times longer), the total simulation time consumed by the ABC simulations is considerably less. In this case of study, ABC method is more than 10 times faster than the MD simulation. This advantage is expected to be more significant for processes associated with slow dynamics, which is with very high transition energy barriers and at relatively lower temperatures.

In sum, the consistency between ABC and MD results in this case study indicates that the ABC method is capable of capturing the transitions in the atomic structure of the SIA clusters and the corresponding energy landscape. It therefore suggests that the simulation method development based on the ABC principles can be particularly useful in predicting how the macroscopic mechanical and chemical properties change in an irradiated material while retaining atomistic fundamentals, which is known as the ultimate challenge in simulating long time scale behavior upon radiation damage in nuclear materials.

## 3.2 Vacancy Accumulation in BCC Fe

### 3.2.1 Background and Motivation

There are five generally accepted stages in radiation damage recovery process [98]. In bcc Fe, they are: stage I ( $\sim -150^\circ\text{C}$ ), migration of self-interstitial atoms (SIA); II ( $\sim -100^\circ\text{C}$ ), long range migration of SIA clusters; III ( $\sim 0^\circ\text{C}$ ), single vacancy migration; IV, migration of vacancy clusters; and stage V ( $\sim 250^\circ\text{C}$ ), thermal dissociation of vacancy clusters. The existence and dominant mechanism of stage IV have long been controversial [92, 98, 99], depending on material, impurities and irradiation conditions, as illustrated in Figure 3.3.

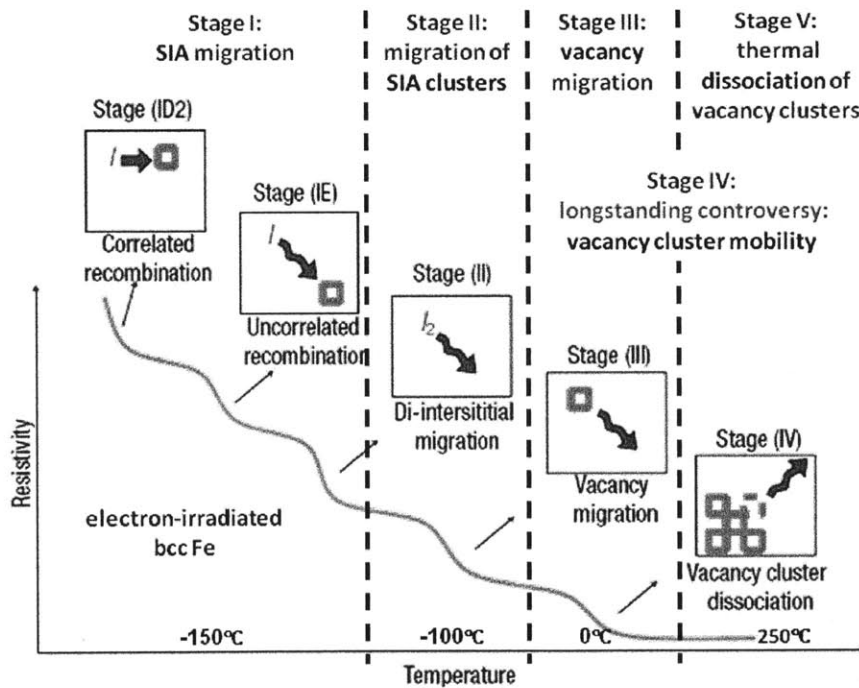


Figure 3.3 A schematic plot of different stages during the resistivity recovery experiments in Fe. Among these stages, stage IV is longstanding controversial. Under electron irradiation conditions, the vacancy cluster motion stage is missing, while it exists under neutron irradiation conditions. (The plot is adapted from Ref.[91])

In this case study, we would like to elucidate the conditions and the mechanism governing stage IV in pure bcc Fe, as this is the important step in incipient void growth and swelling.

In the following part of this section, we present atomistic details to show this transition stage (stage IV) is governed by the mobility and aggregation of small vacancy clusters of size less than ten vacancies, which match quantitatively with recent positron annihilation spectroscopy (PAS) experiments on neutron irradiated single crystal bcc Fe [100]. Our predicted transition temperature of 150 °C lies between stages III and V that was observed in the damage recovery upon electron irradiation [92]. These results indicate the existence of stage IV in bcc Fe under vacancy supersaturated conditions. The sizes of defects captured in our simulations are directly within the detection capability of the PAS technique in characterizing small vacancy clusters [100-104].

### **3.2.2 Problem Statement and System Set Up**

We use a cubic supercell with  $10a_0 \times 10a_0 \times 10a_0$  dimensions for the ABC simulations. The system initially contains 50 randomly distributed single vacancies to represent a vacancy supersaturated structure in the central collision region after a displacement cascade [105] in single crystal bcc Fe. We employ the same EAM type potential that has been used in Sec 3.1.

Following the strategy in Sec 2.2.3, the initial state and detected final state in ABC method are input to NEB to refine the value of the barriers. In each NEB calculation, 10 images are applied between each pair of initial and final states, and 229 successive minima states on the PES are explored in this case study. In the KMC simulations, as a first-order approximation, each energy minimum is connected only with its immediately preceding and following minima. A total of 200 KMC simulations are performed to attain reliable statistics.



### 3.2.3 Results

Figure 3.4 (a) shows the sequence of atomic configurations sampled by ABC with initial configuration C1. At the early phase (C2), the single vacancies migrate to combine with nearby vacancies to form small vacancy clusters. The di- and tri-vacancy clusters are able to migrate over longer distances, while clusters of size four and larger are less mobile and undergo only shape changes toward more stable configurations. In C3 and C4 the larger clusters grow by absorbing the mobile defects, particularly mono-vacancies and di- or tri-vacancy clusters, while in C5 and C6 cluster growth is governed by aggregation of two less mobile clusters as discussed below and shown in Figure 3.4 (b).

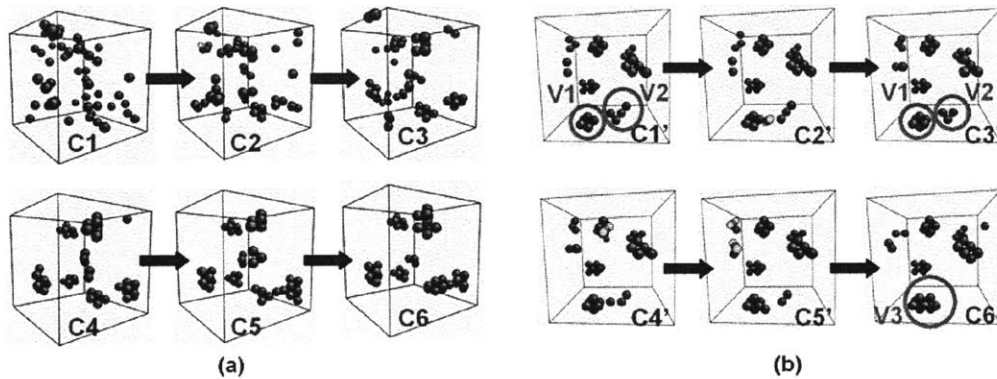


Figure 3.4 (a) Sequence of atomic configurations of vacancies in bcc Fe generated by ABC sampling (lattice atoms not shown) with initial configuration C1 consisting of 50 single vacancies. (b) Sequence of vacancy configurations depicting the reaction between two vacancy clusters,  $V1+V2 \rightarrow V3$ . Blue balls represent the inserted vacancies, and red balls and green balls represent the interstitial atoms and vacant lattice sites, respectively, that arise during the vacancy cluster structure evolution.

Figure 3.4 (b) illustrates the interaction between two relatively immobile vacancy clusters of size 6 (V1) and 4 (V2), in which the smaller cluster dissociates by emitting one vacancy at a time, and the dissociated vacancies migrate toward V1. The process ends with V2 becoming a cluster of 10 vacancies and V1 disappearing. This is a demonstration of Ostwald ripening mechanism at the atomistic level [106].

It is also observed that in a defect supersaturated system as this one, the defect-defect interaction pathways and energetic barriers can depend strongly on the local structure. We demonstrate one such example explicitly for the vacancy migration in the vicinity of a void, shown in Figure 3.5. It can be seen that a mono-vacancy migrates and joins a small cluster with a barrier of 0.44 eV. This value is considerably smaller than the vacancy migration barrier in bulk, found as 0.63 eV using the AMS potential [107]. It is worth reminding this effect and our capability to capture such dependencies without presumed interaction paths and parameters. If these dependencies are not captured during the evolution of the system, this would ultimately lead to inaccuracies in assessing the kinetics at long times.

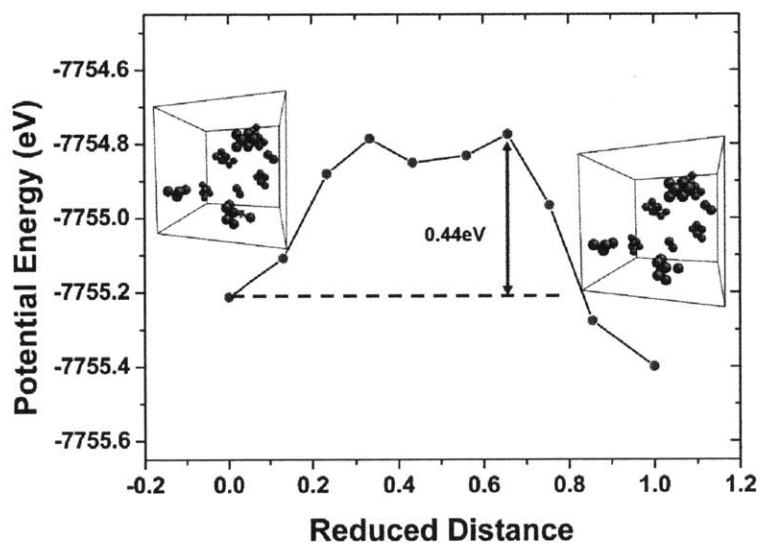


Figure 3.5 The migration barrier for a single vacancy near a small cluster. The barrier 0.44 eV is considerably smaller than 0.63 eV, the vacancy migration barrier in bulk [107].

In the simulations shown in Figure 3.4, the clusters range in size from a single vacancy to 16 vacancies. This range is ideally suitable for direct comparison with PAS measurements on temperature dependent size distribution of vacancy clusters [100, 101]. It has been observed in bcc Fe [100] that the number of clusters with 6 or fewer vacancies undergoes a sudden drop at a temperature around 150 °C, while correspondingly the number of larger vacancy clusters increases significantly. For

the purpose of interpreting these results we focus on simulations in which the starting configuration had vacancy clusters of average size around 6 vacancies per cluster, consistent with the state at the beginning of the PAS measurements in Ref.[100]. The potential energy landscape for the system evolution (exemplified in Figure 3.4) is constructed by from 228 NEB calculations based on 229 successive minimum energy states explored by the ABC method. The resulting PES is shown in Figure 3.6 (a). The average size of vacancy clusters is seen to increase from 6 to 9, while the system systematically evolves toward lower energy configurations.

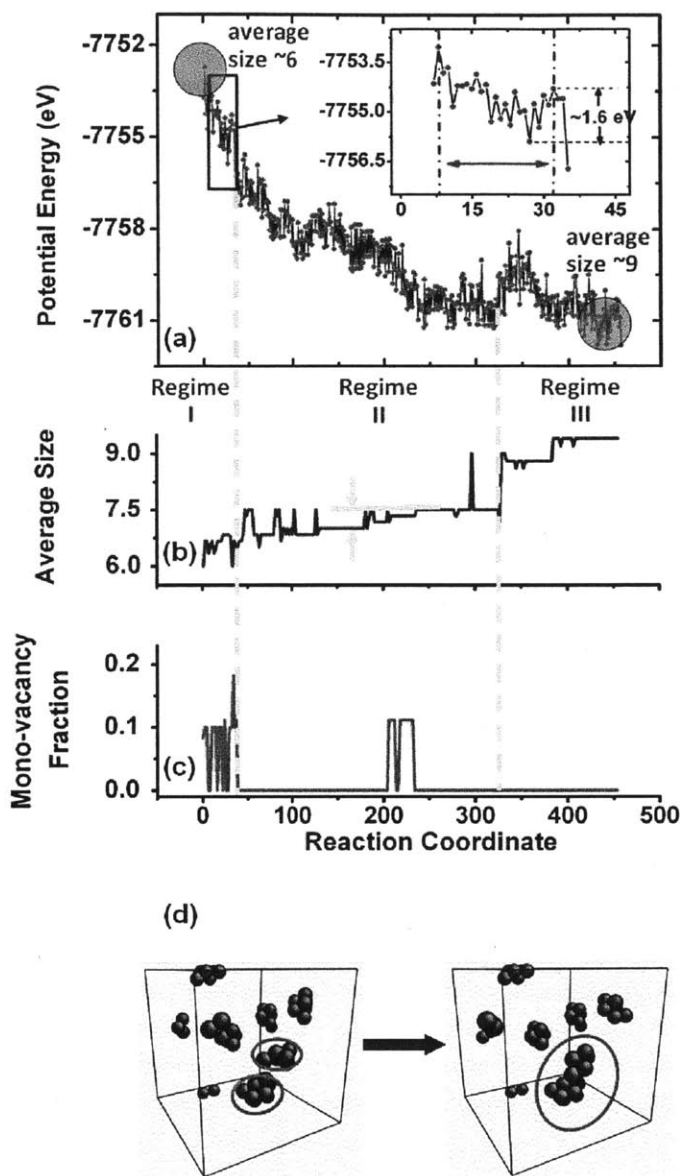


Figure 3.6 (a) The PES associated with a subset of the structural evolution shown in Figure 1(a), with initial and final average clusters of 6 and 9 vacancies, respectively. Inset: A region on the PES where the system is trapped in the early stages of evolution. (b) The average vacancy cluster size associated with the PES in (a). (c) Fraction of mono-vacancies among all the defects during structural evolution. (d) Evolution of vacancy clusters corresponding to the size increase seen in Regime III in (b).

On the basis of the energy landscape thus produced, the temperature and time dependence of the average cluster size are then obtained by KMC simulations. Using initial configurations (same as at the beginning of the PES in Figure 3.6) which have an average cluster size of 6 the simulation is terminated when the average cluster size reaches 9. The initial temperature and annealing rate  $\alpha$  are set at 50 °C and 0.01 K/s, respectively, the conditions reported in the PAS experiments [100]. The temperature in the KMC simulation should increase smoothly, in order to realistically represent the experimental conditions. However, the temperature increment  $\Delta T = \frac{\alpha}{k_0} \cdot \exp[E/k_b T]$  can be too large and abrupt when overcoming a larger barrier  $E$ . In our study, if the temperature increment is too large ( $\Delta T > 20$  K), a self-consistent method is employed to calculate the realistic temperature increment:

$$\Delta T = \frac{\alpha}{k_0} \cdot \exp[E/k_b (T + \Delta T)] \text{ (Eq.3.4)}$$

where  $T$  is the current temperature of the system.

Figure 3.7 shows the temperature variation of the average vacancy cluster size predicted by our KMC simulations over a time duration of about  $2 \times 10^4$  s. The intensity data from PAS experiments are also shown in the same plot [100]. To compare the temperature dependence of cluster size prediction with intensity measurements, the two results are normalized (admittedly arbitrarily) at a temperature of  $\sim 120$  °C in the middle of the plateau region. In the simulated results, below 150 °C the clusters are stable and exhibit a slow increase in average size from 6 to 6.5. This is because the defect clusters are rather immobile and do not interact much with each other. In this temperature range the activated processes with low barriers are migration of mono-vacancies and shape change of vacancy clusters. From the potential energy landscape perspective the system is trapped in a local minimum and the thermal fluctuations are not sufficient to activate cluster evolution. This minimum is shown in the inset of Figure 3.6 (a). The entry barrier from left side into this region is lower than 1 eV, which makes the process feasible at low temperatures ( $< 150$  °C). Once the system is in this region, however, further

evolution forward or backward is hindered by high barriers. To evolve forward out of this minimum, the system needs to overcome an effective activation energy of around 1.6 eV, which implies a relatively high transition temperature or a nearly constant average cluster size below the transition temperature (see Regime I in Figure 3.6 (b)). When the temperature exceeds 150 °C, the system is able to overcome the forward barrier. At the same time at this temperature the remaining mono-vacancies disappear, as seen from the sudden drop of the red plot in Figure 3.6 (c). Correspondingly cluster size begins to grow. The step from Regime II to III in Figure 3.6 (b) is associated with the onset of the Ostwald ripening process discussed above. The spike in Figure 3.6(c) at reaction step 200 represents the re-appearance of mono-vacancies in the Ostwald ripening process (see Figure 3.4 (b)). A significant increase of the average size occurs in the transition to Regime III. The governing mechanism here is the aggregation of two clusters (containing 6 and 10 vacancies, respectively) into a single cluster, as shown in Figure 3.6 (d). The significantly larger standard deviation in the average size seen at 175-200 °C is consistent with the enhanced fluctuations expected in the transition temperature range.

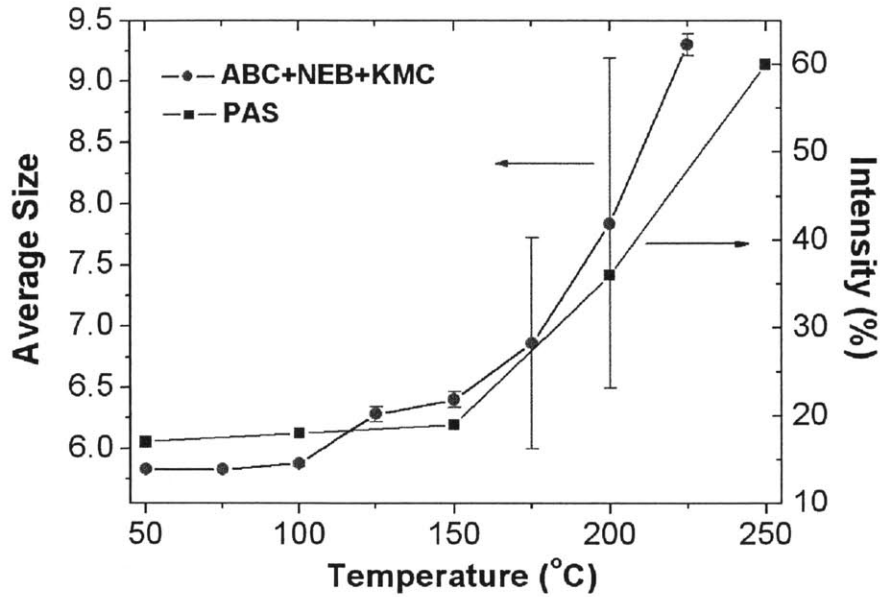


Figure 3.7 Temperature dependence of the average cluster size (red points) simulated by KMC based on the PES in Fig. 2(a), and the PAS data (blue points) [100] showing the relative intensity of vacancy clusters with size larger than ten.

This finding suggests that 150 °C is a transition temperature for enabling the migration of vacancy clusters in a vacancy supersaturated bcc Fe that leads to their accumulation via the atomistic mechanisms demonstrated in Figure 3.4(b) and Figure 3.6 (d). This characteristic temperature therefore delineates the damage recovery stage IV, the existence of which has been controversial in the experimental literature. In the case of electron irradiated iron, only stages III (~0 °C) and V (~250 °C) were observed [92]. This is because only a low density of vacancies is produced upon electron irradiation, making cluster formation and survival difficult. In neutron irradiation it is possible to induce a super-saturation of vacancy defects, thus a higher probability to form clusters and survive up to higher temperatures [98]. Our simulation conditions and results correspond more closely to the latter.

### 3.2.4 Discussion

While we have simulated a model bcc Fe system that was used in experiments, in real alloys impurities can be expected to significantly affect the defect reaction kinetics, and therefore warrant further studies. For example, the presence of C increases the vacancy migration barrier in bcc Fe [108] which could lead to an increase in the transition temperatures [92], and strong hydrogen-vacancy interactions are known to play an important role in determining the energetics and concentrations of point defect clusters [109]. In extending the present work to impurities, the ability of ABC to selectively activate a local region (down to one atom) should prove to be advantageous.

On the other hand, Brommer et al. recently revisited this case [80] study by employing another technique, kinetic ART, which has been introduced in Sec 2.2.1. They reported a much shorter time scale than our results. In this thesis, we offer two observations concerning the large discrepancy. First, a series of applications with ABC method [29, 40, 41, 76-79] suggests that it is a simple and robust algorithm for escaping from potential energy surface (PES) minima, as well as providing the dominant pathway. However, it is likely to give an overestimation because of the 1D nature of sampling and implementation, as introduced in Sec 2.3. Secondly, in assessing the relative sampling effectiveness of two methods, such as k-ART and ABC, one should ensure that equivalent transition state pathways are being examined, that is, the pathways which play the same dominant role in giving rise to a particular system-level behavior of interest. In doing so, the effects of the cut-off radius in topology discretization and the use of the Mean Rate Method [56] on the connectivity of the sampled trajectories could be an issue in k-ART because of the high defect concentrations and the associated long-range interactions between defect clusters (illustrated in Figure 3.5). This step of benchmarking is important for gaining insights into the physical basis of each method, the understanding needed by the community in developing more robust methods for linking specific transitions to macroscale behavior.



In sum, the development of atomistic methods capable of following microstructural evolution over time scales beyond the reach of traditional molecular dynamics simulations is a continuing challenge, with good progress demonstrated here.

### **3.3 Anisotropic Diffusion of Vacancies and Self Interstitial Atoms in HCP Zr**

#### **3.3.1 Vacancy Diffusion**

##### **3.3.1.1 Background and Motivation**

Hcp Zr is an anisotropic material, and there are multiple inequivalent transition pathways for the point defects to migrate. For example, there are two migration paths for vacancy diffusion, one on the basal plane and one out of the basal plane. The in-plane migration has a lower barrier than the out-plane hopping, and both migration paths have 6 degenerate directions. Interstitial migration has many more pathways in the hcp Zr compared to the vacancy migration. In order to capture all possible migration mechanisms and their energy barriers, ABC-E algorithm therefore had to be developed (Chapter 2) and employed for this problem, because the original ABC method can only provide the lowest-barrier mechanism and would inaccurately estimate the diffusion kinetics of point defects in Zr. This is a general challenge for ABC when applied to complex systems with multiple competing transition paths as discussed in Chapter 2.

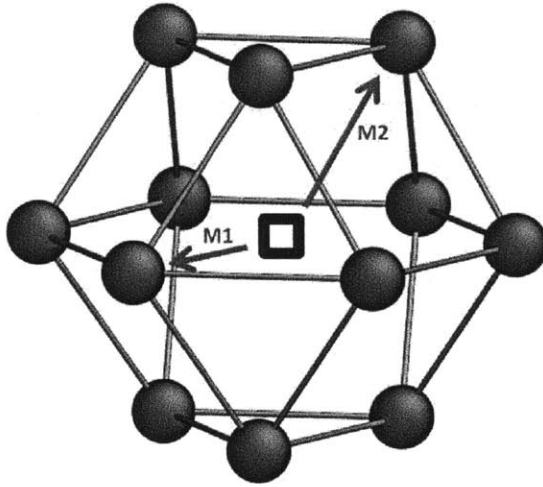


Figure 3.8 Two vacancy migration paths in Zr, represented by M1 and M2. These paths are captured by the ABC-E algorithm.

### 3.3.1.2 Problem Statement and System Set Up

In this section, we are aiming to identify both of the two migration paths in Zr, shown as M1 and M2 in Figure 3.8, by employing ABC-E method. We used the MA07 potential [110] and a system containing 2687 atoms.

### 3.3.1.3 Results and Discussion

We observed that the in-plane migration (M1) has a lower barrier 0.68 eV, compared to the barrier for out-plane migration (M2) is 0.76 eV. We then input these two barriers and the hcp geometry to a KMC algorithm. In the KMC simulation, we trace the coordinate of the vacancy as a function of number and direction of hops. Following Arrhenius law, the vacancy migration rates in-plane and out-of-plane can be expressed as  $k^a = k_0^a \exp[-\frac{E_{M1}}{k_B T}]$ , and  $k^c = k_0^c \exp[-\frac{E_{M2}}{k_B T}]$ , respectively. With the assumption that both migration paths have the same pre-exponential factor, i.e.  $k_0^a = k_0^c$ , we then calculate the mean square displacement (MSD) of the vacancy,

including the total MSD,  $\langle a \rangle$  MSD (in-plane) and  $\langle c \rangle$  (out-of-plane) MSD. Figure 3.9 (a) shows a typical MSD plot at 1000 K. It can be seen from the figure that, the slope of  $\langle a \rangle$  MSD is steeper than that of  $\langle c \rangle$  MSD, which indicates an anisotropically favored diffusion kinetics on the basal plane compared to out-of-plane. We further calculated the MSD at different temperatures, and derived the ratio between the c-axis and a-axis diffusivities, as shown in Figure 3.9 (b). The result indicates a significant anisotropy in diffusion at lower temperatures. The monotonic increase of this ratio with temperature, as expected, shows the decreasing extent of diffusion anisotropy at higher temperatures.

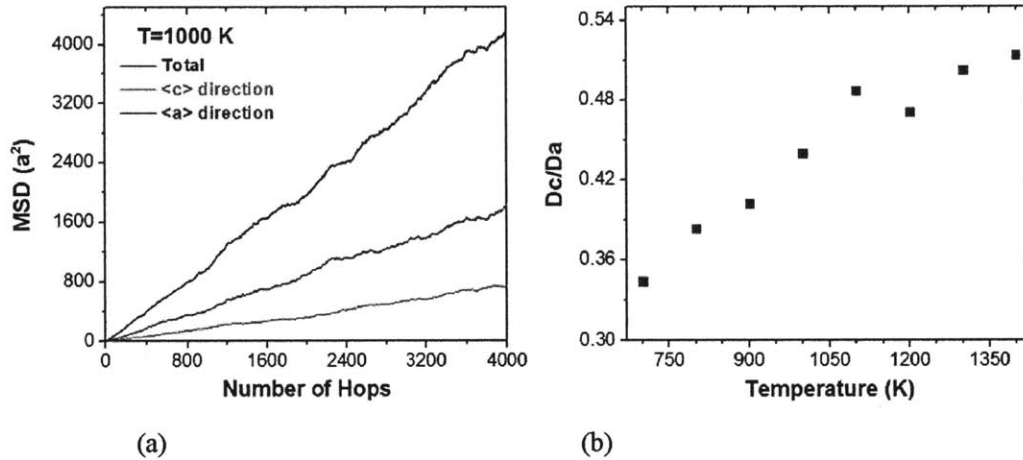


Figure 3.9 (a) The total MSD and its projection on  $\langle a \rangle$  and  $\langle c \rangle$  directions, at 1000 K. The slopes represent the diffusivities along different directions. (b) The ratio between the  $\langle c \rangle$  and  $\langle a \rangle$  diffusivities at various temperatures. All the results in (a) and (b) are based on the assumption that the pre-factors of two migrations are the same.

This result is qualitatively consistent with Osetsky et al.'s previous work [111] which used the AWB95 potential that is different from the one used here. On the other hand, we notice quantitative differences between the results reported here and in Ref [111]. In Ref [111] the ratio between c-axis and a-axis diffusivities is very close to 1 at temperature higher than 1000 K. However, our results in Figure 3.9 (b) give a much lower value,  $\sim 0.5$ .

We notice that in Ref [111], the pre-factors for  $\langle a \rangle$  and  $\langle c \rangle$  diffusions are different according to the MD data fitting (the M2 hopping pre-factor is about 30%

larger than that of M1 hopping). We then incorporate this effect into our KMC simulations. In other words, we set different values to the pre-factors following Ref [111], and re-calculate the ratio between  $\langle a \rangle$  and  $\langle c \rangle$  diffusions. As shown in Figure 3.10 (red squares), the  $D_c/D_a$  value becomes considerably larger. We also calculate the  $D_c/D_a$  with AWB95 potential [112], as shown by the purple open squares in Figure 3.10, and the result is consistent with Ref [111]. The discrepancy between red squares and purple open squares is due to the different interatomic potentials employed in the simulations. In Ref [111], AWB95 potential has been employed, while in our study the MA07 is employed. In AWB95 potential, the migration barriers for M1 and M2 are 0.84 eV and 0.89 eV, respectively. While in our calculation, the corresponding barriers with MA07 potential are 0.68 eV and 0.76 eV, respectively. The difference in MA07 potential is larger than in AWB95 potential, and thus indicates a stronger anisotropic diffusivity, i.e. a smaller value of  $D_c/D_a$ .

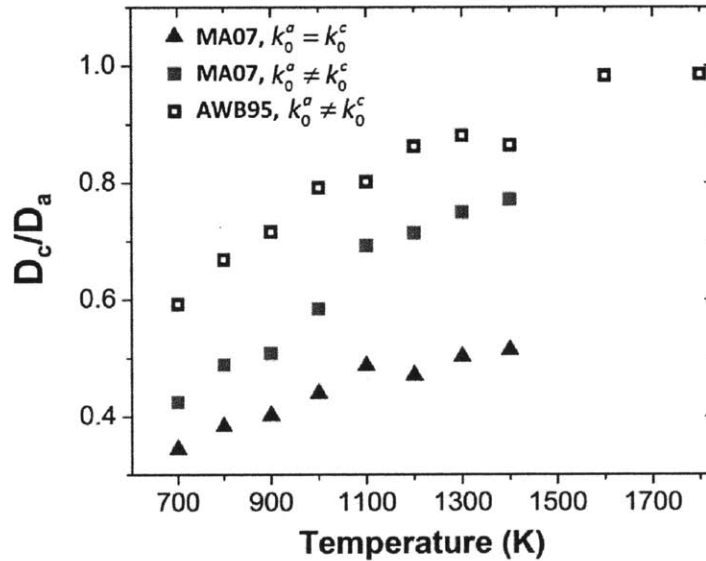


Figure 3.10 Blue triangles: the results with MA07 potential, and the same pre-factors. Red squares: the results with MA07 potential, and different pre-factors. Purple open squares: the results with AWB95 potential, and different pre-factors.

Very recently, Ishii et al. employed another long time scale method, adaptive-boost (AB) MD [42], to study the vacancy diffusion in Zr with MA07 potential. It

can be seen in Figure 3.11 that, the in-plane diffusion is faster than out-plane diffusion, and the derived migration barriers are also consistent with our calculations using the ABC-E method.

The benchmarks against different methods demonstrate that ABC-E method is able to identify multiple transition pathways quantitatively, and can hence provides a more accurate description of point defect diffusion in anisotropic materials compared to the traditional ABC algorithm.

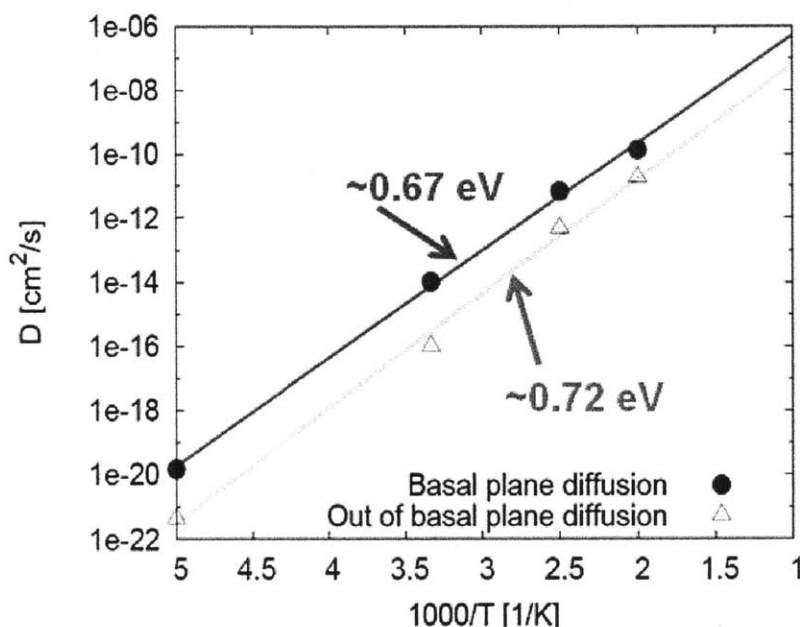


Figure 3.11 Diffusivity under different temperatures, by AB MD method, and with the MA07 potential.

### 3.3.2 Self-interstitial Atom (SIA) Diffusion

#### 3.3.2.1 Problem Statement and System Set Up

Figure 3.12 shows the possible interstitial sites in hcp materials, including octahedral (O), basal octahedral (BO), tetrahedral (T), basal tetrahedral (BT), crowdion (C), and basal crowdion (BC), respectively.

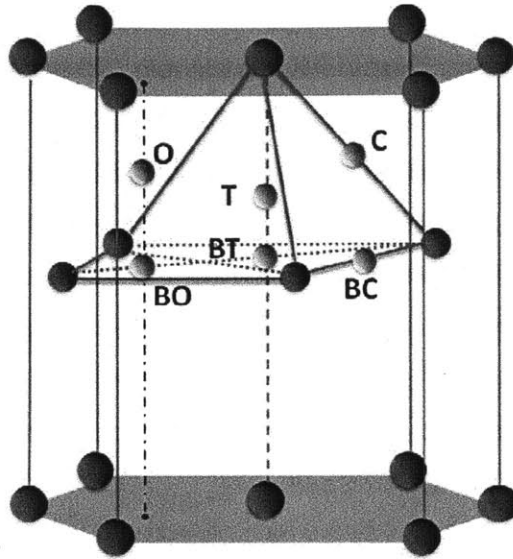


Figure 3.12 Possible interstitial sites in hcp metals (shown by green spheres).

To check the stabilities and formation energies for these interstitial sites, we insert an extra atom to the interstitial sites and then relax the system by the steepest descent algorithm, with the MA07 potential. There are 2689 atoms in the simulation cell, and periodic boundary conditions are applied for all directions. It can be seen in Figure 3.13 that, among the six interstitial sites, there are only three stable structures. Both the perfect O and C sites decay to a distorted O site with the degeneracy of 6. Both T and BT sites are unstable and decay to BC site. BO site is energetically stable.

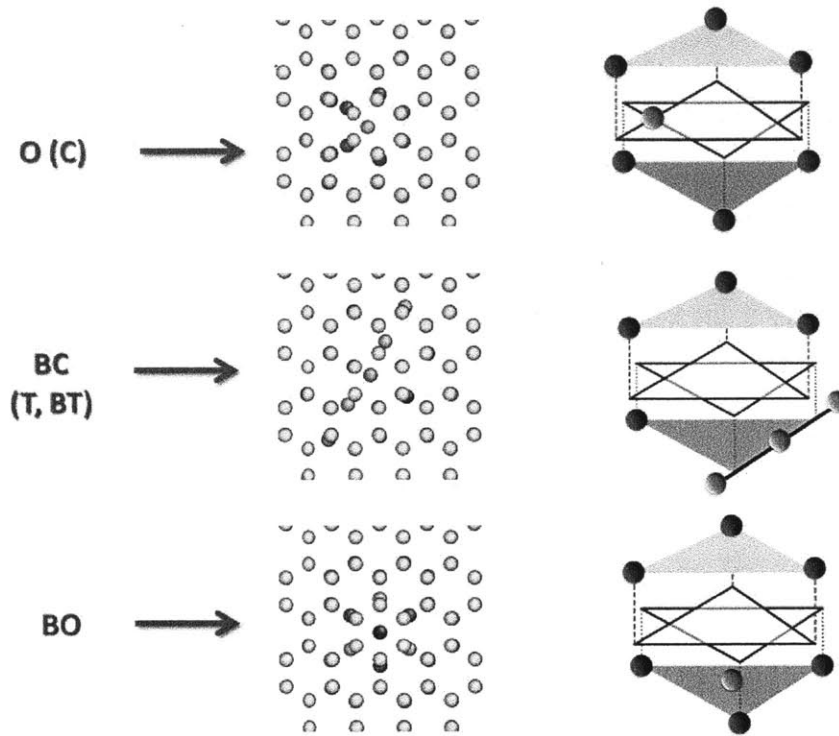


Figure 3.13 Only three stable among all six possible interstitial sites are stable, within MA07 interatomic potential.

The energetics for these sites are summarized in Table 3.2 below. The distorted O site is most stable, with the formation energy 2.74 eV. The formation energies for BC and BO sites are 2.83 eV and 2.86 eV, respectively. Although O site is observed most stable, which is consistent with previous work [110, 113], the quantitative results deviate from each other. The reason leads to the discrepancies are still unclear, and might be related to the size of simulation cell [113].

Table 3.2 The energetic of SIA states and the comparison against previous calculations.

<i>SIA State</i>	<i>Current Study</i>	<i>Mendelev et al [110]</i>	<i>Khater et al [113]</i>
<b>O</b>	2.74 eV	2.88 eV	2.78 eV
<b>BO</b>	2.86 eV	2.90 eV	N/A
<b>BC</b>	2.83 eV	2.91 eV	N/A

### 3.3.2.2 Results and Discussion

#### (i) SIA Migration Mechanisms in Zr

With ABC-E method, we are able to observe the migration mechanisms of SIA in hcpZr. The migration of SIA can be classified as two mechanisms, the O mechanism and BC mechanism, respectively.

##### (i) O mechanism

Starting from the O state (as shown in Figure 3.13), we observe there are mainly three migration pathways.

(a) Direct O-O hopping. As shown in Figure 3.14 below, the O state can directly migrate to the 1st and 2nd nearest neighbor O states, with the migration barriers 0.028 eV and 0.062 eV, respectively.

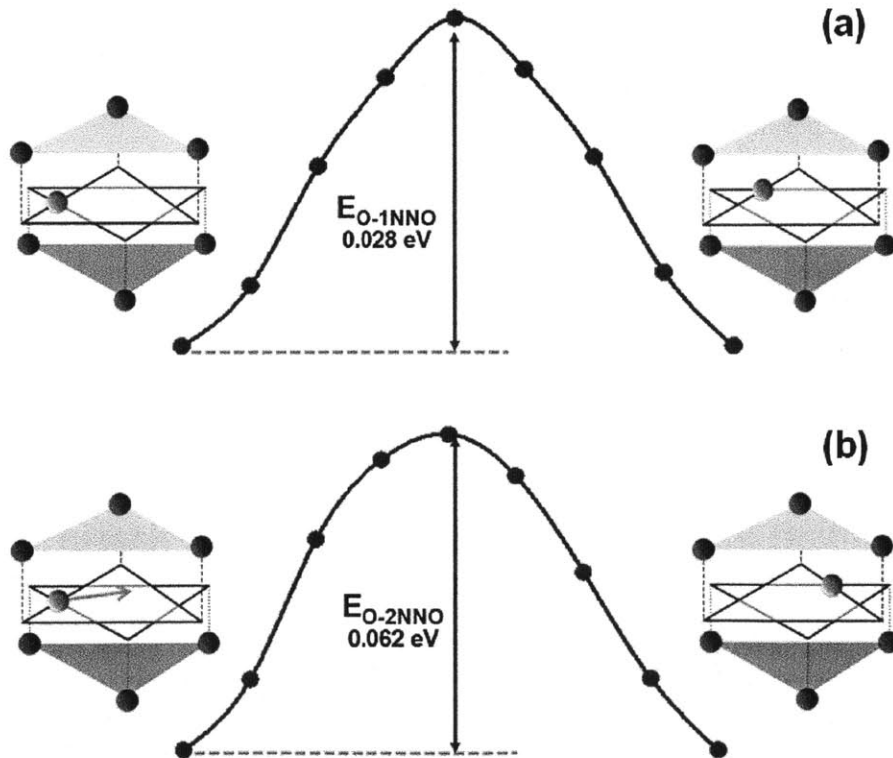


Figure 3.14 Direct O-O hopping mechanism. O state can migrate to either 1st NN O state or 2nd NN O state, as shown in (a) and (b), respectively.



(b) O-M1-BC migration. As shown in Figure 3.15 below, the extra atom in O state can first move away from the middle plane, and evolves to M1 state, where the extra atom stays a little bit above the basal plane. Then the extra atom further moves downward to the basal plane, and forms the BC state. Although Figure 3.15 shows only one pathway of O-M1-BC, the O-M1 transition has actually two degeneracies, i.e. the extra atom can either move upward or downward, and eventually leads to two BC states at different basal planes. The associated migration barriers are also marked in the figure. It can be seen that M1 is quite unstable due to the small transition barriers to either O or BC state.

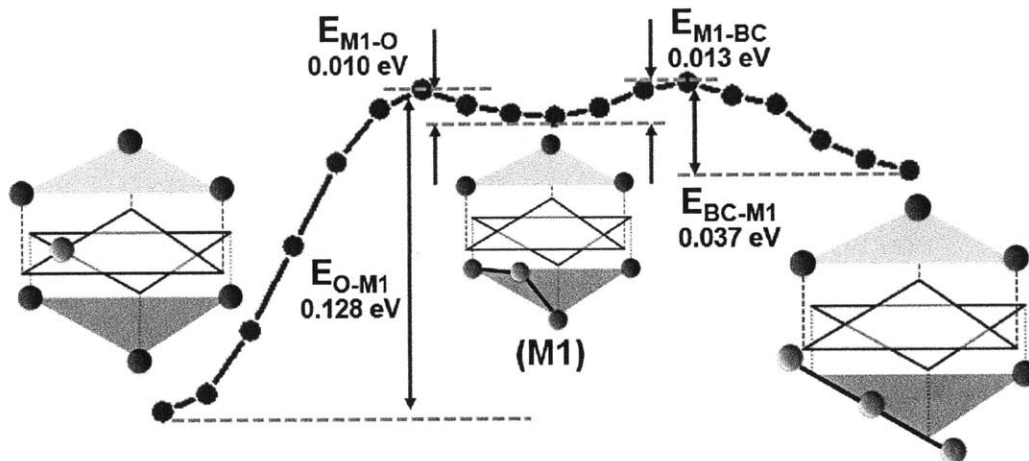


Figure 3.15 O-M1-BC migration pathway and associated barriers. Notice that O-M1 transition has actually two degeneracies, while the figure above only shows one of them.

(c) O-M2-O migration. As shown in Figure 3.16 below, the extra atom in O state can first move away from the middle plane, and forms a dumbbell with the nearest atom in the basal plane (M2 state). Then the nearest atom can be further pushed to an O state in another unit cell. Similarly, there are two degeneracies for O-M2 transition since there are two nearest neighbor atoms associated with the extra atom. The corresponding migration barriers are also marked in the figure. M2 is also an unstable state due to the very low unfaulting barrier.

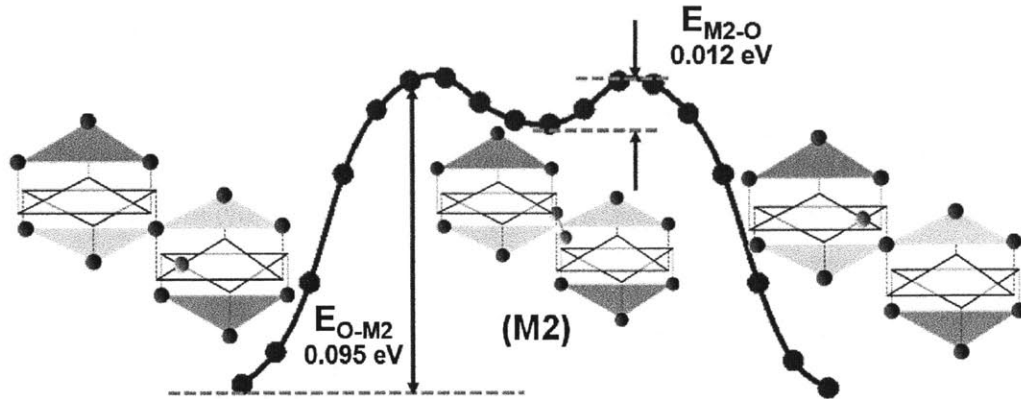


Figure 3.16 O-M2-O migration pathway and associated barriers. O-M2 transition has actually two degeneracies, while the figure above only shows one of them.

(ii) BC mechanism

Start from the BC state (as shown in Figure 3.13), we observe there are three migration pathways.

(a) BC-BC glide motion. Since BC is in crowdion structure, it can easily glide with the migration barrier 0.013 eV. The glide motion has two degeneracies.

(b) BC-M1-O migration. The mechanism is just the reverse pathway of O-M1-BC. The configurations and barriers have been demonstrated above in Figure 3.15. Notice that the BC-M1 transition has two degeneracies, since the middle atom in the crowdion can either move upward or downward.

(b) BC-BO-BC migration. As shown in Figure 3.17 below, the middle atom in the crowdion can migrate to the BO site in the basal plane. The BO site is not stable since the unfaulting barrier is only 0.011 eV. Then the BO state can migrate to BC state again, with three degeneracies. The corresponding migration barriers are also marked in the figure.

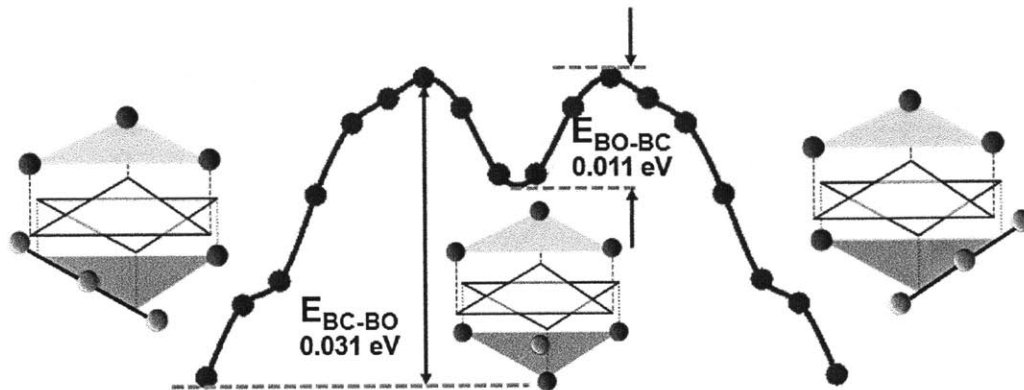


Figure 3.17 BC-BO-BC migration pathway and associated barriers. BO-BC transition has three degeneracies, while the figure above only shows one of them.

All the observed SIA migration mechanisms can be summarized by Table 3.3. We compare the results to Subramanian et al.'s recent calculation by a different technique, the temperature-accelerated dynamics (TAD) [43], as shown in Figure 3.18. It can be seen that more of the mechanisms from both sides are consistent with each other, and the quantitative differences are in the range of error tolerance.

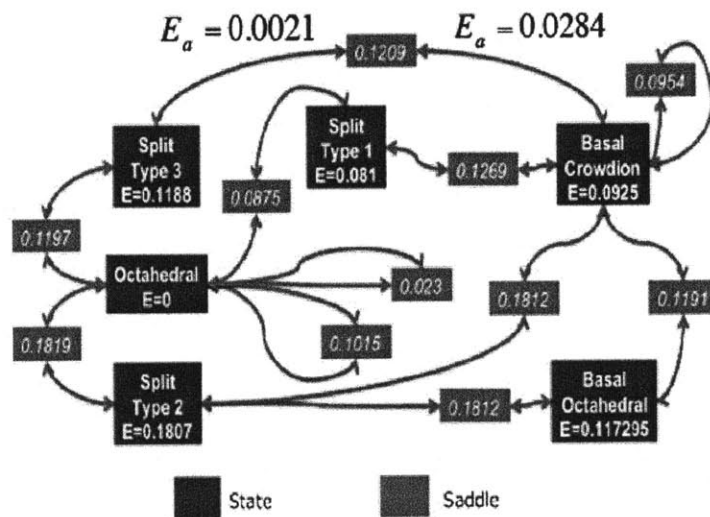


Figure 3.18 The summary on SIA migration mechanisms in Zr from Gopinath et al's TAD results [114].

Table 3.3 The summary on SIA migration mechanisms in Zr from ABC-E results.

<b>Migration Mechanism</b>		<b>Governing Barrier</b>
<b>O Site</b>	O-O (1NN)	0.028 eV
	O-O (2NN)	0.062 eV
	O-M2-O	0.095 eV
	O-M1-BC	0.131 eV
<b>BC Site</b>	BC-BC (glide)	0.013 eV
	BC-BO-BC	0.031 eV
	BC-M1-O	0.037 eV
<b>BO Site</b>	BO-BC	0.011 eV

In sum, the SIA diffusion can be summarized as following: the O state prefers to hop among the six degenerated sites in the same plane due to the lowest migration barrier. The O state has also some probability to migrate to the O site in another plane via O-M2-O mechanism, and thus follows a 3D migration. In addition, the O state also has a chance to evolve to BC state via O-M1-BC mechanism. Once the system migrates to BC state, the SIA will be mainly governed by the 1D glide motion in the basal plane due to the smallest barrier. The BC state has also a probability to transform to another BC state along other direction in the same basal plane, via BC-BO-BC mechanism. The BC state can jump back to the O state via BC-M1-O mechanism. Basically, the SIA diffusion is governed by a mix of 1D and 3D migration mechanisms. The O-M2-O mechanism provides a 3D motion, while BC glide provides a 1D motion in the basal plane. The fraction of the 1D (3D) motion can change as a function of temperature.

## (ii) Anisotropic Diffusion Kinetics

With all derived mechanisms and associated barriers in Sec 3.4.2 (i), we then employ the KMC simulation to study the SIA diffusion in hcp Zr. According to transition state theory, the transition rate can be expressed as  $k^i = k_0^i \exp[-\frac{E_i}{k_B T}]$ ,

where  $E_i$  and  $k_0^i$  are the reaction barrier and pre-exponential factor, respectively. In our KMC simulations, all the transitions are assumed to have the same pre-exponential factor, i.e.  $k_0^i = k_0 = 10^{13} s^{-1}$ .

### (1) SIA diffusion trajectories

Starting from the origin point, the positions of the extra atom are traced as a function of time. Figure 3.19 (a) shows two SIA diffusion trajectories up to 100 ps, at the temperature of 300 K and 500 K, respectively.

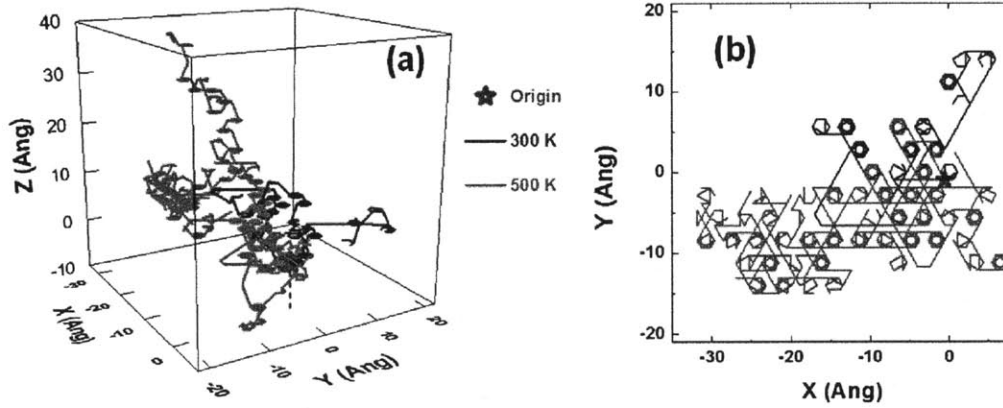


Figure 3.19 (a) SIA diffusion trajectories up to 100 ps, at 300 K and 500 K, respectively. (b) The projections of trajectories in basal plane.

It can be seen from Figure 3.19 (a) that, the trajectories consist of many “nodes”, which are connected by line segments. From the projections on the basal plane (Figure 3.19 (b)), it can be seen that the “nodes” are actually hexagons, which represent the direct O-O hopping mechanism. The short line segments are the O-M2-O migrations, while the long segments are the 1D motion via BC-BC glide mechanism.

## (2) Mean square displacement (MSD) of SIA diffusion

We then calculate the mean square displacement (MSD) of the extra atom (Notice that the extra atom is not necessarily the initial interstitial atom, because the O-M2-O mechanism will actually change the extra atom). In other words, we are actually calculating the MSD of the mass transport.

We calculate the MSD at different temperature, from 150 K up to 900 K. The statistics has been demonstrated extremely important in calculating the diffusivities [115]. In this work, to increase the statistics, we employ an extensive study. Under each temperature, 1000 KMC simulations are employed. In each KMC simulation, we collect the MSD data until 10 ns.

Figures 3.20 (a-c) show the average MSD plots over 1000 KMC simulations, at 150 K, 600 K, and 900 K, respectively. It can be seen from the figure that, the slope of  $\langle a \rangle$  MSD is slightly steeper than that of  $\langle c \rangle$  MSD, which indicates an anisotropic diffusion. We further calculated the ratio between the c-axis and a-axis diffusivities, as shown in Figure 3.20 (d). It can be seen that the ratios are all above 0.8 for entire simulated temperature range, which indicate the anisotropic effect is very weak. On the other hand, the plot in Figure 3.20 (d) shows a very interesting non-monotonic behavior that, at low temperature, the diffusion is more isotropic. At intermediate temperatures, the anisotropic effect increases as a function of temperature, which is in contrast to the results calculated by AWB95 potential [111]. When the temperature is higher than 600 K, the anisotropic effect starts to decrease as a function of temperature.

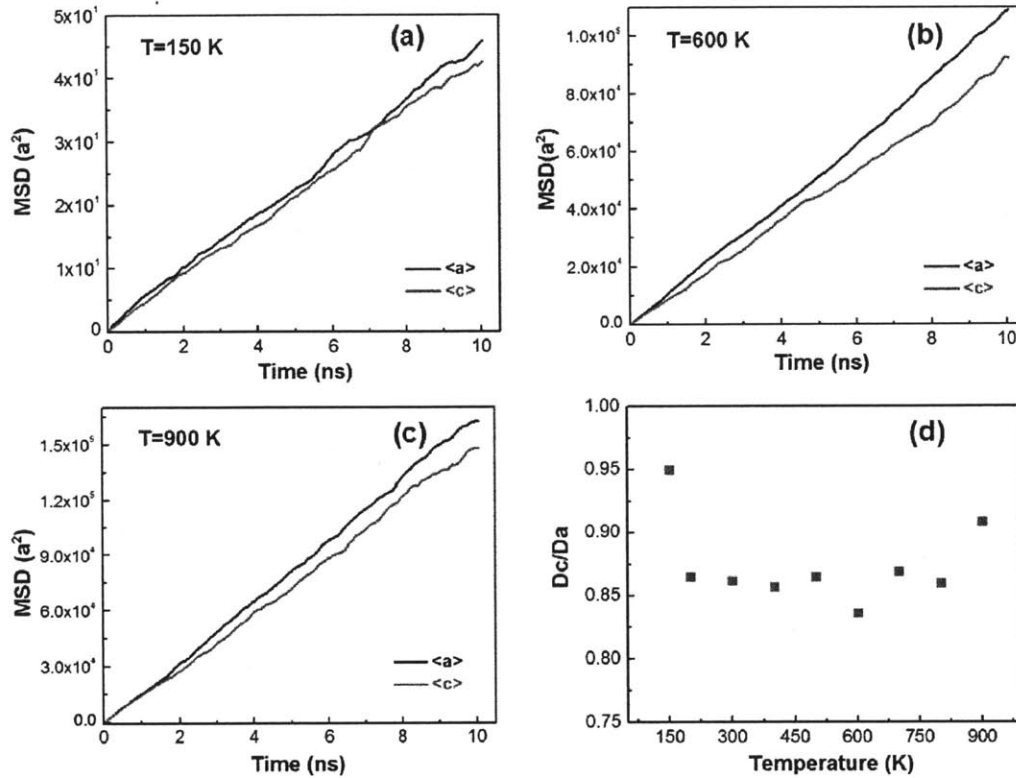


Figure 3.20 (a-c) The MSD on <a> and <c> directions, at 150 K, 600 K, and 900 K, respectively. (d) The ratio between the <c> and <a> diffusivities at various temperatures.

This novel behavior is related to the MA07 potential applied in the simulation. As shown in Table.3.2, the O state has the lower formation energy than BC state for about 0.1 eV. On the other hand, the O-M2-O mechanism has a lower migration barrier than O-M1-BC mechanism for about 0.035 eV. Therefore at low temperature, the system mostly stays at O state, and the diffusion is governed by O-M2-O mechanism, which displays a 3D diffusion. As the temperature increases, the system has a higher probability to stay at the BC state. For the BC mechanism, as discussed above, the BC-BC glide has a lower barrier than BC-M1-O migration. Therefore, the 1D motion, i.e. the anisotropic effect, starts to increase. At high enough temperature, the differences between all the transitions are washed out, and the diffusion should approach to an isotropic pattern.

The non-monotonic behavior shown in Figure 3.20 (d) is in contrast to previous study [111], and the interatomic potential is a critical factor leads to the discrepancy. In previous study, the AWB95 potential is applied. In AWB95 potential, the BC state has the lowest formation energy [113]. Therefore the system has the highest probability to stay at BC state, and thus displays a 1D diffusion mechanism at low temperature [111]. In addition, the 1D diffusion will monotonically transitions to a 3D diffusion at high temperature. In this study however, with MA07 potential, the O state has the lowest formation energy. But the dominant O mechanism is 3D as discussed in Sec 3.3.2.2 (i). Therefore the system shows a 3D diffusion at low temperature. When the temperature increases, the system has higher probability staying at BC state, and therefore the fraction of 1D diffusion starts to increase. At high temperatures, all transitions are effectively activated and the system shows a 3D diffusion again.



## **Chapter 4**

# **Line Defects: Dislocation Mobility, and Interaction with Point Defects**

This chapter focuses on predicting the mobility of dislocations and their interaction with irradiation induced point defects from very low to very high strain rates. This new capability is important because dislocations crucially determine the mechanical properties that are critical for the safety of structural materials in the nuclear reactor. We first provide a physically based, parameter-free model to explain how the flow stresses of dislocations in metals vary at different temperatures and applied strain rates. In addition, we consider two examples involving the dislocation-obstacle interactions over a wide range of temperature and strain rate conditions. We observe that the interaction mechanisms can be different at various environments, and correspondingly lead to different mechanical responses. All the examples demonstrated in this chapter reflect a common mechanism behind all these simulated processes – the competition between strain rate and thermal activation.

## **4.1 Dislocation Mobility at Prescribed Strain Rates and Temperatures**

### **4.1.1 Background and Motivation**

At low temperature, the deformation of metals is largely governed by the thermal activation of dislocation glide [35]. Experiments on different structures of metals, including Fe, Ta, Cu, Al, and Zn [32-37], indicate the dislocation flow stress

varies with strain rate in an apparently universal manner. The flow stress increases slowly in an Arrhenius manner at low strain rates but turns upward sharply beyond a certain range of strain rate. Although the results for different metals can be quantitatively different, the flow stress “up-turn” behavior when the strain rate reaches the range of  $10^3$ - $10^4$ s<sup>-1</sup>[37, 38] appears to have a more fundamental origin. The onset of non-Arrhenius response has elicited the development of several empirical constitutive models [35, 38, 116-122], including the assumption of phonon drag effects to account for the data at high strain rates. All existing models to date use adjustable parameters to connect the flow stress below and above the critical strain rate for “up-turn”. Therefore here we are seeking a fundamental theory without any presumed mechanisms or fitting parameters.

#### **4.1.2 Problem Statement**

In this case study, we derive a general formalism to describe the flow stress - strain rate relation by focusing on the transition time for an activated event that is both thermally and stress driven. We show that the temperature dependence of the transition time is significantly non-Arrhenius at high strain rates. When applied to predict the dislocation flow stress in single crystals, this non-Arrhenius behavior leads naturally to the experimentally observed stress up-turn at high strain rate, without invoking a different physical mechanisms, or introducing any bridging parameters.

#### **4.1.3 Results and Discussion**

##### **(i) Coupling Effect between Thermal Activation and Applied Strain Rate**

The derivation of the flow stress dependence on the strain rate is described in this section. In the thermal activation regime, a dislocation is located on the bottom of its potential energy valley until a thermal fluctuation enables it to climb over the

activation barrier to glide to the next valley. In general, the activation free energy for dislocation flow is a function of both temperature and stress, represented as  $Q(\sigma, T) = (1 - T/T_m)E(\sigma)$  [28], with  $T_m$  being the melting temperature and  $E(\sigma)$  the glide activation energy at 0 K. Since we will be concerned only with the low temperature regime (less than  $0.15T_m$ ), we can take  $Q(\sigma, T) \approx E(\sigma)$ . The activation energy is known to decrease with applied stress [28, 123-126]. When a strain rate is applied, the system begins to deform as time evolves, thus the state of stress becomes time-dependent as does  $E(\sigma)$ . With this in mind and following the transition state theory (TST) [83], we will write for the escape rate of a dislocation from the potential energy valley at a certain stress state as

$$k(\sigma) = k_0 e^{-\frac{E(\sigma)}{k_B T}}, \quad (\text{Eq.4.1})$$

where  $k_0$  is the attempt frequency. The activation barrier  $E(\sigma)$  is yet to be specified. In the elastic deformation regime, the dependence of stress on applied strain rate as a function of time,  $t$ , is given by:

$$\sigma = G\varepsilon = G\dot{\varepsilon}t, \quad (\text{Eq.4.2})$$

where  $G$  is the shear modulus. The  $\varepsilon$  in Eq.(4.2) represents the elastic strain, because in this case study we focus on the initiation of dislocation flow, which pertains to the transition from elastic deformation regime to plastic deformation regime. In light of Eq.(4.2),  $k(\sigma)$  can be represented as a function of time,  $k(t)$ .

The residence probability  $P(t)$  that the dislocation does not escape to a neighboring potential energy valley during time  $t$  (i.e. the system remains in the elastic deformation regime) is defined as [28]:

$$\frac{dP(t)}{dt} = -k(t)P(t), \quad (\text{Eq.4.3})$$

or

$$P(t) = \frac{1}{C} \exp\left[-\int_0^t k(t') dt'\right], \quad (\text{Eq.4.4})$$

where  $C$  is the normalization factor. Accordingly, the first-escape probability distribution  $p(t)$  is given by,

$$p(t) = -\frac{dP(t)}{dt} = \frac{1}{C} k(t) \exp\left[-\int_0^t k(t') dt'\right]. \quad (\text{Eq.4.5})$$

with normalization,

$$\int_0^{t_c} p(t) dt = 1 \Rightarrow C = \int_0^{t_c} k(t) \exp\left[-\int_0^t k(t') dt'\right] dt, \quad (\text{Eq.4.6})$$

where  $t_c = \frac{\sigma_c}{G\dot{\epsilon}}$  represents the maximum residence time, at a given non-zero strain rate  $\dot{\epsilon}$ . The average residence time is therefore given by,

$$\bar{t} = \int_0^{t_c} tp(t) dt = \frac{\int_0^{t_c} tk(t) \exp\left[-\int_0^t k(t') dt'\right] dt}{\int_0^{t_c} k(t) \exp\left[-\int_0^t k(t') dt'\right] dt}. \quad (\text{Eq.4.7})$$

In the limit of vanishing  $\dot{\epsilon}$ ,  $k(t)$  is a constant,  $k$ , and  $t_c \rightarrow \infty$ , Eq.(4.7) gives the average time as  $\bar{t} = 1/k$ , which follows the Arrhenius law. However, for the general condition of non-zero strain rate, the result of Eq. (4.7) will deviate from the Arrhenius behavior.

We would like to stress here that, the derivations of Eq.(4.1-4.7) represent a general formalism that is applicable to a wide range of systems where the reaction rate is time-dependant. Examples include dislocation nucleation under constant strain rate loading, glass transition at different cooling rates, as well as dislocation flow. In this case study we are particularly interested in predicting the variation of flow stress with temperature and strain rate. Since the dislocation will start to glide beyond the residence time  $\bar{t}$ , we obtain the flow stress by combining Eq.(4.2) and Eq.(4.7),

$$\bar{\sigma}_{flow} = G\dot{\epsilon}\bar{t} = \frac{\int_0^{\sigma_c} \sigma k(\sigma) \exp\left[-\frac{1}{G\dot{\epsilon}} \int_0^{\sigma} k(\sigma') d\sigma'\right] d\sigma}{\int_0^{\sigma_c} k(\sigma) \exp\left[-\frac{1}{G\dot{\epsilon}} \int_0^{\sigma} k(\sigma') d\sigma'\right] d\sigma}. \quad (\text{Eq.4.8})$$

In summary, once the dislocation migration barrier profile  $E(\sigma)$  is obtained, the flow stress of the corresponding slip system can be calculated according to Eq.(4.8). There is then only one parameter in Eq.(4.8), the attempt frequency  $k_0$ , which we

take to be on the order of  $10^{12-13} \text{s}^{-1}$ . Although Eq.(4.8) is developed to give the flow stress of a slip system, the formalism is applicable in general to any activated process described by Eq.(4.1).

## **(ii) System Set Up**

The deformation of bcc metals at low temperature is known to be controlled by the motion of  $\frac{1}{2}\langle 111 \rangle$  screw dislocations[126], the flow mechanism being 3D kink nucleation and propagation [124, 125, 127]. For the purpose of testing Eq.(4.8), we examine a short dislocation of length  $5b$ ,  $b$  being the Burger's vector, which should glide without kink nucleation. We use a simulation cell of 55440 atoms, with the dimensions perpendicular to the dislocation line approximately  $230\text{\AA} \times 230\text{\AA}$ . Periodic boundary conditions are applied on the dislocation line and glide directions. The 2D glide motion in this case is frequently studied to infer the behavior in 3D[127]. The embedded-atom method-type potential developed by Mendeleev et. al.[128] is employed. To benchmark the results obtained using Eq. (4.8), we performed direct molecular dynamics (MD) simulations on the same system at the high strain rates where MD is known to be valid. The strain rate conditions,  $10^7$  and  $10^6 \text{ s}^{-1}$ , correspond to steady state dislocation velocities of 22 and 2.2 m/s respectively. The simulations show at low  $T < 100\text{K}$  the dislocation moved practically in the same  $\{110\}$  plane, while at higher  $T$  frequent cross-slips were observed and the overall motion was a combination of slips in the  $\{110\}$  and  $\{112\}$  planes.

## **(iii) Response of Dislocation Mobility to Applied Strain Rate**

The strain-stress curve for our screw dislocation under static conditions is first shown in Figure 4.1 (a). Plastic deformation is seen to set in at around 1400 MPa, consistent with the known Peierls stress values [129]. We then determine the glide barriers for the particular model under study using atomistic simulations capable of probing different stress conditions. The NEB is one way to map out the glide barrier since the initial and final states of the transition are known. In this case we use instead the ABC method to capture the value of activation barrier. At a given stress

state, the method induces the dislocation to migrate to the adjacent energy valley by a series of activation and relaxation steps. As seen in Fig.1 (b), the glide barrier shows a monotonic, though nonlinear, decrease as one may generally expect for a stress activated process. This is indeed what is known from a recent study of surface dislocation nucleation [28]. To fit the experimental data a commonly used expression is  $E(\sigma) = E_0 \left[ 1 - (\sigma / \sigma_c)^p \right]^q$ , where  $E_0$  is the activation barrier under zero stress,  $\sigma_c$  the Peierls stress, and (p,q) are the shape parameters [123-125]. For the stress variation determined here by atomistic simulation the fitting parameters have values of  $p = 0.63$ , and  $q = 1.41$ , which give a clearly nonlinear behavior for  $E(\sigma)$  as seen in Figure 4.1 (b). The dashed line in Figure 4.1 (b), on the other hand, denotes the fit with  $p=q=1$  which is the assumption of a constant activation volume with a linear behavior.

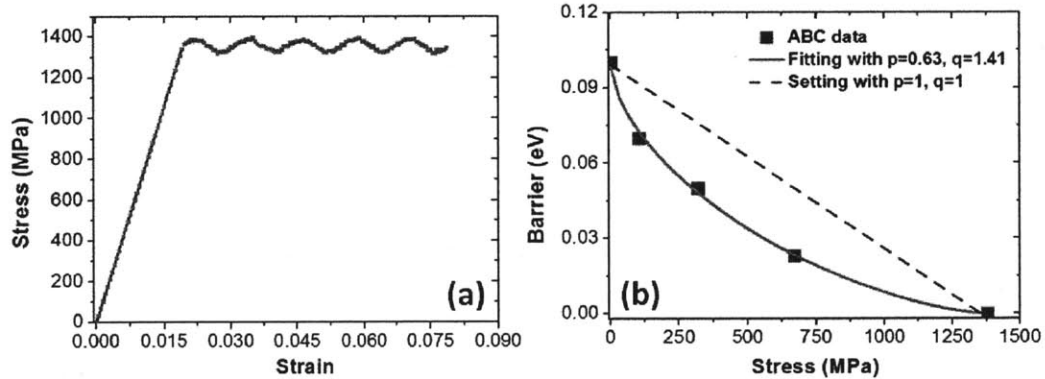
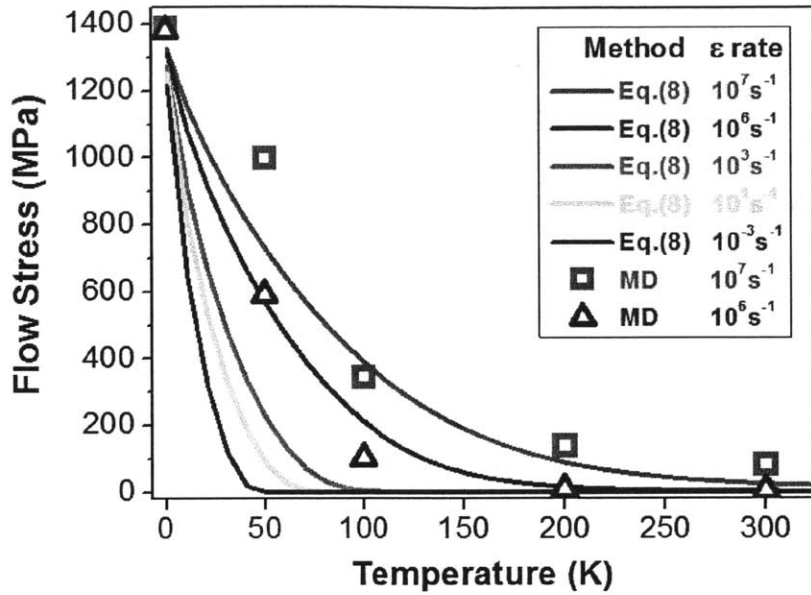


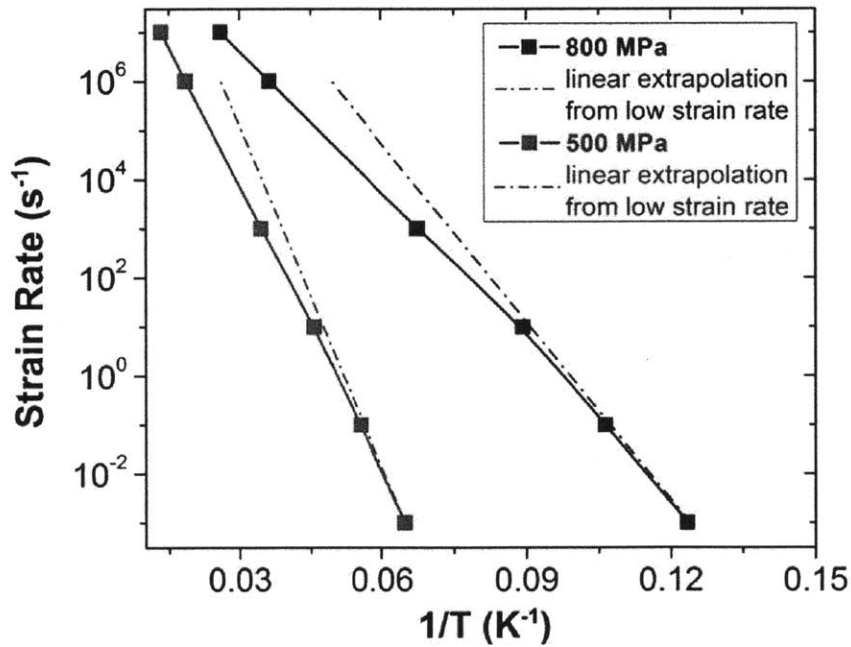
Figure 4.1 (a) Strain-stress curve of the  $\frac{1}{2}\langle 111 \rangle$  screw dislocation in bcc Fe under static conditions. The corresponding Peierls stress is about 1400 MPa. (b) Activation barrier for the glide motion of  $\frac{1}{2}\langle 111 \rangle$  screw dislocation as a function of stress. Blue squares represent the calculated data points by ABC method. The red line is a fit to  $E(\sigma) = E_0 \left[ 1 - (\sigma / \sigma_c)^p \right]^q$  with  $p=0.63$  and  $q=1.41$ . The dashed line represents a constant activation volume scenario with  $p=1$  and  $q=1$ .

The activation barrier  $E(\sigma)$  is the only input needed to predict through Eq.(4.8) the temperature and strain rate variations of the flow stress, both of which can be directly compared against experiments. Figure 4.2 shows the thermal behavior of

flow stress for strain rates varying over 10 orders of magnitude, from  $10^7\text{s}^{-1}$  down to  $10^{-3}\text{s}^{-1}$ . In the low temperature limit, absence of thermal activation, all flow stresses approach the Peierls stress. As temperature increases, all the flow stresses monotonically decrease and approach zero by room temperature. At a fixed temperature, higher strain rate loading results in higher flow stress response. Thus any attempt to compare experimental data against MD simulations must take into account the difference in the strain-rate.



(a)



(b)

Figure 4.2 (a) The flow stress of the  $\frac{1}{2}\langle 111 \rangle$  screw dislocation under different strain rate and temperature conditions. The solid lines show the results calculated according to Eq.(4.8) with the attempt frequency of  $1.2 \cdot 10^{12} \text{ s}^{-1}$ . The open squares and triangles represent direct MD simulation results at strain rates of  $10^7 \text{ s}^{-1}$  and  $10^6 \text{ s}^{-1}$ , respectively. (b) The relation between strain rate (in logarithmic scale) and  $1/T$  at constant flow stress of 800 MPa and 500 MPa. The dashed lines are linear extrapolation from the low strain rate regime.



The symbols in Figure 4.2 (a) represent the MD results at strain rate of  $10^6\text{s}^{-1}$  and  $10^7\text{s}^{-1}$ . They are in reasonable agreement with the predictions of Eq.(4.8) using  $k_0 = 1.2 \cdot 10^{12}\text{s}^{-1}$ , which matches the Debye frequency satisfactorily. This constitutes a self-consistent test of Eq.(4.8) with  $E(\sigma)$  taken from Figure 4.1 (b) in the range of strain rates where MD is valid. One can see an increasingly sharp drop of flow stress as the strain rate decreases to the range accessible to conventional experiments, The sharp drop has been known as a significant feature of the thermal activation process; this behavior is not well captured by MD simulations at its characteristic strain rates [28, 126]. Figure 4.2 (a) shows that this behavior is at least qualitatively accounted for by the present model.

To probe further the coupled effect of thermal and stress activation we plot strain rate and reciprocal temperature at constant flow stresses in Figure 4.2 (b), where a linear relation would indicate adherence to Arrhenius behavior. Non-Arrhenius behavior is seen to set in at high  $\dot{\epsilon}$ . Thus a lower effective barrier at high strain rates is indicated.

The variation of flow stress with strain rate is of fundamental interest in experimental studies of crystal plasticity. Figure 4.3 (a) shows the predicted behavior based on Figure 4.2 (a) and Eq.(4.8). Under the limit of infinitely high strain rate, the flow stress approaches the Peierls stress. On the other hand, the flow stress is negatively sensitive to the temperature. In the high temperature limit, the flow stress approaches zero regardless of the strain rate. At low  $\dot{\epsilon}$  the flow stress increases only moderately, but as  $\dot{\epsilon}$  increases, above  $100\text{ s}^{-1}$  at 50 K, and  $10^4\text{s}^{-1}$  at 100 K, it begins to increase much more strongly.

This up-turn behavior can be analyzed in terms of two factors, stress dependant activation volume, and strain rate induced non-Arrhenius behavior. Because of the non-linear stress dependence of the activation barrier (Figure 4.1 (b)), the activation volume is very small at high stresses. Such small activation volume leads to a high sensitivity of the flow stress dependence on strain rate [28]. In addition, as derived in Eq.(4.7), there is a non-Arrhenius behavior due to the strain rate loading which also contributes to the up-turn in Figure 4.3 (a). To decouple the two contributions, we

remove the non-linearity of  $E(\sigma)$  by setting  $p$  and  $q$  equal to unity (dashed line in Figure 4.1 (b)). Now the only non-linear factor comes from the strain rate induced non-Arrhenius behavior in Eq.(4.8). As shown in Figure 4.3, under this condition, the flow stress up-turn remains, but the stress is now higher beyond the crossover strain rate. Since the assumption of  $p=q=1$  results in a higher effective barrier and correspondingly a longer residence time, it follows that the flow stress response is higher as well. Our analysis therefore shows the onset of flow stress up-turn is to be attributed mainly to the non-Arrhenius behavior induced by strain rate, as described by Eq.(4.7) and Eq.(4.8). This result stands in contrast to the previous study of Domain et al. [126], which extrapolated the short time-scale simulations to long term behavior by assuming a linear relation between flow stress  $\sigma_{flow}$  and logarithm of strain rate,  $\ln \dot{\epsilon}$ .

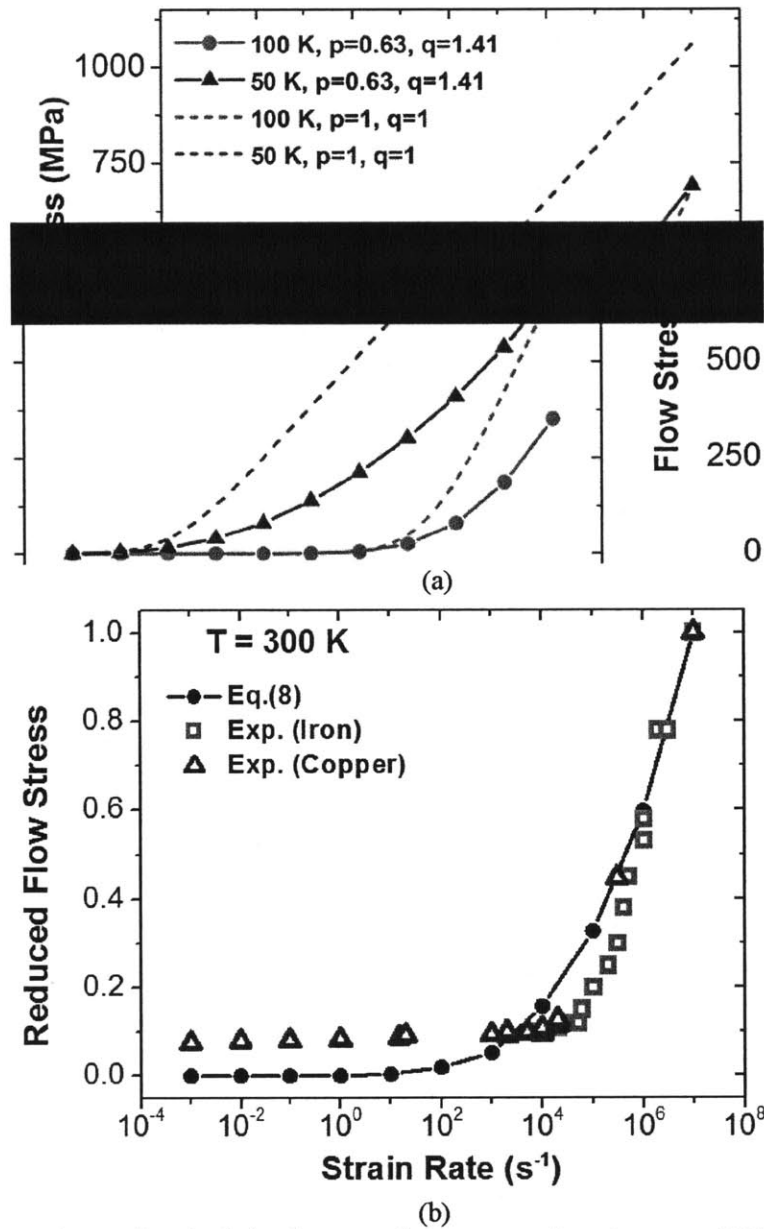


Figure 4.3 (a) The predicted relation between flow stress and strain rate at 50 K and 100 K. The solid symbols and lines are the calculated results for the  $\frac{1}{2}\langle 111 \rangle$  screw dislocation in bcc Fe with  $p=0.63$  and  $q=1.41$  in  $E(\sigma) = E_0 [1 - (\sigma / \sigma_c)^p]^q$ . The dashed lines are the results for a hypothetical scenario of  $p=1$  and  $q=1$  that corresponds to constant activation volume for the dislocation. (b) Variation of reduced flow stress with strain rate at 300 K. The experimental data on copper (blue triangles) and on iron (red squares) are adapted from [38] and references therein. The black line represents the results calculated by Eq.(4.8), with the activation energy profile input from Gordon et al.'s work in [127] for a long screw dislocation in bcc Fe.

To compare the predicted up-turn behavior quantitatively with experimental data, we adapt the energy profile  $E(\sigma)$  for a longer screw dislocation system in bcc Fe calculated by Gordon et al.[127] and use it as input into Eq.(4.8). Figure 4.3 (b) shows the variation of flow stress and strain rate at 300 K, as observed experimentally and predicted by our model. Since the magnitude of flow stress is significantly influenced by the defect microstructures in the experimental specimens[38], the quantitative comparison can only be meaningful after appropriate normalization, e.g. in a precedent display of the temperature variation of the viscosity of supercooled liquids [130]. Therefore, in Figure 4.3 (b) we show the reduced flow stress, defined as the ratio of flow stress to its value at the highest strain rate  $10^7\text{s}^{-1}$ , as a function of strain rate. It is seen that both the experiments and our calculation results show a significant flow stress up-turn with the critical strain rate in the range of  $10^4$ - $10^5\text{s}^{-1}$ . We regard the quantitative agreement with experiments to be a test of whether the mechanism of the transitional behavior is described correctly. The extent of the agreement suggests Eq.(4.8) plus  $E(\sigma)$  have essentially captured the mechanism for the flow stress up-turn behavior. On the other hand, it is known that the flow stress magnitude depends on the local defect microstructure in the material. Experimental specimens have a complex defect microstructure leading to appreciably higher flow stresses (due to, for example, dislocation-obstacle interactions) seen in the experiments compared to the results in Figure 4.3 (a). It is therefore intriguing that the reduced flow stress predicted by our model in Figure 4.3 (b) is also quantitatively consistent with experiments from different materials (a ductile one, copper, and a brittle one, iron). We attribute this finding to the fact that the energy barrier for dislocation to climb/glide over the defects/obstacles in the material bears a similar stress-activated behavior as the simple dislocation glide represented by the expression  $E(\sigma)=E_0\left[1-(\sigma/\sigma_c)^p\right]^q$  that was described above [121]. Thus, Figure 4.3 (b) demonstrates not only the accuracy of our model and the governing mechanism of flow stress up-turn, but also the general applicability of this

model regarding problems of coupled stress and thermal activated processes, beyond simple dislocation glide.

To summarize, in this case study we present a constitutive model which describes the variation of the plastic flow stress with temperature and strain rate. The model is given by Eq.(4.8) which involves the specification of  $E(\sigma)$ , the stress-dependent activation barrier for dislocation mobility. This is the key and the only input needed for the model to predict the temperature and strain-rate behavior shown in Figure 4.2 (a) and Figure 4.3, respectively, results that are tested against measurements. We show that the coupled effects of thermal and stress activation can be analyzed naturally in the framework of transition state theory (for activated state processes). With respect to the particular phenomenon of the flow-stress up-turn (Figure 4.3) we provide a parameter-free explanation of the transition from thermal- to stress- activation controlled regimes across a critical  $\dot{\epsilon}$  range that matches well with experiments, as an alternative to the interpolative models in the literature [35, 119, 121]. It would be of considerable interest to test whether this model can also help understand other problems, as we will discuss in Chap 5, for example, the yield strength up-turn behavior at high strain rates in glassy solids [131].

## **4.2 Dislocation-SIA Cluster Interaction Mechanisms Mapped by Atomistic Simulations as a function of Strain Rate in Zr**

### **4.2.1 Background and Motivation**

Interactions of defects with dislocations affect many of the mechanical properties of metals. This is especially important for irradiated materials where a host of non-equilibrium defect structures are produced. They serve as obstacles to moving dislocations, alter the mechanical properties and critically impact the safety and integrity of structural materials in the nuclear energy systems [24, 25, 44-47]. A mechanism map that delineates the dislocation-defect interactions as a function of environment conditions is thus desired in understanding and predicting materials deformation at meso-scale to optimize performance under a wide range of environments. It is known, as shown by the pioneering studies of Ashby et al. [132, 133], Zhu et al. [134], Yamakow et al. [135], that material deformation mechanisms are strongly affected by the stress and temperature conditions and by grain size. On the other hand, strain rate, another key environmental driver to material degradation, has not yet been systematically introduced to the realm of mechanism maps. The challenge in doing so is two-fold: firstly, many tensile experiments are operated under low strain rates conditions, i.e. slower than  $10^0\text{s}^{-1}$ [30, 136, 137]; but all the computational work using molecular dynamics (MD) to date aimed to reveal the interaction mechanisms between the dislocations and obstacles by performing the simulations only at one particular condition or over a very limited range of conditions. Typical MD simulations of these interactions are performed either at very high strain rates greater than  $10^6\text{s}^{-1}$ [7, 9, 10, 19-22], or at static conditions where the

temperature is set to be 0 K [23-26]. We note that the static calculations only relax the system based on the minimization of the potential energy, and thus, they intrinsically prohibit the thermal activation process while straining the system. As a result, molecular static simulations give rise to effectively equivalent outcomes as the MD simulations at the very high strain rate limit, which also do not permit thermal activation [27-29]. This equivalence is first analytically demonstrated by Zhu et al. in the dislocation nucleation in Cu[28], then by Weinberger et al. in the dislocation nucleation in Au[27], and very recently by Fan et al. in the dislocation flow in bcc Fe[29]. For the sake of simplicity, we will therefore refer to both scenarios as ‘high-strain-rate’ studies in the rest of this paper. Generally, these high-strain-rate results are either directly compared with experiments [21] or incorporated into continuum approaches [22]. An important question emerges from such an approach - can the high-strain-rate studies represent accurately the mechanisms taking place in experiments driven at much lower strain rates? Not only the mechanism, but the magnitudes of critical stresses that determine the unpinning of dislocations are also at stake when simulated only at very high strain rates. Therefore understanding the mechanisms by which defects alter system performance at long time scale is particularly important and challenging to exploit the connection between nanoscale defects and mesoscale phenomena[138]. An important example that supports this question is a seeming controversy between the simulated prediction and the experimental observation over the interaction mechanism between an edge dislocation and a defect cluster made of self interstitial atoms in Zr. In molecular static calculations simulated at 0 K[25], the dislocation and the defect cluster (obstacle) was found not to interact with each other. In other words, the dislocation simply passes through the obstacle upon induced shear deformation, leaving both of the defect structures fully recovered as a result of the interaction[25]. In those simulations, the system was driven by the applied shear strain only without any thermal activation. These conditions are akin to the high strain rate and low temperature limit [27-29] because they don’t give rise to thermal activation over sufficiently long time, as discussed above. While in tensile experiments, under very

low strain rates ( $10^{-4}\text{s}^{-1}$ ) and high temperature (600 K), formation of dislocation channels was found [30]. Presence of dislocation channels is interpreted as the absorption of the obstacles on the slip plane by the moving dislocations. The experimental results starkly differ from the simulation results described above. Another inconsistency between experiments and high strain rate simulation comes from the interaction between dislocation and perfect stacking fault tetrahedra (SFT). In the *in situ* TEM experiments, the SFTs are observed to be absorbed by the dislocation [139]; while in MD simulations, the dislocations pass the perfect SFTs without absorbing them [140]. Although a free surface effect has been introduced for trying to reconcile the two results [141], the difference of the strain rates used in the experiments versus the MD simulations is still a possible reason that leads to the discrepancy, as suggested by Matsukawa et al [139].

The discrepancies mentioned above between experiments and atomistic simulations raises a key challenge - by straining the system too fast in traditional atomistic simulations, are we missing thermally activated processes which then do not have enough time to take place? Furthermore, it has been observed from both simulations and experiments that temperature also affects the interaction mechanisms between dislocations and obstacles. In MD simulation for example, for the interaction between a dislocation and a SIA loop in bcc Fe, the SIA loop is absorbed by the dislocation at high temperature, while both the dislocation and SIA loop recover fully at low temperature, under the same applied strain rate around  $10^6\text{s}^{-1}$  [9, 20]. In tensile experiments, both the number [142] and the width [143] of the dislocation channels are observed larger at high temperature than at low temperature. These findings suggest that both the temperature and the applied strain rate should together determine the interaction mechanism because of the presence of thermally activated processes. However, the following questions remain open: are the strain rate effect and temperature effect independent from each other or do they act in concert with each other? In previous studies on pure dislocation systems [27-29], it has been demonstrated that there does exist a coupling between applied strain rate and thermal activation, which can affect the strength of the materials. Does the



similar argument still hold in a more complicated system involving the dislocation-obstacle interaction? If it does, what is the relation between these two driving factors? And consequently, how can such an interrelation determine the interaction mechanisms between dislocations and obstacles under a wide range of conditions? To address these challenges, a quantitative model applicable over a wide range of strain rate and temperature conditions is desired.

## 4.2.2 Problem Statement and System Set Up

In this section, as a first model problem, we study a unit processes that define the dislocation-obstacle interaction over a wide range of strain rates and temperatures in hcp Zr. This realization is enabled by the implementation of ABC method [40, 76-79, 81], which has been introduced in Chap 2 and demonstrated robust in reaching a wide range of time scales, without limiting the simulation of dislocation-defect interactions to very high strain rates. We theoretically derive the impact of applied strain rate on the thermally activated interaction processes using transition state theory (TST), and inform the TST framework by ABC calculations. This approach enabled us to uncover dislocation-defect interaction mechanisms over a very wide range of strain rates ( $10^{-7}\text{s}^{-1}$  to  $10^8\text{s}^{-1}$ ), which is far beyond the reach of traditional MD methods. We demonstrate that the dislocation-defect interaction mechanism is an outcome of the competition between thermal activation and strain rate, and provide an interaction mechanism map within a two-parameter space consisting of temperature and strain rate. The so-derived mechanism map provides a means to explain the underlying reason for the various dislocation-defect interaction mechanisms previously observed at different temperatures [9, 20]. For the particular defect system chosen in hcp Zr, at high temperatures and low strain rates, the thermally activated process has enough time to take place and leads to the absorption of the obstacle by the dislocation; while at low temperatures and high strain rates, the process does not have enough time to be thermally activated and the dislocation passes through the obstacle, leaving both defects recovered. This finding demonstrates that the seeming controversy between experiments [30] and previous

simulations [25] mentioned above is actually not a real controversy. The different results arise rather because of the different conditions in the simulations and in the experiments reported above. The results at high strain rates are validated quantitatively by MD simulations as a function of temperature on the same defect system. Such a capability to predict the characteristics of dislocation-defect interactions over a wide range of conditions allows us to connect the atomistic results to models at the meso-scale for simulating the plasticity of metals.

Particularly in this study we focus on the interaction between edge dislocation in the prism plane and SIA cluster in the basal plane. The planar structure of SIA clusters in the basal plane were systematically observed in previous displacement cascade simulations [144], suggesting that this defect cluster is energetically very favorable to exist in Zr during irradiation. On the other hand, tensile test experiments demonstrate that the prismatic slip system in Zr alloys is more affected by irradiation than the basal slip system [30]. We set up a model system including the  $1/3 \langle 11\bar{2}0 \rangle \{1\bar{1}00\}$  edge dislocation and a basal 5-SIA cluster in Zr. The simulation system has the dimensions 14.46 nm\*4.15 nm\*13.51 nm, and contains 34181 Zr atoms. The periodic boundary conditions are applied along the dislocation line direction, and the Burgers vector direction, respectively. An embedded atom method (EAM) type interatomic potential for Zr metal, the Ackland-Wooding-Bacon (AWB95) potential[112], is employed in this study.

### 4.2.3 Results and Discussion

We studied the interaction between the dislocation and the SIA cluster first under static conditions, i.e. at 0 K, and then with varying strain rates at a finite temperature. Figure 4.4 shows the strain-stress curve and associated critical configurations for this interaction under static conditions.

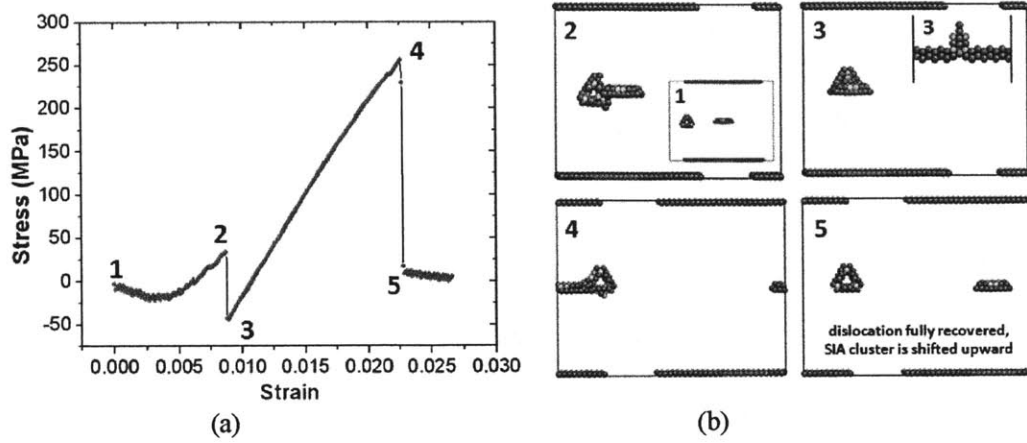


Figure 4.4: (a) The strain-stress curve for the interaction between the  $1/3 \langle 11\bar{2}0 \rangle \{1\bar{1}00\}$  prismatic edge dislocation and a basal 5-SIA cluster in hcp Zr. The numbers 1-5 represent the critical points during the interactions. (b) The corresponding critical configurations during the interaction.

It can be seen that the early phase of the interaction between the dislocation and the SIA cluster is repulsive. This leads to a stress increase from configuration 1 to 2. Then the dislocation is pinned to the SIA cluster along with a stress relaxation at 3. This pinning interaction consists of a glide motion of the dislocation and a climb of the SIA cluster (Figure 4.4 (b), configuration 3). Upon further shear strain, there is a monotonic increase of the stress from 3 to 4. When the stress increases up to 250 MPa, the dislocation and SIA cluster are detached from each other, leading to the sharp stress relaxation. The dislocation structure is fully recovered after the interaction. The SIA cluster structure is fully recovered as well, except being shifted one plane above the original glide plane. This mechanism is identical to the results from a previous static simulation in a larger system [25].

We then studied the same unit process as a function of strain rate at finite temperature, 300 K. Three different strain rates:  $10^5 \text{s}^{-1}$ ,  $10^4 \text{s}^{-1}$ , and  $10^3 \text{s}^{-1}$  were specifically assessed in the same way as above. Figure 4.5 (a) shows the corresponding strain-stress curves and the associated critical configurations, with the attempt frequency of  $10^{13} \text{s}^{-1}$ . It can be seen that all the critical stresses at this temperature are lower than the critical stress found from the static calculation.

Higher strain rate leads to higher critical stress. There is about 100 MPa difference between each of the critical stresses for the strain rates from  $10^5\text{s}^{-1}$  to  $10^4\text{s}^{-1}$  to  $10^3\text{s}^{-1}$ . This critical stress dependence on strain rate indicates that the applied strain rate can couple with the thermal activation and affect the materials strength, which is qualitatively consistent with the previous study on dislocation flow behavior [29].

Interestingly, and importantly, not only the critical stresses but also the interaction mechanisms depend on the applied strain rate. As seen in Figure 4.5 (a), two distinct interaction mechanisms are found. For the relatively high strain rate condition of  $10^5\text{s}^{-1}$ , the interaction mechanism is the same as that found under 0 K conditions, leaving both the dislocation and SIA cluster completely recovered to their original configuration (Figure 4.5 (a), configuration 3 and 4). We refer to this interaction as the “recovery” mechanism. For the lower strain rates at  $10^4\text{s}^{-1}$  and  $10^3\text{s}^{-1}$ , however, the SIA cluster is absorbed by and moves together with the dislocation. We refer this interaction as the “climb” mechanism. More specifically, in the climb mechanism at the lower strain rate (i.e.  $10^3\text{s}^{-1}$ ), the absorbed SIA cluster spreads into an extended jog structure (seen in configuration 1 in Figure 4.5 (a)); while for higher strain rate (i.e.  $10^4\text{s}^{-1}$ ), the absorbed SIA cluster is in a narrow jog structure. The reason is that the SIA does not have enough time to spread out and fully interact with the dislocation at this relatively higher strain rate (seen in configuration 2 in Figure 4.5 (a)).

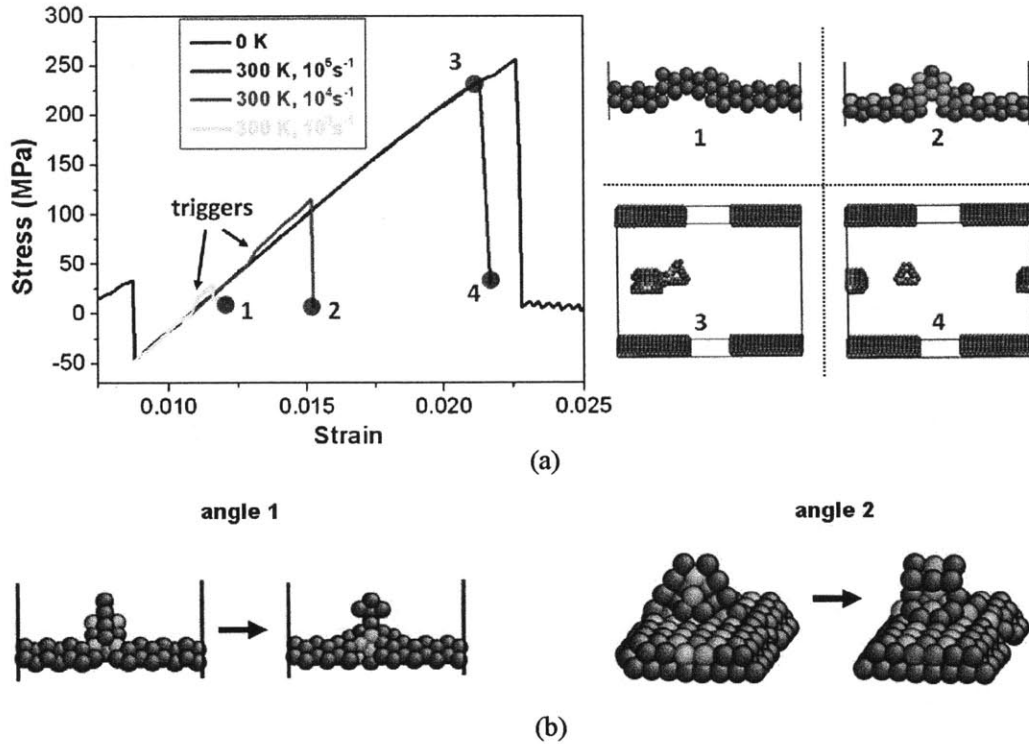


Figure 4.5 (a) (left) The stress-strain curves under different strain rate conditions, and (right) associated critical configurations (1-4 shown in (a)). (b) The unit process governing the kinks in the strain-stress curve in (a) for the lower strain rate cases.

It is important to know the quantitative boundaries that differentiate these two mechanisms because they have drastically different consequences on the mechanical properties. First, as the naming implies, the climb mechanism assists the dislocation climb that is relevant to macroscopic degradation in the context of creep and growth. In addition, this mechanism also can sweep the defects (SIAs in this case) and contribute to the formation of dislocation channels in the prism plane. The formation of dislocation channels can drastically reduce the material's work hardening capacity and may also be responsible for the nucleation of cracks due to the channel-boundary interaction [145, 146]. However, there are no such consequences from the recovery mechanism.

Because these two mechanisms have very different impact on the microstructure and mechanical properties of the material, predicting under what conditions either mechanism predominates is important. In order to elucidate the underlying reason that leads to the two different mechanisms as a function of strain rate, we examine the strain-stress curves as well as the associated atomic configurations. A trigger event appears in the stress-strain curve for the strain rates of  $10^4\text{s}^{-1}$  and  $10^3\text{s}^{-1}$ . The associated atomistic configurations with the trigger reaction are shown in Figure 4.5 (b). In this reaction, few of the atoms on the bottom edge of the SIA cluster are pushed upwards, and this leaves a relatively low-density structure near the dislocation core. The low-density structure formed in this trigger reaction provides more space for the reconstruction of the local atoms, and ultimately assists the absorption of SIA cluster by the dislocation, as seen in Figure 4.5 (a) (configurations 1 and 2).

To predict the critical stresses, reaction mechanisms and final defect structures upon the dislocation-obstacle interaction, it is necessary to quantitatively capture dependence of the trigger reaction on strain rate and temperature. For this purpose, we assess the thermally activated reaction paths and the corresponding energy barriers, and how they are affected by the applied strain rate. We first identified the trigger reaction energy barriers under different strain conditions. As seen in Figure 4.6 (a), the trigger event can only happen in the strain regime from  $\varepsilon_i$  to  $\varepsilon_f$  (the light blue region in the figure). The reason is that the dislocation and SIA cluster do not contact with each other yet before  $\varepsilon_i$ , while beyond  $\varepsilon_f$  the dislocation will simply pass through the SIA cluster and leave both defects fully recovered, following the interaction “recovery” mechanism. The trigger barrier in this regime decreases first as a function of strain, and reaches a minimum around 0.33 eV at the critical strain around 0.015. At larger strain states, however, the trigger barrier increases. This overall parabola shape behavior might be related to the symmetric parabola shape distribution of Burgers vector for  $1/3\langle 11\bar{2}0 \rangle \{1\bar{1}00\}$  edge dislocation within AWB95 potential [113]. Whether the trigger event can happen or not is actually determined by the competition between the thermal activation of that event and the

applied strain rate. If the strain rate is too high, there is not enough time for the thermal activation to take place, *i.e.* the trigger reaction cannot proceed. On the other hand, the higher the temperature, the less time is needed for the thermal activation, and more likely that this trigger reaction will proceed. Similarly, a lower strain rate permits more time for the thermally activated trigger reaction to occur as well. In our previous work, we have demonstrated how the thermal activation is affected by the strain rate under the tensile strain rate experiment conditions [29]. In summary, the key is the presence of stress (or equivalently strain) dependent activation energies,  $E(\varepsilon)$ , that couple with temperature in the TST formalism to describe the dislocation motion. Particularly in this study, we obtained the activation energy profile  $E(\varepsilon)$  following the algorithm described above and shown in Figure 4.6 (a). The activation probability of the trigger event can thus be calculated as a function of temperature and applied strain rate as,

$$P_{trigger} = \frac{1}{\dot{\varepsilon}} \int_{\varepsilon_i}^{\varepsilon_f} k(\varepsilon) e^{-\frac{1}{\dot{\varepsilon}} \int_{\varepsilon_i}^{\varepsilon} k(\varepsilon') d\varepsilon'} d\varepsilon \quad (\text{Eq.4.9})$$

where  $k(\varepsilon) = \nu_0 e^{-E(\varepsilon)/k_B T}$  represents the thermal activation rate of the trigger event,  $\dot{\varepsilon}$  is the applied strain rate condition,  $\varepsilon_i$  and  $\varepsilon_f$  represent the initial and final strain states for the trigger interaction, respectively.

We can then introduce the criterion for identifying whether the trigger event can be effectively activated or not. We choose a threshold probability for this event,  $p_c$ , which should have a value of 0.5 or greater. If  $P_{trigger} \geq p_c$  then the trigger event will proceed, while if  $P_{trigger} < p_c$ , the dislocation will pass through the SIA cluster and the defects get recovered.

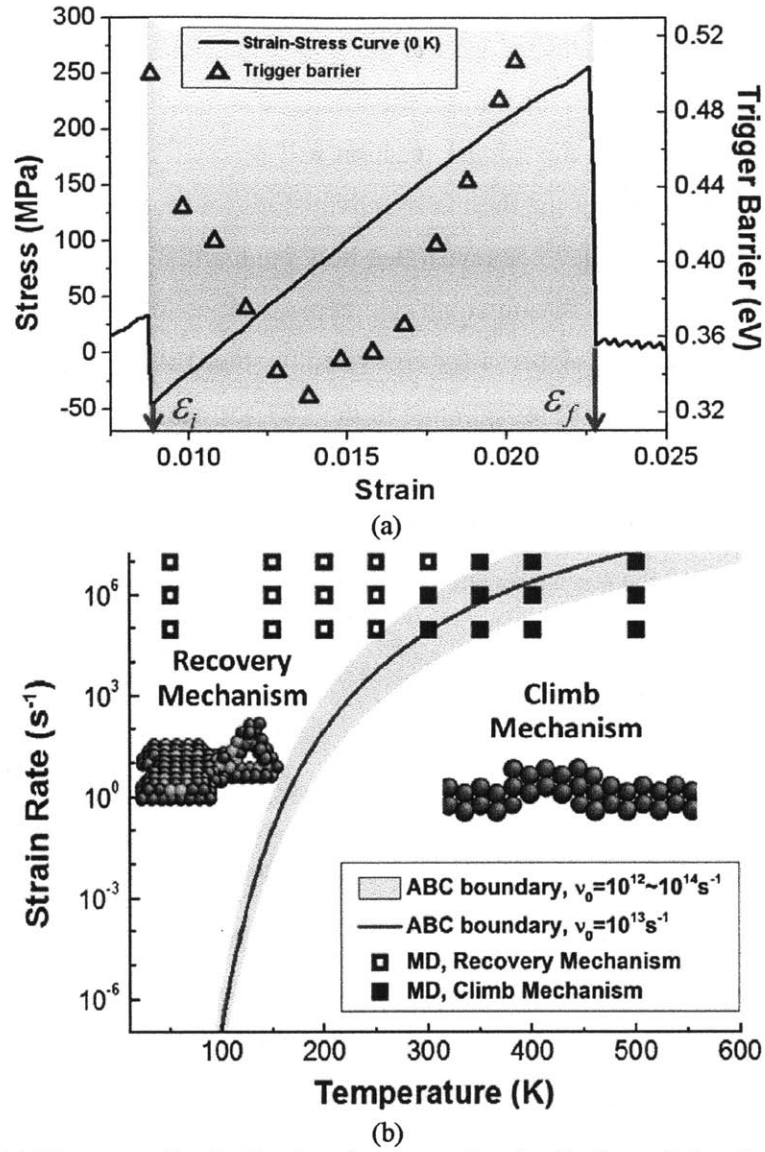


Figure 4.6 (a) The energy barrier for the trigger reaction that leads to dislocation jog via the absorption of the SIA cluster, shown here as a function of strain, associated with the strain-stress curves in Figure 4.5 (a). (b) The strain rate-temperature diagram that provides the boundary for the transitions between the two mechanisms that govern the dislocation-SIA cluster interaction. The red line is the calculated boundary with the attempt frequency of  $10^{13} s^{-1}$ . The upper boundary of the light blue stripe represents the results with the attempt frequency of  $10^{14} s^{-1}$ , while the lower boundary represents the results with the attempt frequency of  $10^{12} s^{-1}$ . The blue data points are the MD results. In particular, the open squares represent the result of mechanism I, that dislocation simply passes through the SIA cluster; while the filled squares represent the mechanism II, that the SIA cluster is absorbed by the dislocation.



The mechanism map thus-constructed for visualizing the dependence of the dislocation-SIA cluster interactions on temperature and strain rate is shown in Figure 4.6 (b). The red curve and the blue stripe around the red curve determine the boundary for the two mechanisms on this diagram. On the left side of the boundary, i.e. at high strain rate and low temperature, the interaction follows the recovery mechanism, that both defects get recovered eventually; while on the right side of the boundary, i.e. at low strain rate and high temperature, the interaction follows the climb mechanism, that the SIA cluster is absorbed by and moves together with the jogged dislocation. Here, we show the results with  $p_c = 0.632$ , where the value 0.632 comes from  $\int_0^1 e^{-x} dx \approx 0.632$ . A sensitivity analysis of the mechanism boundary to the choice of  $p_c$  from 0.5 to 0.632 showed insignificant variation in the results. On the other hand, the results are more sensitive to the choice of the attempt frequency, and the effect is shown in Figure 4.6 (b) as the blue stripe ranging from the  $10^{12}\text{s}^{-1}$  to  $10^{14}\text{s}^{-1}$ . The upper bound of the stripe represents the results with the attempt frequency of  $10^{14}\text{s}^{-1}$ , the lower bound represents the results with the attempt frequency of  $10^{12}\text{s}^{-1}$ , and the red line inside the stripe is the resulting boundary with the attempt frequency of  $10^{13}\text{s}^{-1}$ .

The derived mechanism map is benchmarked against direct MD simulations on the same system. Although MD method is limited at high strain rate conditions only, it is possible to partially examine the mechanism map and cross the mechanism boundary by varying the simulation temperature at high strain rates. In particular, MD simulations were performed under three different strain rates ( $10^5\text{s}^{-1}, 10^6\text{s}^{-1}, 10^7\text{s}^{-1}$ ), and eight different temperatures (50K, 150K, 200K, 250K, 300K, 350K, 400K, 500K). At strain rates of  $10^5\text{s}^{-1}$  and  $10^6\text{s}^{-1}$ , the transition temperatures from recovery mechanism to climb mechanism are between 250 K and 300 K. At the higher strain rate  $10^7\text{s}^{-1}$ , the transition is postponed and taking place at the temperature between 300 K and 350 K. The summary of MD results is also mapped into the derived mechanism map by ABC method in Figure 4.6 (b). It can be seen that the MD results

are very well quantitatively consistent with the upper boundary with the ABC results, suggesting a prefactor value close to  $10^{14}\text{s}^{-1}$ .

Casting of these interactions as a mechanism map in the temperature-strain rate space also permits us to understand the differences between the prior experimental and molecular static simulation results. In the prior molecular static simulation of the interaction between an  $\langle a \rangle$  edge dislocation and a SIA cluster (the same type of defects as analyzed here) in Zr [25], thermal activation is quenched and consequently the interaction is purely driven by the strain. Therefore, the outcome is the recovery mechanism. The tensile experiments [30], however, were performed at 600 K and  $10^4\text{s}^{-1}$ . This set of conditions maps the interaction to the recovery mechanism (as seen in Figure 4.6 (b)). As noted above, the complete absorption of the SIA clusters by the dislocation can clear the obstacles in the path of the dislocation, and be interpreted as the formation of dislocation channels observed in experiments [30]. As a result, we can say that the experiments and previous simulations are not inconsistent. They rather represent different conditions, and our approach here reconciles those results on the mechanism map. We are cautious to also note that other factors, for example the effect of free surfaces [141], can also induce the formation of dislocation channels. However, our results demonstrate that the magnitude of applied strain rate can be an important factor in determining the formation of dislocation channels, in addition to the previously discussed mechanisms.

In summary, we proposed a new atomistic simulation framework to assess the dislocation-defect interaction mechanisms and critical stresses over a wide range of strain rate conditions for the first time, extending to many orders of magnitude longer time scales than what the traditional MD can capture. Results were cast in a deformation mechanism map, for the first time including strain rate as a key parameter. We implemented this approach to examining a unit process of dislocation-SIA cluster interaction in hcp Zr as a model system. We found two clear interaction mechanisms: (i) the SIA cluster is absorbed by the dislocation; (ii) the dislocation passes through the SIA cluster, leaving behind both the SIA cluster and the dislocation structures fully recovered. We further demonstrated that the

competition between thermal activation and applied strain rate determines which mechanism dominates. The results visualized in a mechanism map can reconcile the previous seeming inconsistencies between experiments and molecular static simulations. Since the two mechanisms have significantly different consequences on the mechanical properties, the derived mechanism map is particularly important for predicting the evolution of the material microstructure.

The approach in constructing the mechanism map is based on a general thermal activation theory under prescribed strain rate [29], and is not limited to the defects discussed here in the Zr system. The framework allows to probe how the thermal activation is influenced by other driving parameters (strain rate in this study), and its consequences to the materials properties. This framework is quite general and hence can be applied to study different materials (*e.g.* glass materials, colloidal system) and the response to different conditions (*e.g.* annealing rate, irradiation rate). Previous MD simulations in bcc Fe report different interaction mechanisms between a dislocation and a SIA loop as a function of temperature [9, 20]. Specifically, at high temperature, the SIA loop is absorbed by the dislocation; while at low temperature, both dislocation and SIA loop are completely recovered. Despite both being at high strain rate, these two different outcomes in bcc Fe can also be understood as a competition of strain rate and temperature, as explained on the mechanism map in Figure 4.6 (b).

The new capability and insights presented here are important because it is clear that extrapolating the results obtained at high strain rates to the low strain-rate regime can lead to inaccurate results. Admittedly, there are still gaps between our simulation and the real experiments, in terms of the system size, types of obstacle and microstructure. On the other hand, this work can serve as a bridge between atomistic simulations and models simulating the meso-scale plastic behavior of metals because of the unique ability to predict deformation mechanisms over a very wide range of time scales.

## **4.3 Inverse Relation between Critical Resolved Shear Stress and Strain Rate – Dislocation-Vacancy Cluster Interaction in BCC Fe**

### **4.3.1 Background and Motivation**

The microstructure of neutron-irradiated structural materials, which mainly consist of ferritic alloys, typically includes super-saturation of point defect and clusters [147]. The interaction between point defects and dislocations is particularly critical to the macroscopic degradation of the materials, and known to have marked effects on the mechanical properties. A particular situation is the inverse relation between the flow stresses and strain rates [148-150]. The inverse relation is known as the negative strain-rate sensitivity (nSRS), and can lead to non-uniformities at macroscopic scale [49]. Several continuum models have been developed to explain the nSRS phenomenon. For example, by assuming the obstacle and dislocation concentrations are time- and strain-dependent, respectively, Estrin et al.'s model can predict an inverse behavior if the homogenous nucleation of obstacles in bulk istakingplace [151, 152]. Recently, Curtin et al. made significant improvement to Estrin et al.'s model by introducing the mechanism of direct single-atomic jump across the dislocation slip plane [48]. In this case study, we consider a unit process of dislocation obstacle interaction in bcc Fe over a wide range of strain rates, from  $10^8\text{s}^{-1}$  down to  $10^3\text{s}^{-1}$ , by using the dynamic implementation of ABC method, as introduced in Sec 2.4. This newly developed algorithm allows direct simulation on much longer time scales than molecular dynamics (MD) limits (higher than  $10^6\text{s}^{-1}$ ) [7]. We show that the critical resolved shear stress (CRSS) of the system is determined by the competitions between thermal activation and strain rate effect.

Even a unit process of dislocation obstacle interaction can result in the nSRS behavior, because of different microstructures induced by the competitions at various strain rate conditions.

### **4.3.2 Problem Statement and System Set up**

Voids form especially in fast neutron irradiation, and act as strong obstacles to the glide motion of edge dislocations[20]. In this paper, we consider the interaction between the  $1/2 \langle 111 \rangle$  edge dislocation and a small vacancy cluster in bcc Fe, as a representative unit process. In particular, we set up a model system including the  $1/2 \langle 111 \rangle$  edge dislocation and a small void containing 9 vacancies in bcc Fe. The simulation system has the dimensions 9.81 nm (x)\*3.51 nm (y)\*12.57 nm (z), and contains 33171 Fe atoms. The periodic boundary conditions are applied on the x- and y-directions, which are the glide direction and dislocation line direction, respectively. The interatomic potential employed in this study is an embedded atom method (EAM) type developed by Ackland *et al*[153].

### **4.3.3 Results and Discussion**

We first studied the interaction between the dislocation and the vacancy cluster under static conditions. Figure 4.7 shows the strain-stress curve, associated potential energy, and corresponding critical configurations for this interaction.

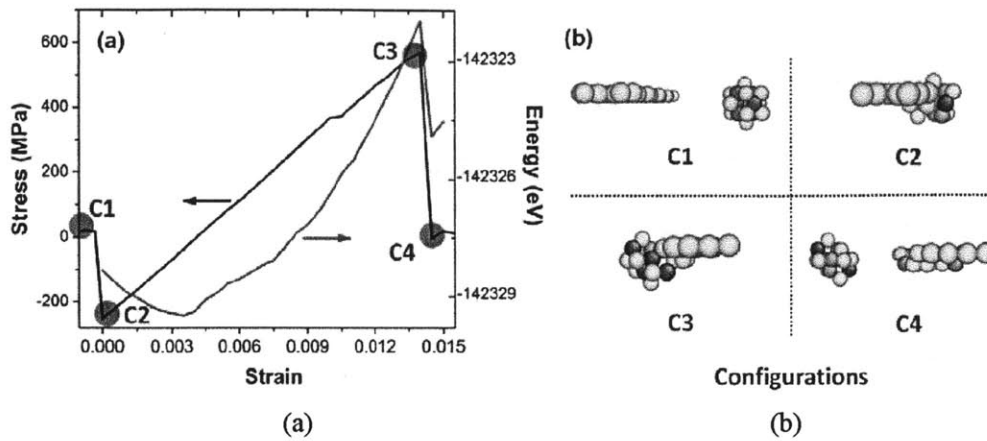


Figure 4.7 (a) The strain-stress curve, and associated potential energy of the system, during the static interaction. (b) The corresponding critical atomistic configurations during the static interaction as shown in (a). The structures are visualized by Atomeye [97], and colored according to different coordination numbers.

In the beginning, the vacancy cluster is on the right side of the dislocation, with the center of mass placed on the glide plane. Upon shear loading, the dislocation is pinned to the vacancy cluster (Figure 4.7 (b), C2) associated with a stress relaxation down to -250 MPa. For the mimicking tensile test experimental condition, it is convenient to study the interaction as a function of strain. The corresponding strain at C2 is therefore set to be zero. With further increasing the strain, there is an almost linear increase of the stress and a parabola like shape of the potential energy, which indicate an elastic deformation behavior. The imperfection of the parabola shape (seen in Figure 4.7 (a)) is due to the mechanical property (e.g. the elastic modulus) changes because of the interaction between dislocation and the cluster. When the stress increases up to 570 MPa, the dislocation and vacancy cluster are detached from each other, leading to the sharp stress relaxation. Two vacancies in the void are absorbed by the dislocation during the static interaction, and a small jog is formed after the interaction (Figure 4.7 (b), C4).

We then studied the same unit process at finite temperature, 300 K, and five different strain rates:  $10^3\text{s}^{-1}$ ,  $10^4\text{s}^{-1}$ ,  $10^5\text{s}^{-1}$ ,  $10^6\text{s}^{-1}$ , and  $10^8\text{s}^{-1}$ , respectively. To benchmark with ABC method, we also performed direct MD simulations on the

same system at the high strain rates of  $10^6\text{s}^{-1}$  and  $10^8\text{s}^{-1}$ , where MD is known to be valid. Figure 4.8 (a-b) show the corresponding strain-stress curves provided by ABC and MD simulation, respectively. It can be seen that all the CRSS under non-zero temperature are lower than the critical stress found from the static calculation. It is also noticed that in the MD simulations (seen in Figure 4.8 (b)), the stress at the beginning is around -180 MPa, which is 70 MPa deviated from the static results (black curve in Figure 4.8 (a)). We identified that this discrepancy is induced by a hydrostatic compression stress produced in the non-zero temperature MD simulations, because of the fixed volume condition. The atomistic configurations after the interaction are shown in Figure 4.8 (c). Compared to 2 vacancies absorbed in static interaction, 5 vacancies are absorbed by the dislocation under 300 K, while different strain rates lead to different atomic configurations after the interaction. In the ABC simulations, a most compact structure of vacancy cluster is formed under  $10^3\text{s}^{-1}$ , as seen in Figure 4.8 (c). The remaining vacancy clusters for the strain rates between  $10^4\text{s}^{-1}$  and  $10^8\text{s}^{-1}$  are in the same structure, while the jogged dislocation at  $10^8\text{s}^{-1}$  has a relatively ripped structure because of the extremely high strain rate. In the MD simulations, the identical vacancy cluster configurations are observed under the same conditions, while the dislocation structures are slightly different from ABC results due to the atom oscillations in non-zero temperature MD simulations.

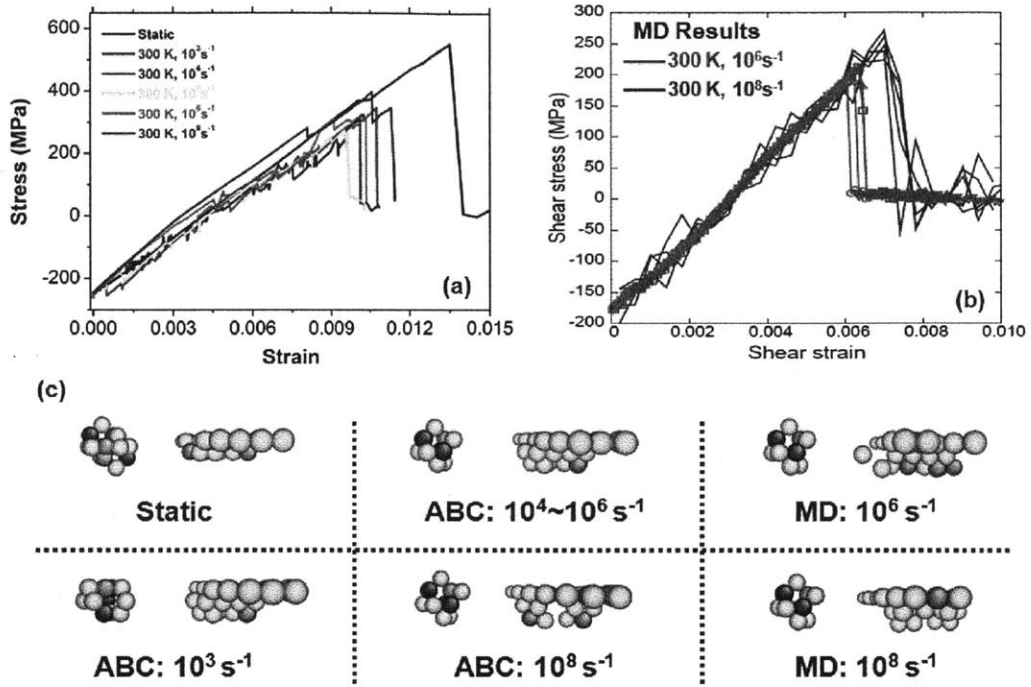


Figure 4.8 (a-b) The stress-strain curves for the dislocation void interaction under different strain rate conditions, provided by ABC and MD simulations, respectively. (c) The associated critical atomic configurations after the interaction.

The CRSS under different strain rates are read off from Figure 4.8 (a-b) and plotted in Figure 4.9. It can be seen from ABC results that, for strain rates higher than  $10^5 \text{ s}^{-1}$ , the CRSS increases as a function of strain rate, which shows a normal relation [7, 19]. In ABC results, the CRSS at  $10^8 \text{ s}^{-1}$  is about 70 MPa higher than the value at  $10^6 \text{ s}^{-1}$ , which is consistent with the difference observed in direct MD simulations. However under the same conditions, there are less than 100 MPa differences of CRSS between ABC and MD simulations. This discrepancy can also be related to the hydrostatic compression in MD simulations, which is similar to the deviation from the static results at the beginning. On the other hand, the choice of the attempt jump frequency in ABC studies can be a factor as well. In the ABC simulations, the attempt jump frequency  $\nu_0$  is set to be a constant  $10^{13} \text{ s}^{-1}$ . However, any deviation from this value can lead to a different CRSS in the end. The lower



values of CRSS in MD simulation suggest a larger  $\nu_0$  number, which might come from the entropy effects.

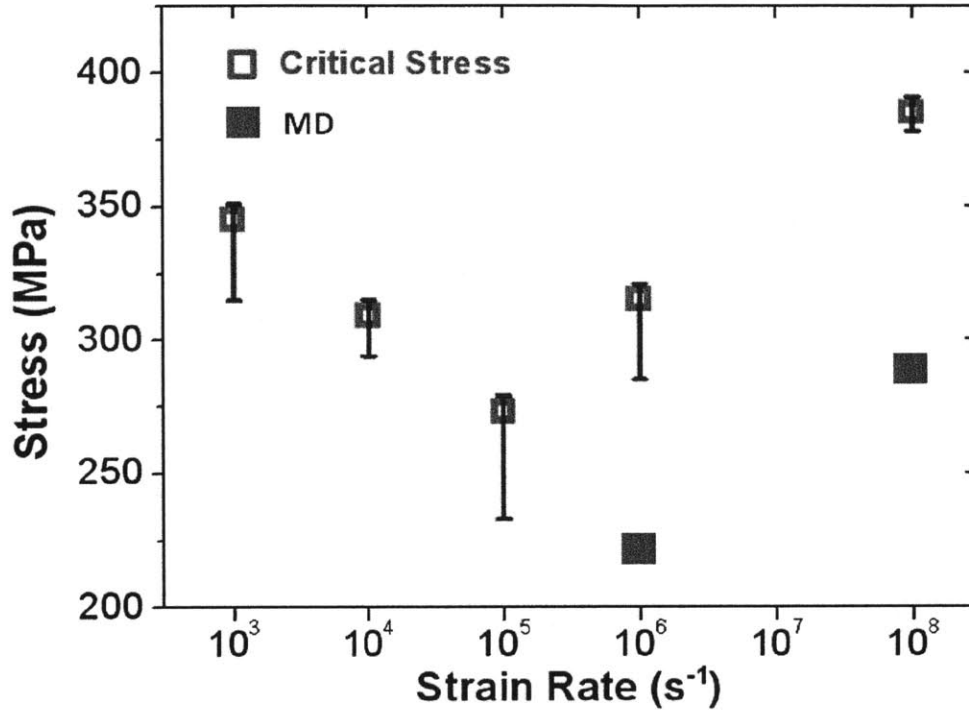


Figure 4.9 The CRSS under different strain rates conditions. Red open squares are the results of ABC framework simulations, while the black squares represent the MD simulations results.

More interestingly, and importantly, the CRSS shows a negative sensitivity to strain rate below  $10^5 \text{s}^{-1}$  in ABC simulations. To understand the underlying mechanism for this inverse behavior, we analyze the energy landscapes and defect structure evolutions under different strain rate conditions. For each set of strain rate, a parabola like shape of the potential energy is observed, similar to the red curve in Figure 4.7 (a). Figure 4.10 (a) shows the energy differences at various strain rate conditions, with respect to the static interaction energy (red curve in Figure 4.7 (a)). As seen in the figure, at relatively low strain rate  $10^4 \text{s}^{-1}$ , there are high frequent fluctuations on the energy difference landscape, which indicates significant amount

of thermal activation events. However for the higher strain rates such as  $10^6\text{s}^{-1}$ , the energy landscape is smoother, which demonstrates that the system is mainly driven by strain deformation induced by the high strain rate.

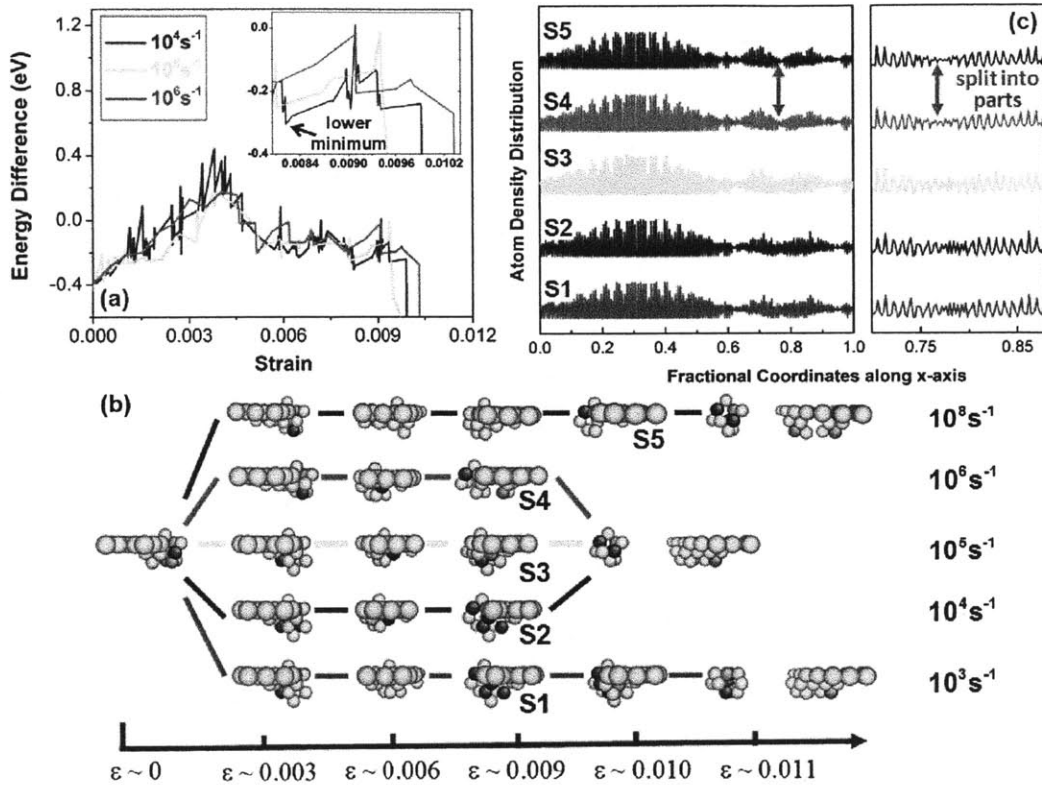


Figure 4.10 (a) The energy differences under different strain rate conditions, with respect to the static energy landscape. (b) The atomistic configurations during the interactions, at various strain rates. (c) The atom density distributions along x-axis, i.e. the  $\langle 111 \rangle$  direction, for structures S1-S5. The vacancy cluster's fractional coordinate along x-axis is about 0.8. It clearly shows that for high strain rates  $10^6\text{s}^{-1}$  and  $10^8\text{s}^{-1}$ , the vacancy clusters are ripped into parts, while such behavior is not observed for lower strain rate conditions.

The evolution of the defect structures under different strain rates are shown in Figure 4.10 (b). At the early strain stage ( $\epsilon \sim 0.003$ ), the vacancy cluster is nucleated downward due to the thermal activation, for those strain rates between  $10^3\text{s}^{-1}$  and

$10^5\text{s}^{-1}$ . However, under high strain rates of  $10^6\text{s}^{-1}$  and  $10^8\text{s}^{-1}$ , no such nucleation is observed because there is not enough time for this event to be thermally activated.

Assisted by thermal activation, the dislocation core glides to the right side of vacancy cluster at medium strain stage (seen in Figure 4.10 (b), the configurations at  $\epsilon \sim 0.006$  for the strain rate between  $10^3\text{s}^{-1}$  and  $10^6\text{s}^{-1}$ ). This process is associated with the energy peak between  $\epsilon = 0.003$  and  $\epsilon = 0.006$  shown in Figure 4.10 (a). On the other hand, for the highest strain rate  $10^8\text{s}^{-1}$ , the dislocation does not glide to the right side of the vacancy cluster until the strain reaches the level around 0.009. In other words, under the condition of  $10^8\text{s}^{-1}$ , the similar interaction mechanism is deferred by a strain amount of 0.003, due to the quenching of thermal activation at extremely high strain rate.

Upon further deformation, the vacancy cluster structures evolve differently at various conditions, as seen from S1-S5 in Figure 4.10 (b). Under the strain rates between  $10^3\text{s}^{-1}$  and  $10^5\text{s}^{-1}$ , the vacancy clusters show downward nucleation due to thermal activations (S1-S3 in Figure 4.10 (b)). However, at  $10^6\text{s}^{-1}$  and  $10^8\text{s}^{-1}$ , the vacancy cluster is ripped into parts (see S4 and S5 in Figure 4.10 (b) and the atom density distribution in Figure 4.10 (c)) rather than nucleated, because there is not enough time for this event to be thermally activated at very high strain rates. On the other hand, the vacancy clusters nucleate to different structures (S1-S3) at the strain rates between  $10^3\text{s}^{-1}$  and  $10^5\text{s}^{-1}$ . S1 and S2 are in a relatively looser structure than S3, and the lower energy minimum in the inset plot of Figure 4.10 (a) indicates that they are energetically more stable than S3. For both the loose structure (S1-S2) and the ripped structure (S4-S5), they have larger surface area as attached to the dislocations than S3 does. Correspondingly, the larger areas induce stronger interactions with dislocations, and thus lead to the higher critical stresses. This explains the reason that the CRSS reaches its minimum at  $10^5\text{s}^{-1}$ , as seen in Figure 4.9.

By comparing the structure evolutions at  $10^3\text{s}^{-1}$  and  $10^4\text{s}^{-1}$ , it can be found that the loose structure of vacancy cluster under  $10^3\text{s}^{-1}$  (S1) further nucleates to another stable configuration, because of more time for thermal activation. Subsequently, this more stable structure leads to a higher CRSS than that in  $10^4\text{s}^{-1}$ . Therefore in the

entire simulated strain rate regime from  $10^3\text{s}^{-1}$  to  $10^8\text{s}^{-1}$ , the CRSS shows a “V” shape as seen in Figure 4.9.

In summary, we have examined an edge dislocation-vacancy cluster interaction in bcc Fe as a model system, by implementing the ABC method in a dynamic framework, as described in Chapter 2. This approach served for extending the atomistic simulation capabilities to low strain rates of deformation as shown also in this model problem. We demonstrated here, too, that the dislocation obstacle interactions are determined by two competitive driving forces: strain rate and thermal activation. Under low strain rates (lower than  $10^5\text{s}^{-1}$ ), thermal activation assists the vacancy cluster in nucleating to more stable states (S1 and S2 in Figure 4.10 (b)). These stable states have a stronger interaction with dislocation and therefore lead to a higher CRSS than that in  $10^5\text{s}^{-1}$ . However under high strain rates, such from  $10^6\text{s}^{-1}$  to  $10^8\text{s}^{-1}$ , there is not enough time for the thermal activation of the vacancy cluster. In contrast, the vacancy cluster is split into parts (S4 and S5 in Figure 4.10 (b)) due to the high strain rate. The parts of vacancy cluster have a larger total area attached to the dislocation than the compact structure in  $10^5\text{s}^{-1}$  (S3 in Figure 4.10 (b)). It therefore also leads to a stronger interaction with the dislocation and thus a higher CRSS. All these together explain the underlying mechanism for the “V” shape relation between CRSS and strain rate, with the minimum at  $10^5\text{s}^{-1}$  in this problem. The interaction at high strain rates are directly benchmarked against MD simulations. The CRSS-strain rate relations are qualitatively consistent with each other. Two studies also show the same atomic configuration after the interaction. The quantitative discrepancies might arise because of the hydrostatic compression in MD simulations, or the choice of the attempt jump frequency in ABC studies. The lower value of CRSS in MD might suggest a non-negligible entropy effect.

The inverse behavior between CRSS and strain rate is known as nSRS phenomena, and can induce some detrimental effects on the materials. For example, the inverse behavior results in the decreased ductility and strength of the materials, and correspondingly generates instabilities in deformation of materials [48, 49]. Understanding and explaining such behavior are therefore critical for the material

design strategies. The nSRS phenomenon is typically studied by considering a number of variables, such as temperature, strain rate, defects concentration, grain size, etc. In this case study, we particularly study the strain rate effect on the strength of the system. Through direct atomistic simulation we demonstrate that, in addition to previously proposed continuum models [48, 151, 152], the unit process of dislocation-obstacle interaction can induce the nSRS behavior as well, due to the coupling between the thermal activation and strain rate. In fact, the coupling effect does not only contribute to nSRS, but also results in other important phenomena, such as flow stress up-turn behavior [29], and dislocation channel formation (discussed in Sec 4.2).

Admittedly, there are still gaps between our simulation and experiments (in terms of the system size, type of obstacle, range of strain rate, etc). On the other hand, the modeling in this chapter provides a general framework to capture the coupling effect between different variables under more realistic conditions which were not possible to simulate till now by other atomistic methods. It can therefore be applied to study other systems governed by complicated driven forces, and shed some light on the materials design under extreme conditions.

## **Chapter 5**

# **The Interface Connecting Atomistic Simulation to Engineering Scale Model**

Often material degradation is governed by an aggregate of multiple modes of mechanisms, rather than a dominant unit process. Under such circumstances, it is necessary to connect atomistic simulations to a higher level modeling framework that can accommodate all the involved unit processes and treat these processes in a self-consistent manner. This chapter proposes an interface connecting the atomistic simulations discussed in Chapters 2-4 to larger length-scale methods. In particular, we develop a suitable set of constitutive relations and provide an illustrative example to show how the ABC-based atomistic results can be fed into the visco-plastic self-consistent (VPSC) model, a well-known engineering scale model developed at Los Alamos National Laboratory. This connection therefore provides a roadmap to enable the multiscale modeling of microstructure evolution.

## **5.1 Atomistic Interface to Engineering Scale Model**

### **5.1.1 Background and Visco-Plastic Self-Consistent (VPSC) Model**

We have shown in Chap 4 that some important mechanical properties are controlled by well-defined unit processes, e.g. the dislocation glide in flow stress, and the dislocation-obstacle interaction in dislocation channeling. Such direct connection between a property and a dominant elementary mechanism make it possible for directly bridging the atomic scale simulation to the engineering scale degradation without introducing an intermediate step. However, for many other phenomena (e.g. growth and creep), the overall degradation is an aggregate of multiple modes of deformation, rather than determined by a unit process. For example, in a polycrystal system the total deformation is a cumulative behavior over all single crystal grains, whose deformation is further an aggregate of different slip systems and different modes (e.g. the thermal creep component and the irradiation component) [50]. Under such circumstances, it is not possible to directly deduce the macroscopic degradation behavior from the atomistic simulation on a unit process. Correspondingly, one needs an intermediate model at engineering scale, which can be used to explain or predict the materials macroscopic degradation by incorporating different unit processes assessed by atomistic techniques.

VPSC model is a well-known constitutive engineering scale model for describing the polycrystalline materials deformations in the context of thermal creep, irradiation creep, and irradiation growth [50-52, 154]. The basic idea of VPSC is to write down the overall deformation as an aggregate of all involved modes, i.e. the contributions from each single crystal grain, from each slip system in a given single crystal, and from the environment related components, such as thermal component

and irradiation component. Then the set of equations are solved in a self-consistent manner. Each single deformation mechanism in VPSC relies on several parameters, which can be in principle be obtained by atomistic simulation, though most of them are set empirically at current stage [51, 52, 154]. In other words, if one can provide the required parameters accurately from the atomic level, VPSC can become a more effective and reliable model to predict the materials degradation over a wide range of conditions. In the following section, we will discuss the proposed atomistic interface to the VPSC model.

### 5.1.2 Atomistic Interface to VPSC Model

As we have introduced in Chap 4, the mechanical properties of structural materials are significantly affected by the interaction between dislocations and irradiation induced defects [24, 25, 30, 44-47]. Therefore, it is important to understand the interaction mechanisms between dislocations and obstacles, and particularly how the interaction would be affected by the applied stress, in the relevance to the climb of dislocations that contribute to irradiation creep and to the transition to plastic yield with deformation rates higher than encountered in irradiation creep.

In VPSC model, the current form of the climb rate in VPSC[114] is expressed as below,

$$\dot{\epsilon}_{ij}^{climb} = \sum_k \rho^{(k)} b_i^{(k)} b_j^{(k)} (\Phi^{(in)t} - \Phi^{(vac)})^c \quad (\text{Eq.5.1})$$

where  $\rho$  represents the dislocation density,  $b$  represents the burgers vector,  $\Phi^{(in)t}$  and  $\Phi^{(vac)}$  represent the flux of interstitials and vacancies absorbed by the dislocation, and they are functions of applied stresses and temperatures.

Under neutron irradiation, however, not only mobile point defects, but also sessile clusters are produced in the displacement cascade [144]. The interactions between dislocations and irradiation induced defects can therefore be divided into two categories: the absorption of mobile point defects by dislocation, and the moving dislocation climb over the sessile defect clusters, respectively. The latter category of



interaction, which was studied specifically in Chapter 4 of this thesis, is especially important when the instantaneous point defect density is not very high, for example, in accident conditions where neutron flux is low, as in loss-of-coolant accident (LOCA). Therefore we can rewrite the overall dislocation climb rate by additively combining both these two contributions, as expressed below,

$$\dot{\varepsilon}_{ij}^{climb} = \sum_k \rho^{(k)} b_i^{(k)} b_j^{(k)} (\Phi^{(int)} - \Phi^{(vac)}) + \sum_s \rho_{disl.} c_{sessile}^{cluster} \dot{\gamma}_{ij}^s(\sigma, T) \quad (\text{Eq.5.2})$$

where the first term on the RHS represents the absorption of vacancies and interstitials by the dislocation that has been introduced above in Eq. 5.1. The second term is what we introduce as a new additive contribution, and represents the climb rate attributed to the interaction between dislocation and sessile defect clusters. In the second term,  $\rho_{disl.}$  represents the moving dislocation density,  $c_{sessile}^{cluster}$  represents the concentration of sessile cluster,  $\dot{\gamma}_{ij}^s(\sigma, T)$  represents the climb rate for a specific slip system at different stresses and temperatures.  $\dot{\gamma}_{ij}^s(\sigma, T)$  can be calculated via atomistic simulation. In sum,

Given that we have studied several examples on the interactions between dislocations and sessile obstacles in Chap 4, in this section we will mainly focus on the contribution of the second term. The specific relation between strain rate and applied stress is governed by a constitutive formula below [52],

$$\dot{\gamma}^s = \dot{\gamma}_0 \left( \frac{\tau^s}{\tau_0^s} \right)^{n_g} \quad (\text{Eq.5.3})$$

where  $\tau^s$  is the applied stress,  $\tau_0^s$  is the critical stress for present slip system,  $n_g$  is the power index,  $\dot{\gamma}_0$  is the prefactor, and  $\dot{\gamma}^s$  is the strain rate of present slip system.

To provide atomistically-derived parameters into the VPSC model, an interface connecting atomistic simulation to VPSC model has been suggested [52], however this relation was not implemented by connection to an atomistic code before. The expression is below:

$$\dot{\gamma}^s = \dot{\gamma}_0 \exp \left\{ -\frac{\Delta F(\tau^s)}{kT} \right\} \quad (\text{Eq.5.4})$$

There are two important parameters in the formula above,  $\dot{\gamma}_0$  and  $\Delta F(\tau^s)$ .  $\dot{\gamma}_0$  is the prefactor of the strain rate, which is relevant to the interaction mechanism between dislocation and obstacle, e.g. the number of vacancies/interstitials absorbed by dislocation and contributed to the climb.  $\Delta F(\tau^s)$  is the corresponding activation energy as a function of applied stress. In the following section, we will provide an example to illustrate how to obtain these parameters from atomistic simulation.

### 5.1.3 Connecting Atomistic Model to VPSC – Example on Dislocation-Void Interaction

In this section, to demonstrate the capability to capture the interaction of sessile clusters and dislocations, we examine a model system: the  $1/3 \langle 11\bar{2}0 \rangle \{1\bar{1}0\}$  edge dislocation and its interaction with anano-void containing 19 vacancies. We employ ABC method to study the interaction mechanisms at different stress level, and then combine with the NEB method to get the accurate activation energy. The derived mechanisms and associated barriers can be fed into the VPSC model discussed above.

Figure 5.1 (a-b) shows the static interaction under zero applied stress, and yield stress, respectively.

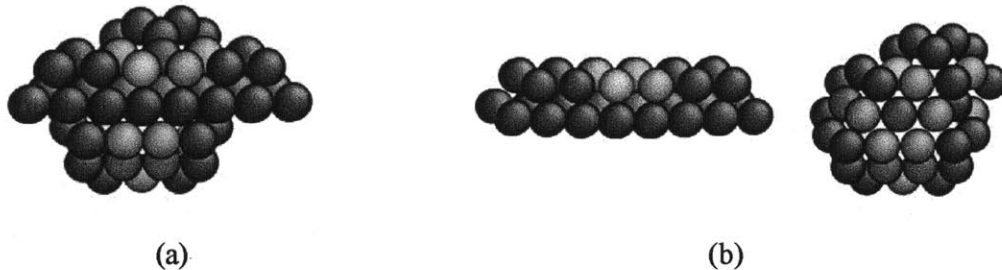
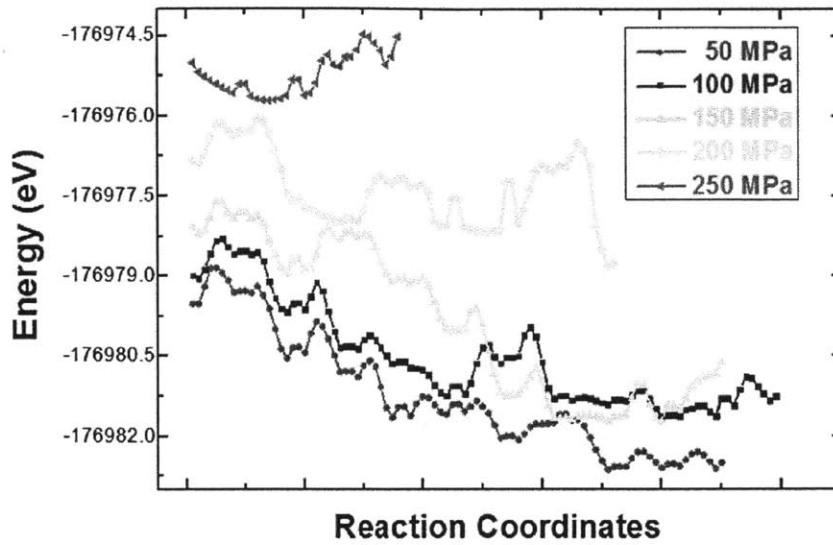


Figure 5.1 The interaction mechanism between  $\langle a \rangle$ -type edge dislocation and vacancy cluster under (a) 0 MPa, and (b) yield stress  $\sim 300$  MPa, respectively.


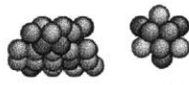


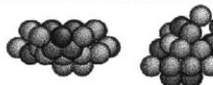
The yield stress for this interaction is around 300 MPa. Under this stress condition, the dislocation glides through the vacancy cluster without absorbing any

vacancies. Correspondingly, the prefactor  $\dot{\gamma}_0$  in Eq.(5.4) at higher stresses than 300 MPa should be zero.

We then employ ABC method to study the interaction at different stress conditions, and the results are shown in Figure 5.2.



(a)

Applied Stress	Effective Barrier	Interaction Mechanism
50 MPa	0.67 eV	 12 vacancies absorbed
100 MPa	0.74 eV	 10 vacancies absorbed
150 MPa	0.60 eV	 14 vacancies absorbed
200 MPa	0.83 eV	 10 vacancies absorbed
250 MPa	0.53 eV	 4 vacancies absorbed

(b)

Figure 5.2 (a) The energy landscape of the dislocation-void interaction at different stress conditions. (b) The corresponding effective barriers and interaction mechanisms at different stress conditions.

Figure 5.2 (a) shows the energy landscape of the dislocation-void interaction at different stress conditions. It can be seen that the shape of the energy landscapes are different at varying stress conditions, and this indicates different interaction mechanisms and activation barriers. Figure 5.2 (b) displays the effective barrier as a function of stress, deduced from the energy landscape in Figure 5.2 (a), and the atomistic configurations that reveal the interaction mechanisms. As seen in Figure 5.2 (b), there is a significant stress effect on the interaction mechanism (specified as the number of vacancies absorbed). This corresponds to different prefactors  $\dot{\gamma}_0$  at various applied stresses, i.e. semi-quantitatively, the prefactor at 150 MPa should be more than three times larger than the value at 250 MPa since three times more vacancies are absorbed and hence contribute to the dislocation climb.

The effective energy barrier also changes as a function of stress. According to transition state theory, the climb rate for this particular system can be expressed as,

$$\dot{\gamma} = \dot{\gamma}_0(\sigma) \cdot \exp[-E(\sigma)/k_B T] \quad (\text{Eq.5.5})$$

where  $\dot{\gamma}_0(\sigma)$  and  $E(\sigma)$  are the prefactor and activation energy, respectively, and they are both functions of stress. The prefactor  $\dot{\gamma}_0(\sigma)$  should be proportional to the number of vacancies absorbed by the dislocation, and can therefore be expressed as,

$$\dot{\gamma}_0(\sigma) = \nu_0 \cdot N_{abs} \quad (\text{Eq.5.6})$$

where  $\nu_0$  is a stress-independent constant with the unit of  $s^{-1}$ , while  $N_{abs}(\sigma)$  is the number of vacancies absorbed by the dislocation as shown in Figure 5.2 (b).

An accurate determination of  $\nu_0$  may require further calculations on the basis of the shape of the interaction energy landscape, or by fitting and extrapolating from the MD simulations or experiments. However, we can identify the climb rates, at least semi-quantitatively, by defining a dimensionless reduced climb rate as:

$$\hat{\gamma} \equiv \dot{\gamma} / \nu_0 = N_{abs}(\sigma) \cdot \exp[-E(\sigma)/k_B T] \quad (\text{Eq.5.7})$$

For this particular system, we plot the reduced climb rate as a function of temperature, under different stress conditions. As shown in Figure 5.3, the climb rate

increases as a function of temperature. 150 MPa and 250 MPa give the highest climb rate, due to either the large prefactor (for 150 MPa), or the smaller activation energy (for 250 MPa). Particularly, at the temperatures below 650 K, the maximum climb rate happens at 250 MPa; while for higher than 650 K, the maximum climb rate happens at 150 MPa.

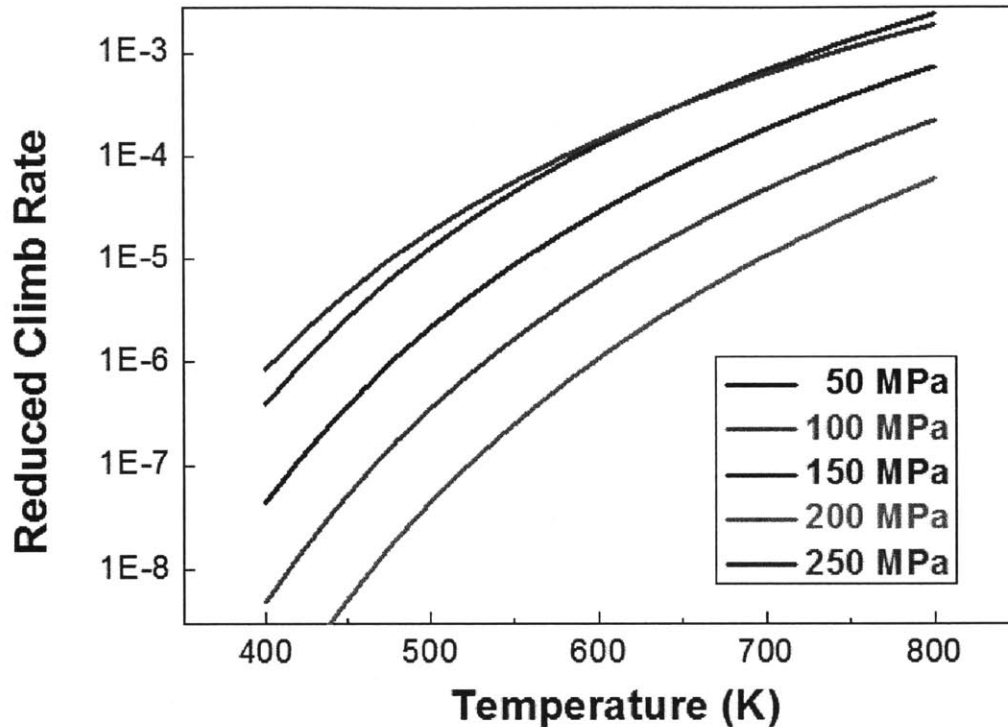


Figure 5.3 The reduced climb rate, following the definition in Eq.(5.7), as a function of temperature at different stress conditions.

#### 5.1.4 Provide Physical Based Description to Mesoscale Constitutional Model: Example on Strain Rate Sensitivity

Strain rate sensitivity is an important property of the materials for describing its response under different loading conditions. The tensile experiments in Zircaloy-4 show that the strain rate sensitivity displays an “S” shape profile, where the curve is

flat at low and high temperatures, but stiffer at intermediate temperature (seen in Figure 5.4). However, there is no satisfied explanation yet to this non-trivial behavior. In contrast, the current constitutional model [155] is based on a pure fitting to experimental data and containing many parameters.

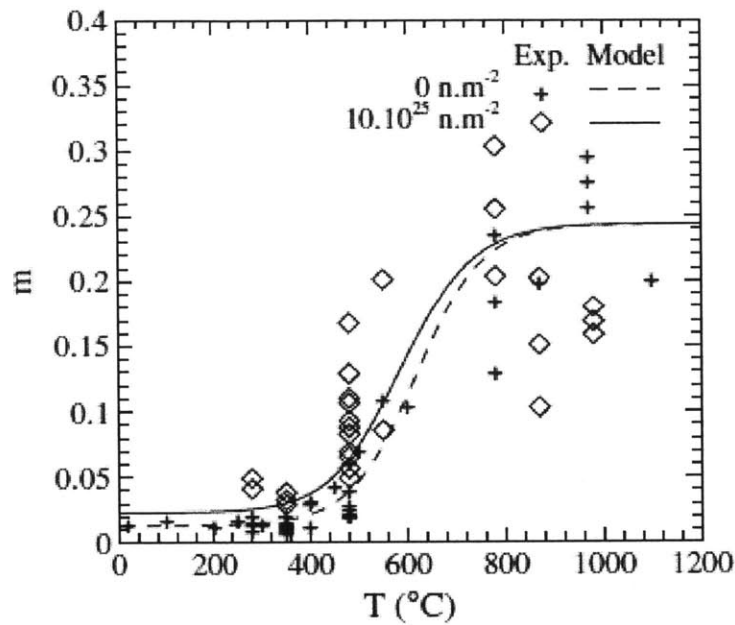


Figure 5.4 The measured strain rate sensitivity for Zircaloy-4, defined as  $m = \partial \ln \sigma / \partial \ln \dot{\epsilon}$ , at different temperatures. The plot is adapted from Ref.[155].

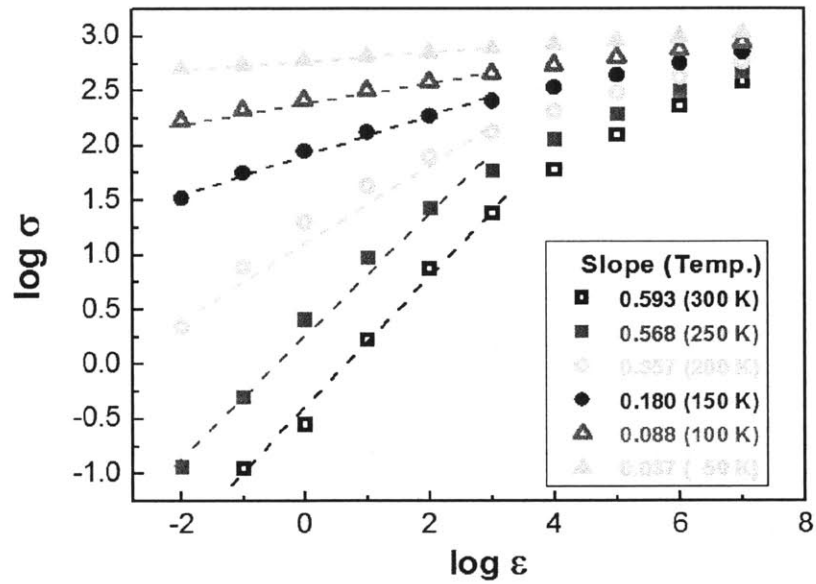
In this section, we would like to provide a physical based model to describe this “S” shape behavior in a simpler way. In Chapter 4, section 4.1, we derived an analytical expression (Eq.4.8) for the yield strength of the materials at prescribed temperatures and strain rates. Since the strain rate sensitivity is defined as  $m = \partial \ln \sigma / \partial \ln \dot{\epsilon}$ , the full information on strain rate sensitivity is actually included already in Eq.4.8.

Since there is no suitable interatomic potential yet for Zr, here we revisit the bcc Fe model system in section 4.1, as an illustrative example. In Figure 5.5 (a), we plot the relation between yield strength and applied strain rate at different temperatures, in a log-log scale. According to the definition of the strain rate sensitivity, the slopes of these curves thus represent the strain rate sensitivity. In previous constitutional

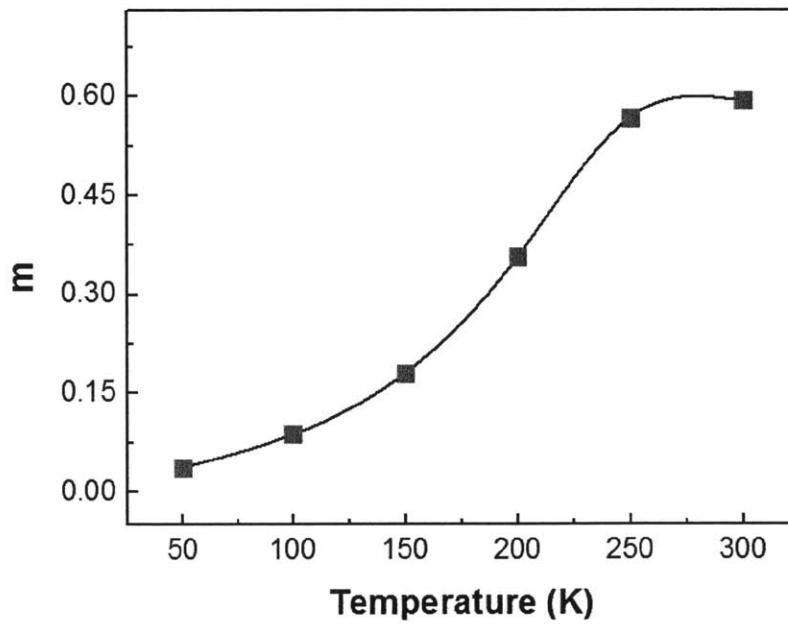
model [155],  $m$  is believed to be strain rate-independent. However in our results, the value of  $m$  is also changing as a function of applied strain rate. As seen in Figure 5.5 (a), the curves are bending down at the right end, indicating a smaller value at high strain rates. On the other hand, in the low strain rate regime (below  $10^3\text{s}^{-1}$ ), where the experiments have been done, the slopes are quasi-linear. We therefore fit the data points below  $10^3\text{s}^{-1}$  and read off the corresponding slopes at various temperatures. We then plot the slopes as a function of temperature, as shown by Figure 5.5 (b). It can be seen that, a natural “S” shape curve occurs in our model, which is qualitatively consistent with the experiments.

Admittedly, there are non-negligible quantitative discrepancies between the results in Figure 5.5 and the experiments. For example, in Figure 5.5 (b), the strain rate sensitivity starts to increase significantly at 150 K, while gets saturated above 250 K. While in experiments shown in Figure 5.4, the strain rate sensitivity does not increase until  $450^\circ\text{C}$  (723 K), and gets saturated around  $800^\circ\text{C}$  (1073 K). And there are several reasons for this quantitative discrepancy. At first, our simulated system is on bcc Fe, while the experiments are on Zircolay-4. Different materials will probably have quite different characteristic activation energy profiles  $E(\sigma)$ , which further induce such discrepancy. Secondly, in our modeling system, we are simulating a single dislocation glide in the pure metal, while the real experiments can have complicated microstructures and impurities, which again significantly affect the activation energy profiles  $E(\sigma)$  and lead to the quantitative inconsistency. So in order to have a more accurate description on the real materials, one requires a suitable interatomic potential, as well as the dominant unit process in real experiments.





(a)



(b)

Figure 5.5 (a) The relation between yield strength and applied strain rate in a log-log scale, at different temperature, in a Fe model system. (b) The strain rate sensitivity calculated from (a), as a function of temperature.

To summarize, we introduced two illustrative examples in this chapter, to demonstrate a constitutive framework for feeding the atomistic simulation results on dislocation-defect interactions into engineering scale model. We observed that, for the interaction between dislocation and vacancy cluster, both the interaction mechanisms and activation energies, and thus the climb rates, are significantly influenced by the applied stress. These derived parameters can be directly input into Eq.(5.4) in VPSC model, and therefore strengthen its accuracy from a fundamental level. We also provided a physical based description to the mesoscale constitutional model, and qualitatively explained the non-trivial “S” shape behavior for the strain rate sensitivity observed in experiments.

# Chapter 6

## Summary and Broad Implication

### 6.1 Summary of the Thesis

In this thesis, we have employed a newly adapted atomistic modeling technique to investigate the slow dynamics in microstructural evolution in irradiated nuclear structural materials. The aim has been understanding and predicting the material macroscopic degradation from a fundamental level. We particularly focused on the dislocation mobility and dislocation interaction with radiation induced defect clusters under different conditions of applied strain rates and temperatures. The problems tackled in this thesis are of great technological and scientific importance, because the materials mechanical properties, which are critical for the safety in the nuclear reactors, are largely controlled by the dislocation-obstacle interactions[24, 25, 44-47].

The first contribution in this thesis is to address the challenge of bridging a time scale gap more than ten orders of magnitude, from the intrinsic atomic scale (around  $10^{-12}$ s) to experimental scale (seconds or even years), which can never be accomplished by traditional atomistic simulation methods like molecular dynamics. This challenge is overcome by a combining a recently developed technique, the ABC method, with transition state theory calculations. ABC is rooted on the concept of exploring energy landscape. By analyzing how the defect microstructure evolves on the associated energy landscape, we are able to characterize the important unit processes. Correspondingly, the derived pathways and barriers are fed into TST, which enables to extend the analysis to arbitrarily long time scales while retaining the atomistic details. In this thesis, we extended the capabilities of the ABC method in two key areas. ABC is now made able to detect the multiple transition pathways

associated with the same given energy minimum state. This extension is especially useful in complex or anisotropic reactions, where only one pathway is not enough to accurately describe the kinetics of the system evolution. In order to study the dislocation-obstacle interactions at long time scales with a prescribed strain rate, we particularly made a dynamic generalization of ABC method. The new model consists of consecutive ABC iterations and TST to incorporate the strain rate effect. This framework is very general, and can be easily modified to incorporate other dynamic factors, e.g. the irradiation dose rate, temperature annealing rate, etc.

If the studies are performed only by ABC calculations, then the results are inherently limited to a set of discrete points, i.e. results obtained at a particular temperature and strain rate. Our second contribution in this thesis is to derive an analytical theory for describing the reaction mechanisms under different applied strain rate and temperature conditions. We explicitly demonstrated how the applied strain rate can affect the thermal activation, within the framework of transition state theory and informed by ABC. This theoretical generalization not only allows the investigation in an arbitrary range of strain rate and temperature, but it also provides a continuous quantitative identification of mechanism boundary in a two-parameter space consisting of strain rate and temperature.

Three key scientific contributions followed, enabled by the new approach described above. These all relate to properties of dislocations, and are explained by a common theory, that is the coupling of strain rate and thermal activation. First is the prediction of flow stresses in plastically deforming metals. Explaining and predicting the dislocation flow stress as a function of strain rate problem has been known as a formidable challenge in material science. The underlying mechanism for the experimentally observed flow stress upturn behavior at high strain rate has not been well clarified till this thesis. All existing models to date use adjustable parameters to connect the flow stress below and above the critical strain rate for upturn. In this thesis, we demonstrated that the coupling between strain rate and thermal activation leads naturally to the experimentally observed stress upturn at high strain rate, without invoking a different physical mechanism, or introducing any bridging

parameters. This parameter-free explanation of the transition from thermal- to stress-activation controlled regimes across a critical  $\dot{\epsilon}$  range matches quantitatively with experiments.

Our second scientific contribution is the derivation of the mechanism map for describing the boundaries between dislocation-obstacle interaction mechanisms as a function of strain rate, which was never possible to do prior to our work. We showed the interactions are determined by the competition between thermal activation and applied strain rate. Specifically, there are two distinct interaction mechanisms: (i) at high temperature and low applied strain rate, the SIA cluster is absorbed by the dislocation; (ii) at low temperature and high applied strain rate, the dislocation passes through the SIA cluster, leaving behind both the SIA cluster and the dislocation structures fully recovered. The derived interaction mechanism map can well explain the seeming controversy between experiments, where dislocation channels are observed, and previous molecular static simulation, where the defects get fully recovered. Since the two mechanisms have qualitatively different consequences to the mechanical properties, the derived mechanism map is therefore particularly important for predicting the materials microstructural evolution, and hence optimizing its performance under various environmental conditions. In addition, our mechanism map can provide useful guidance to MD simulations. For example, many MD studies at current stage intend to reveal the interaction mechanisms between dislocations and obstacles by doing the simulations only at one particular or very limited range of conditions (i.e. always at higher strain rates than  $10^6\text{s}^{-1}$ ) [7, 9, 10, 19, 20, 24, 25]. However, our derived mechanism map in this thesis shows that the MD results at limited conditions cannot always be extrapolated to low strain rates, and that it is necessary to directly simulate a wide range of environments in order to have a comprehensive understanding of their interaction mechanisms and the critical stresses.

Our third scientific contribution is providing a new, alternative explanation to the experimentally observed negative strain rate sensitivity (nSRS) phenomena from an atomistic point of view. Previous explanations to nSRS have been developed from

a macroscale point of view. Understanding and explaining the nSRS behavior are critical because it results in the decreased ductility and strength of the materials, and correspondingly generates the plastic instabilities of materials during deformation [48, 49]. In this thesis we examined a unit process of dislocation-vacancy cluster interaction in bcc Fe over a broad range of strain rates, and observed a nSRS behavior below the condition of  $10^5\text{s}^{-1}$ . We demonstrated that the critical resolved shear stress (CRSS) of the system is determined by the competitions between thermal activation and strain rate effect. Different strain rates can affect the microstructures of the defects during the interaction, and eventually lead to the “V” shape like relation between the CRSS and loaded strain rates. We showed that even a unit process can induce an inverse behavior as well, which supplements the previous explanations to the inverse relation from a global point of view.

In wrapping up the summary, we would like to offer a brief outlook beyond the current scope that so far has focused on the dislocation system. In fact as seen in Figure 6.1, by connecting the examples tackled in this thesis, we proposed a general workflow that can bridge the atomistic scale to the experimental scale. Connecting these two ends of the computational spectrum typically separated by many orders of magnitude difference in time scale has been a grand challenge in materials simulations. The ABC algorithm is the starting point, which allows one to identify the governing reaction pathways in the system evolution regardless of the extent of time scale. Then combined with the derived analytical theory, we can predict the response of these reactions at the unit process level to the surrounding environments. This approach transfers the underlying mechanism from fundamental level to engineering scale. This proposed workflow is quite general and is not limited to specific materials or reactions. It therefore can be applicable to many other important systems (e.g. colloids, cement) and phenomena (e.g. corrosion, creep) as well, and we would like to propose an analogy between the crystal plasticity and glass rheology in the following section.

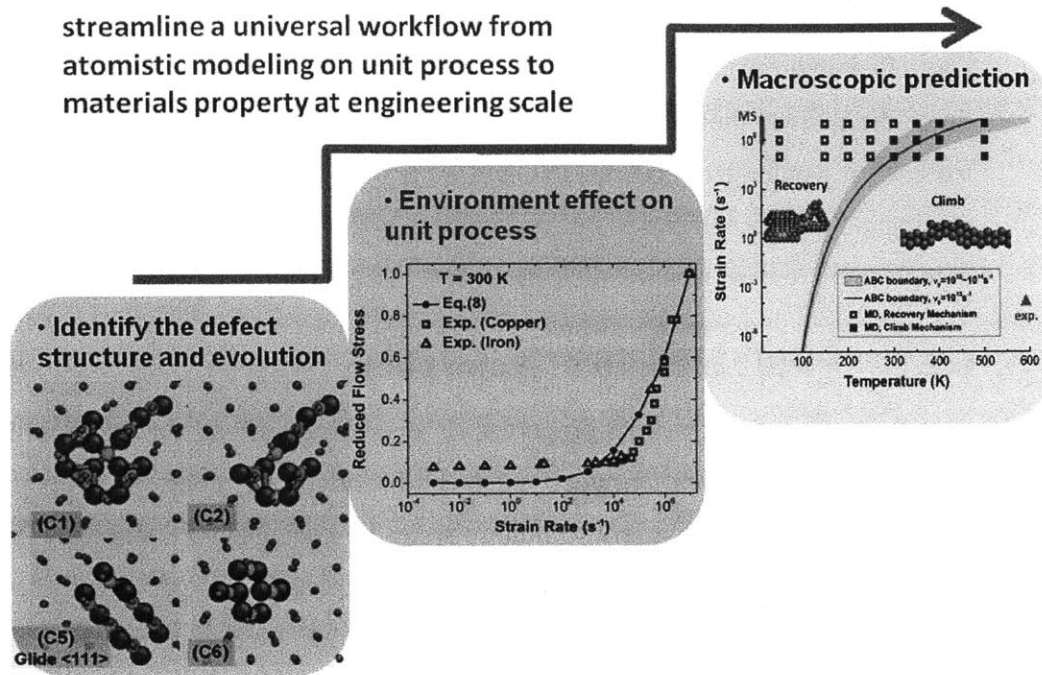


Figure 6.1 A schematic illustration of the general workflow built up in this thesis, from the atomistic modeling on unit process to predict materials properties at engineering scale.

## 6.2 Analogy between Glass Rheology and Crystal Plasticity

### 6.2.1 Background

Throughout this thesis, particularly in Chap 4, we demonstrated that the competition between thermal activation and applied strain rate is a common principle behind many important phenomena driven by time dependent conditions. In Sec 4.1, within the framework of transition state theory, we derive an analytical model which describes the variation of the plastic flow stress with temperature and strain rate. Given the stress-dependent activation barrier  $E(\sigma)$  for the dominant plastic unit (e.g.

the glide motion of screw dislocation in Sec 4.1), our model can provide a parameter-free explanation of the transition from thermal- to stress- activation controlled regimes across a critical  $\dot{\epsilon}$  range that matches well with experiments. Since the derived theory in Chap 4 is quite general and not limited by any specific material, it would be of considerable interest to test whether this model can also help understand the phenomena in other systems, e.g. the yield strength up-turn behavior at high strain rates in glassy solids, as we will discuss below.

## 6.2.2 Yield Strength of Amorphous System

The study of mechanical properties of amorphous system, *e.g.* its deformation and plasticity behaviors, has received much attention. To probe the properties of glassy system, it is convenient to impose a steady, homogenous shear flow into the system [156, 157]. It is therefore particularly important to study the mechanical response of the glassy system to the applied shear rate. Both experiments [158] and simulations [131, 159] have shown that, there exists a nonlinear relation between the flow stress and applied strain rate. For example, Figure 6.2 (a) shows the yield stress variation with strain rate observed in a colloidal suspension. Upon analysis the data are found to correlate with several stages of microstructural transitions, from single-crystal (SC) to polycrystal (PC) and to shearing layers (SL). As for the yield strength, it can be seen that the increase of shear stress is relatively slow at low strain rates, while becomes significant at high strain rates. In this section we focus on the stress up-turn seen at the strain rate around  $10^2 \text{ s}^{-1}$ . A corresponding yield response measured in a metal is given in Figure 6.2 (b). An even more pronounced stress increase sets in at the critical strain rate around  $10^4 \text{ s}^{-1}$ . It may seem the up-turn behavior could be a general response, common to amorphous and crystalline matter. One may then ask whether there is an equally general understanding of the underlying rate-dependent phenomena.



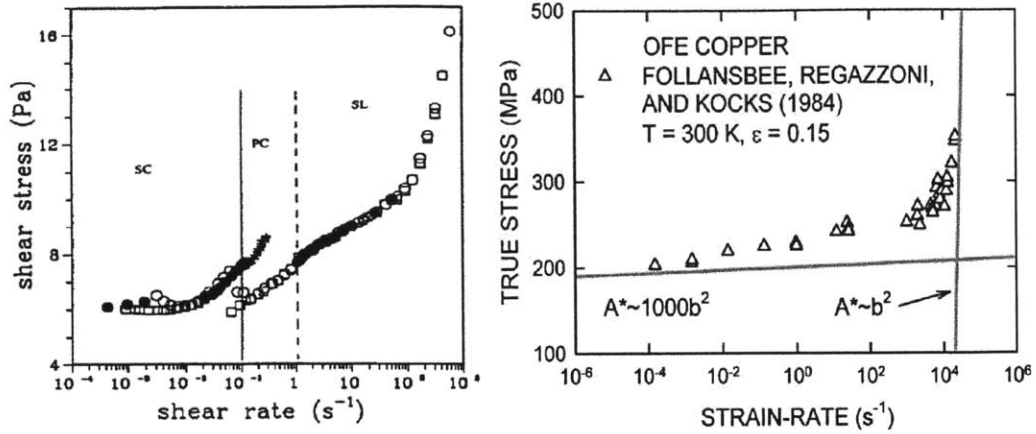


Figure 6.2 (a) Experimental data on a colloidal suspension showing a significant increase in the shear stress beyond a certain shear rate (adapted from [158]). (b) Measured flow stress in copper showing the up-turn behavior [38]. Two activation volumes corresponding to the low and high strain-rate regimes are indicated.

Several models have been proposed to describe the temperature and strain rate dependence of shear yielding in amorphous systems, such as the Eyring model[160], shear transformation zone (STZ) theory [161], and soft glassy rheology (SGR) model [162].

In Eyring model, the activation volume for the plastic unit is assumed to be a constant, *i.e.* its activation barrier changes linearly as the shear stress. Therefore the transition rate of plastic unit can be written as:

$$k = k_0 \exp\left[-\frac{E - \sigma V^*}{k_B T}\right] \quad (\text{Eq.6.1})$$

where  $k_0$  is the attempt frequency,  $E$  is the activation barrier,  $V^*$  is the activation volume,  $\sigma$  is the shear stress. Based on the assumption of constant transition rate, the relation between shear stress, applied strain rate and temperature can be expressed in a classical Arrhenius manner, as:

$$\sigma = \frac{E}{V^*} + \frac{k_B T}{V^*} \ln\left[\frac{\dot{\epsilon}}{\dot{\epsilon}_0}\right] \quad (\text{Eq.6.2})$$

where  $\dot{\epsilon}$  is the applied strain rate,  $\dot{\epsilon}_0$  is the reference strain rate. Therefore the Eyring model predicts a linear relation between the yield stress and logarithm of applied strain rate.

In STZ theory, different from the Eyring model, the transition rate of plastic unit is based on free-volume activation rather than thermal activation. Specifically, the transition rate is written in the form:

$$k = k_0 \exp\left[-\frac{v_0}{v_f}\right] \exp\left[\frac{\sigma}{\bar{\mu}}\right] \quad (\text{Eq.6.3})$$

where  $v_0$  is the characteristic free volume for a STZ rearrangement,  $v_f$  is a typical free volume per particle,  $\bar{\mu}$  is a typical stress scaling factor. After combining a creation and annihilation term of STZ that is coupled with the mean flow, STZ theory predicts a power law relation between the yield stress and applied strain rate.

In SGR model, similarly to STZ theory, the yield process is assumed to be activated by structure arrangement, rather than the temperature. In addition, the activation barrier of the yield process is assumed varying elastically. In particular, the transition rate for the yield process can thus be expressed as:

$$k = k_0 \exp\left[-\frac{E - \tau l^2 / 2}{x}\right] \quad (\text{Eq.6.4})$$

where  $\tau$  is the elastic constant,  $l$  is the local strain,  $x$  is the characteristic interactions between regions in a mean-field approximation. Similarly to STZ theory, a power law relation between the yield stress and applied strain rate is predicted in SGR model.

While each model mentioned above has merit, none can be regarded as satisfactory in providing underlying physical explanation of the yielding over the entire range of strain rates. Figure 6.3 shows MD simulations of supercooled binary liquids (80/20 LJ system) [131, 159]. In interpreting the results shown in Figure 6.3 (a), it is noted that at low strain rate, the yield stress varies linearly as logarithm of strain rate (indicated by the solid lines), as described by the Eyring model. However, at high strain rate one sees a more rapid increase, more like a power-law

behavior(dashed lines), as given by the STZ and SGR models[131]. In another MD study shear localization in the sense of shear-induced ordering was analyzed through a local intermediate scattering function [159]. The stress-strain rate flow curve, seen in Figure 6.3 (b) shows the observation of fluidized shear bands at low strain rates. With increasing strain rate the band grows thicker and then disappears. More recently, simulation studies have focused on the interplay of loading, thermal activation, and mechanical noise, clarifying the effects of temperature relative to athermal processes of avalanche dynamics [163]. Generally speaking while the up-turn behavior under discussion here is clearly known in glassy systems, its dynamical origin has not received much attention.

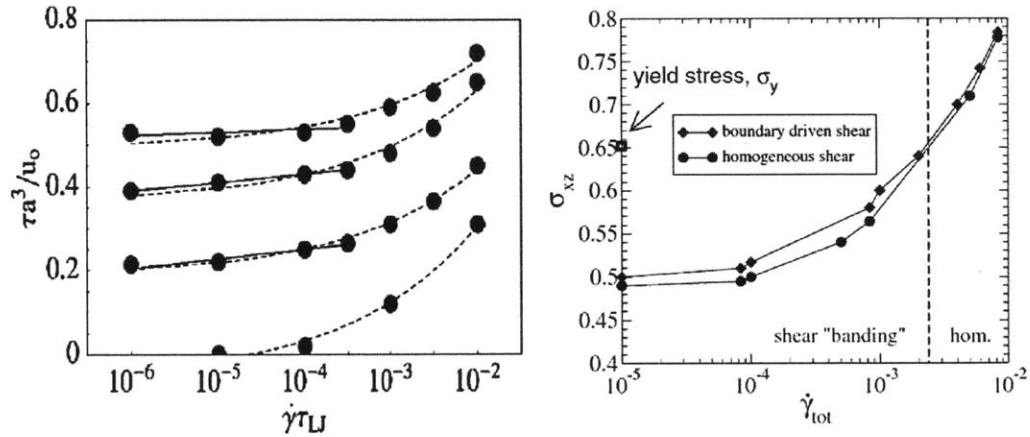


Figure 6.3 (a) Variation of yield stress with strain rate in supercooled liquids (adapted from [131]). solid lines indicate a linear relation between the stress and logarithm of the strain rate, while dashed lines are power-law fits. (b) Relation between yield stress and applied strain rate showing stress-induced shear bands at low strain rate (adapted from [159]).

### 6.2.3 Analogy between Amorphous and Crystal System

As introduced in Sec 4.1, experimental evidence of up-turn in yield response of metals is well established[38]. There is general agreement the essentially Arrhenius behavior at low strain rates is indicative of thermal activation. The underlying dislocation mechanism at the crossover and beyond, where a power-law behavior is indicated, is still a matter of interest. Such variations have been observed in a number of metals, including Fe, Ta, Cu, Al, and Zn[37]. The onset of non-Arrhenius

response has elicited the development of several empirical constitutive models which have been reviewed by Remington *et al.* [121]. Similar to the current views in glass rheology, most existing models do not offer a natural explanation for the onset of the up-turn behavior. Instead adjustable parameters are postulated to connect the flow stress behavior below and above the critical strain rate.

The similarity in yielding between glassy and crystalline systems can be examined at the atomistic level in terms of MD simulations of stress versus strain. As seen in Figure 6.4 after the initial elastic response, the shear stress undergoes small-scale fluctuations interrupted by a larger-magnitude relaxation event, reminiscent of stick-slip behavior. The intermittent discrete relaxation events in the crystal can be interpreted as activation of dislocation displacement, while in the glass they suggest activation (flip) of shear transformation [164], or free volume zones [165].

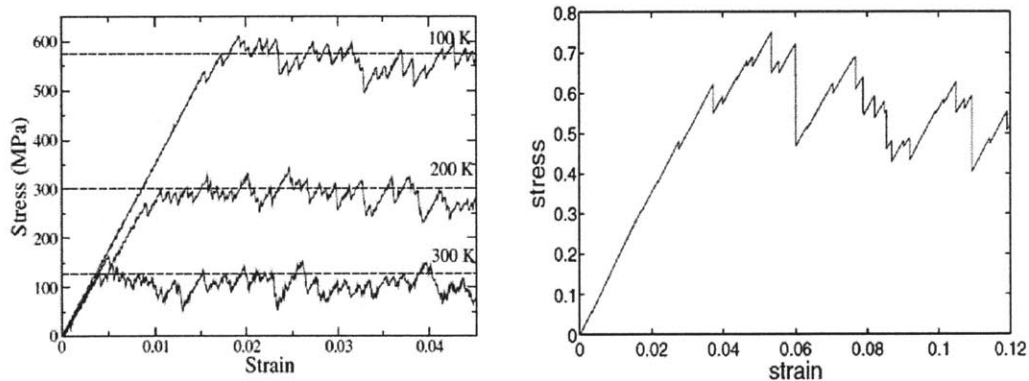


Figure 6.4 (a) MD simulation of stress-strain curves in single crystal Al containing a Lomer dislocation at several temperatures (adapted from [166]). (b) MD simulation results on a glassy system (adapted from [167]).

The similarity we have noted between glasses and metals which clearly have different microstructures suggests the upturn behavior may have a more fundamental origin that is not material specific. In Sec 4.1, we developed a constitutive model for the onset of plastic flow in crystals by introducing a stress-dependent activation barrier,  $E(\sigma)$ , a quantity that can be obtained separately by atomistic calculations [29]. The model is formulated in the framework of TST where the only mechanism

for plastic deformation considered is dislocation glide. For strain-rate controlled environments, where the system's strain and stress are time-dependent, the yield strength of the system is given by,

$$\bar{\sigma}_{flow} = \frac{\int_0^{\sigma_c} \sigma k^\perp(\sigma) \exp\left[-\frac{1}{G\dot{\epsilon}} \int_0^\sigma k^\perp(\sigma') d\sigma'\right] d\sigma}{\int_0^{\sigma_c} k^\perp(\sigma) \exp\left[-\frac{1}{G\dot{\epsilon}} \int_0^\sigma k^\perp(\sigma') d\sigma'\right] d\sigma}, \quad (k^\perp(\sigma) = k_0^\perp \exp\left[-\frac{E(\sigma)}{k_B T}\right])$$

(Eq.6.5)

where  $k^\perp(\sigma)$  is the transition rate which is determined by a stress-dependent (also time-dependent) activation barrier  $E(\sigma)$ ,  $G$  is the shear modulus, and  $\dot{\epsilon}$  is the applied strain rate. The only input to the model is  $E(\sigma)$ , a quantity that can be determined by atomistic calculations using an appropriate inter-atomic potential [29]. This model gives the flow stress behavior over the entire range of strain rates, without invoking any other dislocation interaction mechanism or introducing bridging parameters. As seen in Figure 4.3 (b), this model shows a natural transition from classical Arrhenius behavior of yielding, associated with thermally assisted relaxation, to a nonlinear behavior beyond the critical strain rate, which is very well consistent with experiments.

An analogous situation should hold for amorphous solids. Indeed the notion of a strain-dependent activation energy has been put forth recently in analyzing the temperature effects on the rheology [163], or equivalently elastoplasticity [167, 168], of glasses and dense colloidal suspensions. In particular, it has been proposed to couple the thermally activated plastic units with applied strain rate through a conditional probability [163],

$$P(\epsilon; \epsilon_0) = \exp\left[-\frac{1}{\dot{\epsilon}} \int_{\epsilon_0}^\epsilon k^{flip}(\epsilon') d\epsilon'\right] \quad (\text{Eq.6.6})$$

$$k^{flip}(\epsilon) \propto \exp\left[-\frac{E(\epsilon)}{k_B T}\right] \quad (\text{Eq.6.7})$$

where  $P(\epsilon; \epsilon_0)$  is the probability that the local zone does not flip at strain  $\epsilon$  given that the initial strain is  $\epsilon_0$ , and  $k^{flip}(\epsilon)$  is the transition rate for a zone flip at local strain  $\epsilon$ .

Comparing Eq.(6.5) and Eq.(6.6-6.7) shows that investigators in two communities which have not had much exchange thus far can benefit from an awareness of the broad significance of thermal and stress activation effects in plasticity. The fact that recent developments have led to the same formulation is not accidental. It suggests that the use of a transition rate in the stress-dependant (also time-dependant) form is a physically sound way of quantifying the effects of stress (or strain) on defect nucleation and mobility. It is effective in coupling thermal and mechanical effects. Also the simple form is convenient for numerical calculations. On the other hand, to our best knowledge, there has not yet been a universal accepted identification for the local shear transformation zone and its flipping activation energy profile  $E(\epsilon)$  shown in Eq.(6.7). In contrast, the current focus on  $E(\epsilon)$  is only limited in the vicinity near the saddle point, and its form follows an empirical asymptotic function [163, 167-169], rather than the directly atomistic calculation. Given the good consistency in crystal plasticity, it therefore would be of considerable interest to test whether the similar strategy can also shed light on the glassy system. Specifically, the plastic units in glassy system need to be identified first. Then the corresponding activation energies with respect to the system's stress need be calculated directly from atomistic simulation. These two required input can actually well capture by ABC method, because it has already some successful applications in amorphous system [40, 41, 79]. Given this strategy, together with the constitutional model as derived in Eq.(6.5-6.7), a quantitatively more accurate description on glass rheology could be anticipated.

## 6.2.4 Discussion and Broader Implications

Based on the analogy mentioned above, one can give a physical interpretation of the up-turn behavior which is intuitively consistent with what we have discussed. We believe the up-turn, seen clearly in Figure 6.2 can be regarded as strain localization

in the sense that at the critical strain rate a localized strain does not have enough time to propagate throughout the system. In other words, the onset of a rising stress signifies a kinetically trapped microstructure. Recall in Figure 6.2 (b) the experimental data suggests that beyond critical strain rate the “apparent” activation volume is reduced by three orders of magnitude. It is this confinement (localization) that characterizes the rate sensitivity. On the other hand, a very recent MD study of shear flow in supercooled liquids also emphasized the role of a critical strain rate in probing the atomic mechanisms governing strain propagation [170], which is in the same line with the concepts we discussed here.

In sum, it seems reasonable to regard the coupling between thermal activation and strain rate is the fundamental physical mechanism underlying the non-linear up-turn behavior. Our understanding of materials yielding should not be confined only to simple dislocation glide in crystal or STZ flips in amorphous solids. In fact, more complex microstructure features could be treated, and quite possibly these could lead to refinements that give us further insights into the dynamic sensitivity of yielding to microstructure details. In addition, the theory can be further developed to incorporate other effects on the thermal activation than the applied strain rate. For example, other conditions (e.g. temperature annealing rate, irradiation rate, etc) can be similarly treated within the framework of Eq.(6.5-6.7), as long as those control parameters are time-dependant. With such development, we believe that this model can be applied to study broader materials and phenomena under various environments, beyond the current scope of this thesis.

# Bibliography:

1. Grimes, R.W., R.J. Konings, and L. Edwards, *Greater tolerance for nuclear materials*. Nature Materials, 2008. 7(9): p. 683-5.
2. Hill, D.J., *Nuclear energy for the future*. Nature Materials, 2008. 7(9): p. 680-682.
3. Stan, M., *Discovery and design of nuclear fuels*. Materials Today, 2009. 12(11): p. 20-28.
4. Grimes, R.W. and W.J. Nuttall, *Generating the Option of a Two-Stage Nuclear Renaissance*. Science, 2010. 329(5993): p. 799-803.
5. Zinkle, S.J. and G.S. Was, *Materials challenges in nuclear energy*. Acta Materialia, 2013. 61(3): p. 735-758.
6. Terentyev, D.A., Y.N. Osetsky, and D.J. Bacon, *Effects of temperature on structure and mobility of the  $\langle 100 \rangle$  edge dislocation in body-centred cubic iron*. Acta Materialia, 2010. 58(7): p. 2477-2482.
7. Terentyev, D., Y.N. Osetsky, and D.J. Bacon, *Competing processes in reactions between an edge dislocation and dislocation loops in a body-centred cubic metal*. Scripta Materialia, 2010. 62(9): p. 697-700.
8. Rong, Z., Y.N. Osetsky †, and D.J. Bacon \*, *A model for the dynamics of loop drag by a gliding dislocation*. Philosophical Magazine, 2005. 85(14): p. 1473-1493.
9. Bacon, D.J., Y.N. Osetsky, and Z. Rong, *Computer simulation of reactions between an edge dislocation and glissile self-interstitial clusters in iron*. Philosophical Magazine, 2006. 86(25-26): p. 3921-3936.



10. Terentyev, D., P. Grammatikopoulos, D.J. Bacon, and Y.N. Osetsky, *Simulation of the interaction between an edge dislocation and a  $\langle 1\ 0\ 0 \rangle$  interstitial dislocation loop in  $\alpha$ -iron*. *Acta Materialia*, 2008. **56**(18): p. 5034-5046.
11. Mansur, L.K., *Theory and experimental background on dimensional changes in irradiated alloys*. *Journal of Nuclear Materials*, 1994. **216**: p. 97-123.
12. Was, G.S., *Materials degradation in fission reactors: Lessons learned of relevance to fusion reactor systems*. *Journal of Nuclear Materials*, 2007. **367-370**(Part 1): p. 11-20.
13. Odette, G.R., M.J. Alinger, and B.D. Wirth, *Recent developments in irradiation-resistant steels*. *Annual Review of Materials Research*, 2008. **38**: p. 471-503.
14. Gelles, D.S., *Void swelling in binary FeCr alloys at 200 dpa*. *Journal of Nuclear Materials*, 1995. **225**(0): p. 163-174.
15. Katoh, Y., A. Kohyama, and D.S. Gelles, *Swelling and dislocation evolution in simple ferritic alloys irradiated to high fluence in FFTF/MOTA*. *Journal of Nuclear Materials*, 1995. **225**(0): p. 154-162.
16. Konobeev, Y.V., A.M. Dvoriashin, S.I. Porollo, and F.A. Garner, *Swelling and microstructure of pure Fe and Fe-Cr alloys after neutron irradiation to ~26 dpa at 400 °C*. *Journal of Nuclear Materials*, 2006. **355**(1-3): p. 124-130.
17. de Koning, M., A. Antonelli, and S. Yip, *Single-simulation determination of phase boundaries: A dynamic Clausius-Clapeyron integration method*. *The Journal of Chemical Physics*, 2001. **115**(24): p. 11025-11035.
18. Yip, S., *Synergistic science*. *Nature Materials*, 2003. **2**(1): p. 3-5.

19. Terentyev, D., L. Malerba, D.J. Bacon, and N.O. Yu, *The effect of temperature and strain rate on the interaction between an edge dislocation and an interstitial dislocation loop in  $\alpha$ -iron*. Journal of Physics: Condensed Matter, 2007. **19**(45): p. 456211.
20. Bacon, D.J., Y.N. Osetsky, and D. Rodney, *Chapter 88 Dislocation–Obstacle Interactions at the Atomic Level*, in *Dislocations in Solids*, J.P. Hirth and L. Kubin, Editors. 2009, Elsevier. p. 1-90.
21. Hatano, T. and H. Matsui, *Molecular dynamics investigation of dislocation pinning by a nanovoid in copper*. Physical Review B, 2005. **72**(9): p. 094105.
22. Hatano, T., *Dynamics of a dislocation bypassing an impenetrable precipitate: The Hirsch mechanism revisited*. Physical Review B, 2006. **74**(2): p. 020102.
23. Monnet, G., *Mechanical and energetical analysis of molecular dynamics simulations of dislocation–defect interactions*. Acta Materialia, 2007. **55**(15): p. 5081-5088.
24. Voskoboinikov, R.E., Y.N. Osetsky, and D.J. Bacon, *Interaction of edge dislocation with point defect clusters created in displacement cascades in  $\alpha$ -zirconium*. Materials Science and Engineering: A, 2005. **400–401**(0): p. 49-53.
25. Voskoboynikov, R.E., Y.N. Osetsky, and D.J. Bacon, *Self-interstitial atom clusters as obstacles to glide of edge dislocations in  $\alpha$ -zirconium*. Materials Science and Engineering: A, 2005. **400–401**(0): p. 54-58.
26. Dutta, A., M. Bhattacharya, N. Gayathri, G.C. Das, and P. Barat, *The mechanism of climb in dislocation–nanovoid interaction*. Acta Materialia, 2012. **60**(9): p. 3789-3798.
27. Weinberger, C.R., A.T. Jennings, K. Kang, and J.R. Greer, *Atomistic simulations and continuum modeling of dislocation nucleation and strength*

- in gold nanowires*. Journal of the Mechanics and Physics of Solids, 2012. **60**(1): p. 84-103.
28. Zhu, T., J. Li, A. Samanta, A. Leach, and K. Gall, *Temperature and strain-rate dependence of surface dislocation nucleation*. Physical Review Letters, 2008. **100**(2).
  29. Fan, Y., Y.N. Osetsky, S. Yip, and B. Yildiz, *Onset Mechanism of Strain-Rate-Induced Flow Stress Upturn*. Physical Review Letters, 2012. **109**(13): p. 135503.
  30. Onimus, F., I. Monnet, J.L. Béchade, C. Prioul, and P. Pilvin, *A statistical TEM investigation of dislocation channeling mechanism in neutron irradiated zirconium alloys*. Journal of Nuclear Materials, 2004. **328**(2-3): p. 165-179.
  31. Fan, Y., Y.N. Osetsky, S. Yip, and B. Yildiz, to be submitted.
  32. Ferguson, W.G., F.E. Hauser, and J.E. Dorn, *Dislocation damping in zinc single crystals*. British Journal of Applied Physics, 1967. **18**(4): p. 411.
  33. Kumar, A., F.E. Hauser, and J.E. Dorn, *Viscous drag on dislocations in aluminum at high strain rates*. Acta Metallurgica, 1968. **16**(9): p. 1189-1197.
  34. Campbell, J.D. and W.G. Ferguson, *The temperature and strain-rate dependence of the shear strength of mild steel*. Philosophical Magazine, 1970. **21**(169): p. 63-82.
  35. Hoge, K.G. and A.K. Mukherjee, *The temperature and strain rate dependence of the flow stress of tantalum*. Journal of Materials Science, 1977. **12**(8): p. 1666-1672.

36. Follansbee, P.S., G. Regazzoni, and U.F. Kocks, in *Mechanical Properties of Materials at High Strain Rates*, J. Harding, Editor. 1984, Institute of Physics: London. p. 71.
37. Regazzoni, G., U.F. Kocks, and P.S. Follansbee, *Dislocation kinetics at high strain rates*. *Acta Metallurgica*, 1987. **35**(12): p. 2865-2875.
38. Armstrong, R.W., W. Arnold, and F.J. Zerilli, *Dislocation mechanics of copper and iron in high rate deformation tests*. *Journal of Applied Physics*, 2009. **105**(2): p. 023511-7.
39. Fan, Y., A. Kushima, S. Yip, and B. Yildiz, in preparation.
40. Kushima, A., X. Lin, J. Li, J. Eapen, J.C. Mauro, X. Qian, P. Diep, and S. Yip, *Computing the viscosity of supercooled liquids*. *The Journal of Chemical Physics*, 2009. **130**(22): p. 224504-12.
41. Kushima, A., X. Lin, J. Li, X. Qian, J. Eapen, J.C. Mauro, P. Diep, and S. Yip, *Computing the viscosity of supercooled liquids. II. Silica and strong-fragile crossover behavior*. *The Journal of Chemical Physics*, 2009. **131**(16): p. 164505-9.
42. Ishii, A., S. Ogata, H. Kimizuka, and J. Li, *Adaptive-boost molecular dynamics simulation of carbon diffusion in iron*. *Physical Review B*, 2012. **85**(6): p. 064303.
43. Sorensen, M.R. and A.F. Voter, *Temperature-accelerated dynamics for simulation of infrequent events*. *Journal of Chemical Physics*, 2000. **112**(21): p. 9599-9606.
44. Griffiths, M., *A review of microstructure evolution in zirconium alloys during irradiation*. *Journal of Nuclear Materials*, 1988. **159**(0): p. 190-218.

45. Griffiths, M., *Evolution of microstructure in hcp metals during irradiation*. Journal of Nuclear Materials, 1993. **205**(0): p. 225-241.
46. Hayes, T., M. Kassner, and R. Rosen, *Steady-state creep of  $\alpha$ -zirconium at temperatures up to 850 °C*. Metallurgical and Materials Transactions A, 2002. **33**(2): p. 337-343.
47. Hayes, T. and M. Kassner, *Creep of zirconium and zirconium alloys*. Metallurgical and Materials Transactions A, 2006. **37**(8): p. 2389-2396.
48. Curtin, W.A., D.L. Olmsted, and L.G. Hector, *A predictive mechanism for dynamic strain ageing in aluminium-magnesium alloys*. Nature Materials, 2006. **5**(11): p. 875-880.
49. Robinson, J.M. and M.P. Shaw, *Microstructural and mechanical influences on dynamic strain aging phenomena*. International Materials Reviews, 1994. **39**(3): p. 113-122.
50. Turner, P.A., C.N. Tomé, N. Christodoulou, and C.H. Woo, *A self-consistent model for polycrystals undergoing simultaneous irradiation and thermal creep*. Philosophical Magazine A, 1999. **79**(10): p. 2505-2524.
51. Tomé, C.N. and N. Christodoulou, *Analysis of accelerated irradiation growth in Zr-2.5% Nb pressure tubes*. Philosophical Magazine A, 2000. **80**(6): p. 1407-1424.
52. Lebensohn, R.A., C.S. Hartley, C.N. Tomé, and O. Castelnau, *Modeling the mechanical response of polycrystals deforming by climb and glide*. Philosophical Magazine, 2010. **90**(5): p. 567-583.
53. Sastry, S., P.G. Debenedetti, and F.H. Stillinger, *Signatures of distinct dynamical regimes in the energy landscape of a glass-forming liquid*. Nature, 1998. **393**(6685): p. 554-557.

54. Barkema, G.T. and N. Mousseau, *Event-based relaxation of continuous disordered systems*. Physical Review Letters, 1996. **77**(21): p. 4358-4361.
55. Cances, E., F. Legoll, M.C. Marinica, K. Minoukadeh, and F. Willaime, *Some improvements of the activation-relaxation technique method for finding transition pathways on potential energy surfaces*. Journal of Chemical Physics, 2009. **130**(11): p. -.
56. Béland, L.K., P. Brommer, F. El-Mellouhi, J.-F. Joly, and N. Mousseau, *Kinetic activation-relaxation technique*. Physical Review E, 2011. **84**(4): p. 046704.
57. Kallel, H., N. Mousseau, and F. Schiettekatte, *Evolution of the Potential-Energy Surface of Amorphous Silicon*. Physical Review Letters, 2010. **105**(4): p. -.
58. Rodney, D. and C. Schuh, *Distribution of Thermally Activated Plastic Events in a Flowing Glass*. Physical Review Letters, 2009. **102**(23): p. 235503.
59. Henkelman, G. and H. Jonsson, *A dimer method for finding saddle points on high dimensional potential surfaces using only first derivatives*. The Journal of Chemical Physics, 1999. **111**(15): p. 7010-7022.
60. Heyden, A., A.T. Bell, and F.J. Keil, *Efficient methods for finding transition states in chemical reactions: Comparison of improved dimer method and partitioned rational function optimization method*. The Journal of Chemical Physics, 2005. **123**(22): p. 224101-14.
61. Xu, H., Y.N. Osetsky, and R.E. Stoller, *Simulating complex atomistic processes: On-the-fly kinetic Monte Carlo scheme with selective active volumes*. Physical Review B, 2011. **84**(13): p. 132103.

62. Haixuan, X., N.O. Yuri, and E.S. Roger, *Self-evolving atomistic kinetic Monte Carlo: fundamentals and applications*. Journal of Physics: Condensed Matter, 2012. **24**(37): p. 375402.
63. Xu, H., Y.N. Osetsky, and R.E. Stoller, *Cascade annealing simulations of bcc iron using object kinetic Monte Carlo*. Journal of Nuclear Materials, 2012. **423**(1–3): p. 102-109.
64. Voter, A.F., *A method for accelerating the molecular dynamics simulation of infrequent events*. The Journal of Chemical Physics, 1997. **106**(11): p. 4665-4677.
65. Wang, J.C., S. Pal, and K.A. Fichthorn, *Accelerated molecular dynamics of rare events using the local boost method*. Physical Review B, 2001. **6308**(8): p. -.
66. Montalenti, F. and A.F. Voter, *Applying Accelerated Molecular Dynamics to Crystal Growth*. physica status solidi (b), 2001. **226**(1): p. 21-27.
67. Bai, X.M., A.F. Voter, R.G. Hoagland, M. Nastasi, and B.P. Uberuaga, *Efficient Annealing of Radiation Damage Near Grain Boundaries via Interstitial Emission*. Science, 2010. **327**(5973): p. 1631-1634.
68. Laio, A. and M. Parrinello, *Escaping free-energy minima*. Proc Natl Acad Sci U S A, 2002. **99**(20): p. 12562-6.
69. Henkelman, G. and H. Jonsson, *Improved tangent estimate in the nudged elastic band method for finding minimum energy paths and saddle points*. The Journal of Chemical Physics, 2000. **113**(22): p. 9978-9985.
70. Rodney, D. and C.A. Schuh, *Yield stress in metallic glasses: The jamming-unjamming transition studied through Monte Carlo simulations based on the activation-relaxation technique*. Physical Review B, 2009. **80**(18): p. 184203.

71. Rodney, D. and T. Schröder, *On the potential energy landscape of supercooled liquids and glasses*. The European Physical Journal E, 2011. **34**(9): p. 1-7.
72. Mousseau, N., L.K. Béland, P. Brommer, J.-F. Joly, F. El-Mellouhi, E. Machado-Charry, M.-C. Marinica, and P. Pochet, *The Activation-Relaxation Technique: ART Nouveau and Kinetic ART*. Journal of Atomic, Molecular, and Optical Physics, 2012. **2012**: p. 14.
73. Wang, H., D.S. Xu, D. Rodney, P. Veyssière, and R. Yang, *Atomistic investigation of the annihilation of non-screw dislocation dipoles in Al, Cu, Ni and  $\gamma$ -TiAl*. Modelling and Simulation in Materials Science and Engineering, 2013. **21**(2): p. 025002.
74. Voter, A.F., F. Montalenti, and T.C. Germann, *EXTENDING THE TIME SCALE IN ATOMISTIC SIMULATION OF MATERIALS*. Annual Review of Materials Research, 2002. **32**(1): p. 321-346.
75. Hara, S. and J. Li, *Adaptive strain-boost hyperdynamics simulations of stress-driven atomic processes*. Physical Review B, 2010. **82**(18): p. 184114.
76. Fan, Y., A. Kushima, and B. Yildiz, *Unfaulting mechanism of trapped self-interstitial atom clusters in bcc Fe: A kinetic study based on the potential energy landscape*. Physical Review B, 2010. **81**(10): p. 104102.
77. Wang, H., D. Rodney, D. Xu, R. Yang, and P. Veyssière, *Pentavacancy as the key nucleus for vacancy clustering in aluminum*. Physical Review B, 2011. **84**(22): p. 220103.
78. Lau, T.T., A. Kushima, and S. Yip, *Atomistic Simulation of Creep in a Nanocrystal*. Physical Review Letters, 2010. **104**(17): p. 175501.



79. Li, J., A. Kushima, J. Eapen, X. Lin, X. Qian, J.C. Mauro, P. Diep, and S. Yip, *Computing the Viscosity of Supercooled Liquids: Markov Network Model*. PLoS ONE, 2011. **6**(3): p. e17909.
80. Brommer, P. and N. Mousseau, *Comment on "Mechanism of Void Nucleation and Growth in bcc Fe: Atomistic Simulations at Experimental Time Scales"*. Physical Review Letters, 2012. **108**(21): p. 219601.
81. Fan, Y., A. Kushima, S. Yip, and B. Yildiz, *Mechanism of Void Nucleation and Growth in bcc Fe: Atomistic Simulations at Experimental Time Scales*. Physical Review Letters, 2011. **106**(12): p. 125501.
82. Fan, Y., A. Kushima, S. Yip, and B. Yildiz, *Fan et al. Reply*. Physical Review Letters, 2012. **108**(21): p. 219602.
83. Voter, A.F., *Introduction to the kinetic Monte Carlo method*, in *Radiation Effects in Solids* K.E. Sickafus, E.A. Kotomin, and B.P. Uberuaga, Editors. 2007, Springer: Berlin. p. 1~24.
84. Osetsky, Y.N. and D.J. Bacon, *An atomic-level model for studying the dynamics of edge dislocations in metals*. Modelling and Simulation in Materials Science and Engineering, 2003. **11**(4): p. 427.
85. Wirth, B.D., G.R. Odette, D. Maroudas, and G.E. Lucas, *Energetics of formation and migration of self-interstitials and self-interstitial clusters in  $\alpha$ -iron*. Journal of Nuclear Materials, 1997. **244**(3): p. 185-194.
86. Soneda, N. and T. Diaz de La Rubia, *Migration kinetics of the self-interstitial atom and its clusters in bcc Fe*. Philosophical Magazine A, 2001. **81**(2): p. 331-343.
87. Osetsky, Y.N., D.J. Bacon, A. Serra, B.N. Singh, and S.I. Golubov, *One-dimensional atomic transport by clusters of self-interstitial atoms in iron and copper*. Philosophical Magazine, 2003. **83**(1): p. 61-91.

88. Marian, J., B.D. Wirth, A. Caro, B. Sadigh, G.R. Odette, J.M. Perlado, and T. Diaz de la Rubia, *Dynamics of self-interstitial cluster migration in pure  $\alpha$ -Fe and Fe-Cu alloys*. Physical Review B, 2002. **65**(14): p. 144102.
89. Takahashi, A. and N.M. Ghoniem, *Structure of self-interstitial atom clusters in iron and copper*. Physical Review B, 2009. **80**(17): p. 174104.
90. Arakawa, K., M. Hatanaka, E. Kuramoto, K. Ono, and H. Mori, *Changes in the Burgers Vector of Perfect Dislocation Loops without Contact with the External Dislocations*. Physical Review Letters, 2006. **96**(12): p. 125506.
91. Fu, C.C., J. Dalla Torre, F. Willaime, J.L. Bocquet, and A. Barbu, *Multiscale modelling of defect kinetics in irradiated iron*. Nature Materials, 2005. **4**(1): p. 68-74.
92. Takaki, S., J. Fuss, H. Kugler, U. Dedek, and H. Schultz, Radiat. Eff., 1983. **79**: p. 87.
93. Terentyev, D.A., T.P.C. Klaver, P. Olsson, M.C. Marinica, F. Willaime, C. Domain, and L. Malerba, *Self-Trapped Interstitial-Type Defects in Iron*. Physical Review Letters, 2008. **100**(14): p. 145503.
94. Ackland, G.J., M.I. Mendeleev, D.J. Srolovitz, S. Han, and A.V. Barashev, *Development of an interatomic potential for phosphorus impurities in alpha-iron*. Journal of Physics-Condensed Matter, 2004. **16**(27): p. S2629-S2642.
95. Domain, C. and C.S. Becquart, *Ab initio calculations of defects in Fe and dilute Fe-Cu alloys*. Physical Review B, 2001. **65**(2): p. 024103.
96. Fu, C.-C., F. Willaime, and P. Ordejón, *Stability and Mobility of Mono- and Di-Interstitials in  $\alpha$ -Fe*. Physical Review Letters, 2004. **92**(17): p. 175503.
97. Ju, L., *AtomEye: an efficient atomistic configuration viewer*. Modelling and Simulation in Materials Science and Engineering, 2003. **11**(2): p. 173.

98. Schilling, W., P. Ehrhart, and K. Sonnenberg. *Interpretation of defect reactions in irradiated metals by the one interstitial model*. in *Fundamental Aspects of Radiation Damage in Metals, Vol. I, CONF-751006-P1*. (1975. Oak Ridge, Tenn.
99. Nikolaev, A.L., V.L. Arbuzov, and A.E. Davletshin, *On the effect of impurities on resistivity recovery, short-range ordering, and defect migration in electron-irradiated concentrated Fe-Cr alloys*. *Journal of Physics-Condensed Matter*, 1997. **9**(21): p. 4385-4402.
100. Eldrup, M. and B.N. Singh, *Accumulation of point defects and their complexes in irradiated metals as studied by the use of positron annihilation spectroscopy - a brief review*. *Journal of Nuclear Materials*, 2003. **323**(2-3): p. 346-353.
101. Puska, M.J. and R.M. Nieminen, *Defect Spectroscopy with Positrons - a General Computational Method*. *Journal of Physics F-Metal Physics*, 1983. **13**(2): p. 333-346.
102. Arponen, J. and E. Pajanne, *Electron Liquid in Collective Description .3. Positron-Annihilation*. *Annals of Physics*, 1979. **121**(1-2): p. 343-389.
103. Gupta, R.P. and R.W. Siegel, *Positron Trapping and Annihilation at Vacancies in Bcc Refractory-Metals*. *Journal of Physics F-Metal Physics*, 1980. **10**(1): p. L7-L13.
104. Glade, S.C., B.D. Wirht, G.R. Odettes, P. Asoka-Kumar, P.A. Sterne, and R.H. Howell, *Positron annihilation spectroscopy and small-angle neutron scattering characterization of the effect of Mn on the nanostructural features formed in irradiated Fe-Cu-Mn alloys*. *Philosophical Magazine*, 2005. **85**(4-7): p. 629-639.

105. Bacon, D.J., Y.N. Osetsky, R. Stoller, and R.E. Voskoboinikov, *MD description of damage production in displacement cascades in copper and [alpha]-iron*. Journal of Nuclear Materials, 2003. **323**(2-3): p. 152-162.
106. Balluffi, R.W., S.M. Allen, W.C. Carter, and R.A. Kemper, *Kinetics of materials*. 2005, Hoboken, N.J.: J. Wiley & Sons. xxvi, 645 p.
107. Terentyev, D., C. Lagerstedt, P. Olsson, K. Nordlund, J. Wallenius, C.S. Becquart, and L. Malerba, *Effect of the interatomic potential on the features of displacement cascades in [alpha]-Fe: A molecular dynamics study*. Journal of Nuclear Materials, 2006. **351**(1-3): p. 65-77.
108. Lau, T.T., C.J. Forst, X. Lin, J.D. Gale, S. Yip, and K.J. Van Vliet, *Many-body potential for point defect clusters in Fe-C alloys*. Phys Rev Lett, 2007. **98**(21): p. 215501.
109. Monasterio, P.R., T.T. Lau, S. Yip, and K.J. Van Vliet, *Hydrogen-vacancy interactions in Fe-C alloys*. Phys Rev Lett, 2009. **103**(8): p. 085501.
110. Mendeleev, M.I. and G.J. Ackland, *Development of an interatomic potential for the simulation of phase transformations in zirconium*. Philosophical Magazine Letters, 2007. **87**(5): p. 349-359.
111. Osetsky, Y., D. Bacon, and N. de Diego, *Anisotropy of point defect diffusion in alpha-zirconium*. Metallurgical and Materials Transactions A, 2002. **33**(13): p. 777-782.
112. Ackland, G.J., S.J. Wooding, and D.J. Bacon, *Defect, surface and displacement-threshold properties of alpha-zirconium simulated with a many-body potential*. Philosophical Magazine A, 1995. **71**(3): p. 553-565.
113. Khater, H.A. and D.J. Bacon, *Dislocation core structure and dynamics in two atomic models of alpha-zirconium*. Acta Materialia, 2010. **58**(8): p. 2978-2987.

114. Subramanian, G. and C.N. Tomé, *Progress report on the incorporation of lower lengthscales into polycrystal plasticity models*. Technical Report, 2012. **LA-UR-12-25612**.
115. Deng, C. and C.A. Schuh, *Atomistic Simulation of Slow Grain Boundary Motion*. Physical Review Letters, 2011. **106**(4): p. 045503.
116. Johnson, G.R., J.M. Hoegfeldt, U.S. Lindholm, and A. Nagy, *Response of Various Metals to Large Torsional Strains Over a Large Range of Strain Rates---Part 1: Ductile Metals*. Journal of Engineering Materials and Technology, 1983. **105**(1): p. 42-47.
117. Zerilli, F.J. and R.W. Armstrong, *Dislocation-mechanics-based constitutive relations for material dynamics calculations*. Journal of Applied Physics, 1987. **61**(5): p. 1816-1825.
118. Follansbee, P.S. and U.F. Kocks, *A constitutive description of the deformation of copper based on the use of the mechanical threshold stress as an internal state variable*. Acta Metallurgica, 1988. **36**(1): p. 81-93.
119. Steinberg, D.J. and C.M. Lund, *A constitutive model for strain rates from  $10^{sup - 4}$  to  $10^{sup 6}$  s $^{sup - 1}$* . Journal of Applied Physics, 1989. **65**(4): p. 1528-1533.
120. Preston, D.L., D.L. Tonks, and D.C. Wallace, *Model of plastic deformation for extreme loading conditions*. Journal of Applied Physics, 2003. **93**(1): p. 211-220.
121. Remington, B.A., P. Allen, E.M. Bringa, J. Hawreliak, D. Ho, K.T. Lorenz, H. Lorenzana, J.M. McNaney, M.A. Meyers, S.W. Pollaine, K. Rosolankova, B. Sadik, M.S. Schneider, D. Swift, J. Wark, and B. Yaakobi, *Material dynamics under extreme conditions of pressure and strain rate*. Materials Science and Technology, 2006. **22**(4): p. 474-488.

122. Armstrong, R.W., *Relation between the Peetch "friction" stress and the thermal activation rate equation*. Acta Metallurgica, 1967. **15**(4): p. 667-668.
123. Kocks, U.F., A.S. Argon, and M.F. Ashby, in *Progress in Materials Science*, B. Chalmers, J.W. Christian, and T.B. Massalski, Editors. 1975, Pergamon Press: New York. p. 110.
124. Rodney, D. and L. Proville, *Kink-pair nucleation on dislocations under stress in the two-dimensional Frenkel-Kontorova model*. Physical Review B, 2008. **78**(10): p. 104115.
125. Rodney, D. and L. Proville, *Stress-dependent Peierls potential: Influence on kink-pair activation*. Physical Review B, 2009. **79**(9): p. 094108.
126. Domain, C. and G. Monnet, *Simulation of Screw Dislocation Motion in Iron by Molecular Dynamics Simulations*. Physical Review Letters, 2005. **95**(21): p. 215506.
127. Gordon, P.A., T. Neeraj, Y. Li, and J. Li, *Screw dislocation mobility in BCC metals: the role of the compact core on double-kink nucleation*. Modelling and Simulation in Materials Science and Engineering, 2010. **18**(8): p. 085008.
128. Mendeleev, M.I., S. Han, D.J. Srolovitz, G.J. Ackland, D.Y. Sun, and M. Asta, *Development of new interatomic potentials appropriate for crystalline and liquid iron*. Philosophical Magazine, 2003. **83**(35): p. 3977-3994.
129. Terentyev, D., G. Bonny, C. Domain, and R.C. Pasianot, *Interaction of a  $1/2\{111\}$  screw dislocation with Cr precipitates in bcc Fe studied by molecular dynamics*. Physical Review B, 2010. **81**(21): p. 214106.
130. Angell, C.A., *Perspective on the glass transition*. Journal of Physics and Chemistry of Solids, 1988. **49**(8): p. 863-871.

131. Rottler, J. and M.O. Robbins, *Shear yielding of amorphous glassy solids: Effect of temperature and strain rate*. Physical Review E, 2003. **68**(1): p. 011507.
132. Ashby, M.F., *A first report on deformation-mechanism maps*. Acta Metallurgica, 1972. **20**(7): p. 887-897.
133. Frost, H.J. and M.F. Ashby, *Deformation-mechanism maps : the plasticity and creep of metals and ceramics*. 1982, Oxford [Oxfordshire]; New York: Pergamon Press.
134. Zhu, T. and J. Li, *Ultra-strength materials*. Progress in Materials Science, 2010. **55**(7): p. 710-757.
135. Yamakov, V., D. Wolf, S.R. Phillpot, A.K. Mukherjee, and H. Gleiter, *Deformation-mechanism map for nanocrystalline metals by molecular-dynamics simulation*. Nature Materials, 2004. **3**(1): p. 43-47.
136. Onimus, F. and J.-L. Béchade, *A polycrystalline modeling of the mechanical behavior of neutron irradiated zirconium alloys*. Journal of Nuclear Materials, 2009. **384**(2): p. 163-174.
137. Dunlop, J.W., Y.J.M. Bréchet, L. Legras, and Y. Estrin, *Dislocation density-based modelling of plastic deformation of Zircaloy-4*. Materials Science and Engineering: A, 2007. **443**(1-2): p. 77-86.
138. Crabtree, G.W. and J.L. Sarrao, *Opportunities for mesoscale science*. Mrs Bulletin, 2012. **37**(11): p. 1079-1088.
139. Matsukawa, Y. and S.J. Zinkle, *Dynamic observation of the collapse process of a stacking fault tetrahedron by moving dislocations*. Journal of Nuclear Materials, 2004. **329-333**, Part B(0): p. 919-923.

140. Wirth, B.D., V.V. Bulatov, and T. De La Diaz Rubia, *Dislocation-stacking fault tetrahedron interactions in Cu*. Journal of Engineering Materials and Technology, Transactions of the ASME, 2002. **124**(3): p. 329-334.
141. Osetsky, Y.N., Y. Matsukawa, R.E. Stoller, and S.J. Zinkle, *On the features of dislocation-obstacle interaction in thin films: large-scale atomistic simulation*. Philosophical Magazine Letters, 2006. **86**(8): p. 511-519.
142. Hashimoto, N., S.J. Zinkle, A.F. Rowcliffe, J.P. Robertson, and S. Jitsukawa, *Deformation mechanisms in 316 stainless steel irradiated at 60°C and 330°C*. Journal of Nuclear Materials, 2000. **283–287**, **Part 1**(0): p. 528-534.
143. Onchi, T., H. Kayano, and Y. Higashiguchi, *The inhomogeneous deformation behaviour of neutron irradiated Zircaloy-2*. Journal of Nuclear Materials, 1980. **88**(2–3): p. 226-235.
144. Wooding, S.J., L.M. Howe, F. Gao, A.F. Calder, and D.J. Bacon, *A molecular dynamics study of high-energy displacement cascades in  $\alpha$ -zirconium*. Journal of Nuclear Materials, 1998. **254**(2–3): p. 191-204.
145. Edwards, D.J., B.N. Singh, and J.B. Bilde-Sørensen, *Initiation and propagation of cleared channels in neutron-irradiated pure copper and a precipitation hardened CuCrZr alloy*. Journal of Nuclear Materials, 2005. **342**(1–3): p. 164-178.
146. Fukumoto, K.-i., M. Sugiyama, and H. Matsui, *Features of dislocation channeling in neutron-irradiated V-(Fe, Cr)-Ti alloy*. Journal of Nuclear Materials, 2007. **367–370**, **Part A**(0): p. 829-833.
147. Shastry, V. and T.D. de la Rubia, *The Interaction Between Point Defects and Edge Dislocation in BCC Iron*. Journal of Engineering Materials and Technology, 1999. **121**(2): p. 126-128.



148. Kipelova, A., R. Kaibyshev, V. Skorobogatykh, and I. Schenkova, *Portevin-Le Chatelier effect in an E911 creep resistant steel with 3%Co additives*. Journal of Physics: Conference Series, 2010. **240**(1): p. 012100.
149. Lebyodkin, M.A., Y. Brechet, Y. Estrin, and L.P. Kubin, *Statistics of the Catastrophic Slip Events in the Portevin-Le Chatelier Effect*. Physical Review Letters, 1995. **74**(23): p. 4758-4761.
150. Bertram, A., T. Böhlke, C. Brüggemann, Y. Estrin, and M. Lebyodkin, *Modeling and Simulation of the Portevin-Le Chatelier Effect*. PAMM, 2006. **6**(1): p. 353-354.
151. Brechet, Y. and Y. Estrin, *On the Influence of Precipitation on the Portevin-Le Chatelier Effect*. Acta Metallurgica Et Materialia, 1995. **43**(3): p. 955-963.
152. Zhang, S., P.G. McCormick, and Y. Estrin, *The morphology of Portevin-Le Chatelier bands: finite element simulation for Al-Mg-Si*. Acta Materialia, 2001. **49**(6): p. 1087-1094.
153. Ackland, G.J., D.J. Bacon, A.F. Calder, and T. Harry, *Computer simulation of point defect properties in dilute Fe-Cu alloy using a many-body interatomic potential*. Philosophical Magazine A, 1997. **75**(3): p. 713-732.
154. Lebensohn, R.A., C.N. Tomé, and P.P. Castañeda, *Self-consistent modelling of the mechanical behaviour of viscoplastic polycrystals incorporating intragranular field fluctuations*. Philosophical Magazine, 2007. **87**(28): p. 4287-4322.
155. Le Saux, M., J. Besson, S. Carassou, C. Poussard, and X. Averty, *A model to describe the anisotropic viscoplastic mechanical behavior of fresh and irradiated Zircaloy-4 fuel claddings under RLA loading conditions*. Journal of Nuclear Materials, 2008. **378**(1): p. 60-69.

156. Berthier, L. and J.-L. Barrat, *Shearing a Glassy Material: Numerical Tests of Nonequilibrium Mode-Coupling Approaches and Experimental Proposals*. Physical Review Letters, 2002. **89**(9): p. 095702.
157. Liu, A.J. and S.R. Nagel, *Nonlinear dynamics: Jamming is not just cool any more*. Nature, 1998. **396**(6706): p. 21-22.
158. Chen, L.B., B.J. Ackerson, and C.F. Zukoski, *Rheological consequences of microstructural transitions in colloidal crystals*. Journal of Rheology, 1994. **38**(2): p. 193-216.
159. Varnik, F., L. Bocquet, J.L. Barrat, and L. Berthier, *Shear Localization in a Model Glass*. Physical Review Letters, 2003. **90**(9): p. 095702.
160. Eyring, H., *Viscosity, Plasticity, and Diffusion as Examples of Absolute Reaction Rates*. The Journal of Chemical Physics, 1936. **4**(4): p. 283-291.
161. Lemaître, A., *Rearrangements and Dilatancy for Sheared Dense Materials*. Physical Review Letters, 2002. **89**(19): p. 195503.
162. Sollich, P., F. Lequeux, P. Hébraud, and M.E. Cates, *Rheology of Soft Glassy Materials*. Physical Review Letters, 1997. **78**(10): p. 2020-2023.
163. Chattoraj, J., C. Caroli, and A. Lemaître, *Universal Additive Effect of Temperature on the Rheology of Amorphous Solids*. Physical Review Letters, 2010. **105**(26): p. 266001.
164. Schuh, C.A. and A.C. Lund, *Atomistic basis for the plastic yield criterion of metallic glass*. Nature Materials, 2003. **2**(7): p. 449-452.
165. Ye, J.C., J. Lu, C.T. Liu, Q. Wang, and Y. Yang, *Atomistic free-volume zones and inelastic deformation of metallic glasses*. Nature Materials, 2010. **9**(8): p. 619-623.

166. Rodney, D., *Activation enthalpy for kink-pair nucleation on dislocations: Comparison between static and dynamic atomic-scale simulations*. Physical Review B, 2007. **76**(14): p. 144108.
167. Karmakar, S., E. Lerner, I. Procaccia, and J. Zylberg, *Statistical physics of elastoplastic steady states in amorphous solids: Finite temperatures and strain rates*. Physical Review E, 2010. **82**(3): p. 031301.
168. Karmakar, S., E. Lerner, and I. Procaccia, *Statistical physics of the yielding transition in amorphous solids*. Physical Review E, 2010. **82**(5): p. 055103.
169. Maloney, C.E. and D.J. Lacks, *Energy barrier scalings in driven systems*. Physical Review E, 2006. **73**(6): p. 061106.
170. Iwashita, T. and T. Egami, *Atomic mechanism of flow in simple liquids under shear*. Physical Review Letters, 2012. **108**(19): p. 196001.